

**(QC THEME) TYPE-TWO QUANTUM COMPUTING IN PBG-BASED
CAVITIES FOR EFFICIENT SIMULATION OF LATTICE GAS DYNAMICS**

Contract # FA9550-04-1-0189

PI: Selim Shahriar, EECS Department, Northwestern University

FINAL REPORT

ABSTRACT

The key challenge in this project was to realize a high-quality PBG structure in a crystalline thin film of diamond. This task proved to be extremely difficult, due to severe constraints. Significant technical hurdles in the context of lithography have to be overcome before a PBG based QC can be realized in NVD. The most promising approach would be to use the polished single crystal and would require research into developing techniques for polishing diamond, and incorporating such a film into E-beam lithography, as outlined at the end of this report. We have also pursued several other lines of work, resulting in demonstrations of complimentary technologies for realizing a QC. These include (a) arbitrary pattern lithography, using atomic interferometry, (b) a QC architecture using atomic ensembles as quantum bits, (c) ultra-low power non-linear optic effects in a tapered nanofiber, as an enabling technology for optically linking ensemble-based quantum bits, and (d) suppression of driver phase correlated fluctuations in the rotation of a quantum bit. Support from this grant led to two Ph.D. theses, and a total of 21 publications, including 5 journal papers.

REPORT DOCUMENTATION PAGE

*Form Approved
OMB No. 0704-0188*

The public reporting burden for this collection of information is estimated to average 1 hour per response, including the time for reviewing instructions, searching existing data sources, gathering and maintaining the data needed, and completing and reviewing the collection of information. Send comments regarding this burden estimate or any other aspect of this collection of information, including suggestions for reducing the burden, to the Department of Defense, Executive Services and Communications Directorate (0704-0188). Respondents should be aware that notwithstanding any other provision of law, no person shall be subject to any penalty for failing to comply with a collection of information if it does not display a currently valid OMB control number.

PLEASE DO NOT RETURN YOUR FORM TO THE ABOVE ORGANIZATION.

1. REPORT DATE (DD-MM-YYYY)		2. REPORT TYPE		3. DATES COVERED (From - To)	
4. TITLE AND SUBTITLE			5a. CONTRACT NUMBER		
			5b. GRANT NUMBER		
			5c. PROGRAM ELEMENT NUMBER		
6. AUTHOR(S)			5d. PROJECT NUMBER		
			5e. TASK NUMBER		
			5f. WORK UNIT NUMBER		
7. PERFORMING ORGANIZATION NAME(S) AND ADDRESS(ES)			8. PERFORMING ORGANIZATION REPORT NUMBER		
9. SPONSORING/MONITORING AGENCY NAME(S) AND ADDRESS(ES)			10. SPONSOR/MONITOR'S ACRONYM(S)		
			11. SPONSOR/MONITOR'S REPORT NUMBER(S)		
12. DISTRIBUTION/AVAILABILITY STATEMENT					
13. SUPPLEMENTARY NOTES					
14. ABSTRACT					
15. SUBJECT TERMS					
16. SECURITY CLASSIFICATION OF:			17. LIMITATION OF ABSTRACT	18. NUMBER OF PAGES	19a. NAME OF RESPONSIBLE PERSON
a. REPORT	b. ABSTRACT	c. THIS PAGE			19b. TELEPHONE NUMBER (Include area code)

INSTRUCTIONS FOR COMPLETING SF 298

1. REPORT DATE. Full publication date, including day, month, if available. Must cite at least the year and be Year 2000 compliant, e.g. 30-06-1998; xx-06-1998; xx-xx-1998.

2. REPORT TYPE. State the type of report, such as final, technical, interim, memorandum, master's thesis, progress, quarterly, research, special, group study, etc.

3. DATES COVERED. Indicate the time during which the work was performed and the report was written, e.g., Jun 1997 - Jun 1998; 1-10 Jun 1996; May - Nov 1998; Nov 1998.

4. TITLE. Enter title and subtitle with volume number and part number, if applicable. On classified documents, enter the title classification in parentheses.

5a. CONTRACT NUMBER. Enter all contract numbers as they appear in the report, e.g. F33615-86-C-5169.

5b. GRANT NUMBER. Enter all grant numbers as they appear in the report, e.g. AFOSR-82-1234.

5c. PROGRAM ELEMENT NUMBER. Enter all program element numbers as they appear in the report, e.g. 61101A.

5d. PROJECT NUMBER. Enter all project numbers as they appear in the report, e.g. 1F665702D1257; ILIR.

5e. TASK NUMBER. Enter all task numbers as they appear in the report, e.g. 05; RF0330201; T4112.

5f. WORK UNIT NUMBER. Enter all work unit numbers as they appear in the report, e.g. 001; AFAPL30480105.

6. AUTHOR(S). Enter name(s) of person(s) responsible for writing the report, performing the research, or credited with the content of the report. The form of entry is the last name, first name, middle initial, and additional qualifiers separated by commas, e.g. Smith, Richard, J, Jr.

7. PERFORMING ORGANIZATION NAME(S) AND ADDRESS(ES). Self-explanatory.

8. PERFORMING ORGANIZATION REPORT NUMBER. Enter all unique alphanumeric report numbers assigned by the performing organization, e.g. BRL-1234; AFWL-TR-85-4017-Vol-21-PT-2.

9. SPONSORING/MONITORING AGENCY NAME(S) AND ADDRESS(ES). Enter the name and address of the organization(s) financially responsible for and monitoring the work.

10. SPONSOR/MONITOR'S ACRONYM(S). Enter, if available, e.g. BRL, ARDEC, NADC.

11. SPONSOR/MONITOR'S REPORT NUMBER(S). Enter report number as assigned by the sponsoring/monitoring agency, if available, e.g. BRL-TR-829; -215.

12. DISTRIBUTION/AVAILABILITY STATEMENT. Use agency-mandated availability statements to indicate the public availability or distribution limitations of the report. If additional limitations/ restrictions or special markings are indicated, follow agency authorization procedures, e.g. RD/FRD, PROPIN, ITAR, etc. Include copyright information.

13. SUPPLEMENTARY NOTES. Enter information not included elsewhere such as: prepared in cooperation with; translation of; report supersedes; old edition number, etc.

14. ABSTRACT. A brief (approximately 200 words) factual summary of the most significant information.

15. SUBJECT TERMS. Key words or phrases identifying major concepts in the report.

16. SECURITY CLASSIFICATION. Enter security classification in accordance with security classification regulations, e.g. U, C, S, etc. If this form contains classified information, stamp classification level on the top and bottom of this page.

17. LIMITATION OF ABSTRACT. This block must be completed to assign a distribution limitation to the abstract. Enter UU (Unclassified Unlimited) or SAR (Same as Report). An entry in this block is necessary if the abstract is to be limited.

A. Report Summary

The primary objective of this project was to investigate the feasibility of realizing a large-scale, Type-II quantum computer using NV-Diamond (NVD). The resulting device was then to be used to demonstrate Type-II quantum computing. The key goal is to use such a quantum computer for efficient simulation of turbulent flows, via the quantum lattice gas dynamics model. In the proposed approach, the qubits are spins of color centers in NVD, located in a single, diffraction limited spot, distinguished from one another via spectral signatures. The inter-qubit coupling is mediated via a combination of external lasers and single-photons in photonic-band-gap (PBG) based cavities. The cavities are etched directly on to the diamond substrate. The set of coupled qubits in each spot represents an individual quantum computer (QC), with a large number of QC's located on a single substrate.

The key technical challenge in this project was to realize a high-quality PBG structure in a crystalline thin film of diamond. This task proved to be extremely difficult, due to severe technical constraints, given in part to the limited time and resources allocated to this project. Our initial approach was to perform lithography on a single crystal diamond. However, the orientation of the crystal made it essentially inert against the range of etching chemicals we tried. In principle, it would be possible to make use of a single crystal diamond with a different orientation that would be etchable. However, another constraint of the type of PBG structure needed for this project is that the substrate must be very thin, ideally close to 2 microns, backed by a silicon substrate. Single crystal diamonds this thin are not available. A possible alternative is to polish a thicker crystal down to this thickness. We were unable to find any vendor that would be able to perform this polishing. Harris offered to make a film with a thickness down to 18 microns, without guaranteeing good surface quality, and stated that they do not know how to make it any thinner. We then moved to using the so-called UNCD (Ultrananocrystalline Diamond) film, invented and developed by Krauss et al. at Argonne National Laboratory. Our E-beam lithographic process, after some modification in the steps, was successful in etching the requisite patterns. However, the holes produced turned out to be of non-uniform depths. This was attributable primarily to the roughness of the surface of the UNCD film.

We then collaborated with Steven Praver of Melbourne University in Australia to pursue an alternative approach: using FIB (focused ion beam) etching of a single crystal. This approach was useful in producing a PBG pattern. However, the FIB process produced microscopic damages that severely degraded the quality of the pattern, making this process unsuitable for a high-Q PBG cavity of the type needed for our project. Annealing after the FIB etching process improved the quality of the PBG pattern somewhat, but not enough.

In parallel to our effort for producing a PBG structure in diamond, we pursued several other lines of work, in order to develop complimentary as well as alternative technologies for realizing a quantum computer. These include (a) development of a new technology of arbitrary pattern lithography, using Bose-condensate based atomic interferometry, (b) development of a quantum computing architecture using atomic ensembles as quantum bits, (c) demonstration of ultra-low power non-linear optic effects via coupling between the evanescent field of a tapered nanofiber and surrounding atoms,

as an enabling technology for optically linking ensemble-based quantum bits, and (d) demonstration of measurement of absolute phase of a localized field via the Bloch-Siegert oscillation, as a technique for suppressing driver phase correlated fluctuations in the rotation of a strongly driven quantum bit.

It is our conclusion that significant technical hurdles in the context of lithography have to be overcome before a PBG based QC can be realized in NVD. The most promising approach would be to use the polished single crystal and conventional lithography. This would require research into developing techniques for polishing diamond while maintaining surface smoothness, and incorporating this film into the E-beam lithography process. In figure 11 of section B.1, we offer an explicit plan for how such a scheme could be carried out in the future. We also believe that, the alternative technology of atomic ensembles as quantum bits, linked with tapered nanofibers, as developed under this grant, is a more promising approach for realizing a quantum computer.

Full or partial support from this grant led to two Ph.D. theses, and a total of 21 publications, including 5 journal papers.

B. TECHNICAL DETAILS

B.1. Lithographic Effort for Producing a PBG Structure in a Diamond Film

The concept of quantum computing using NV-diamond and a PBG structure is recalled briefly in figure 1. The left-most diagram shows the global view of the whole substrate, containing an array of PBG cavities, indicated by red circles. Each red-circled-cavity,

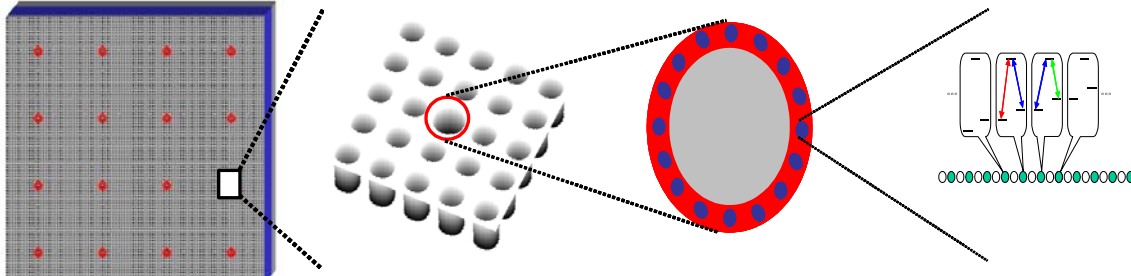


Figure 1: Schematic illustration of the concept of quantum computing using NV-diamond and a PBG structure. See text for details.

along with the active molecules (i.e., diamond color centers) it houses, represent a mini quantum computer (QC). Thus, the diagram shows 16 mini QC's on the same substrate. Of course, a larger substrate (say 12 cm diameter) could host a much larger number of mini QC's. The next diagram shows a zoomed-in view of a single mini-QC, with the red circle (top view of a donut) showing the volume occupied by the cavity mode. The third diagram shows schematically the active molecules inside the cavity mode.

The fourth diagram shows all of these molecules, but arranged according to their spectral response. Because of local non-uniformities, otherwise identical molecules have a range of resonance frequencies for any given transition --- the so-called inhomogeneous broadening. Our model couples a molecule at one spectral point to its spectral neighbor; the coupling is mediated by the cavity photon, and controlled by two external laser frequencies. Each mini-computer can have a large number of distinct quantum bits; however, our goal was to work with a more modest number (about 10 to start with, eventually reaching a 100, in each mini-QC). Thus, the whole chip would consist of say about 10000 mini-QC's, each of which will hold about 100 qubits. Inside each mini-QC, the coupling is quantum mechanical. Among different mini-QC's, the communication/coupling would be strictly classical. This is, of course, the so-called Type II Quantum Computer.

The first step in our project was to design the PBG cavity structure, using FDTD simulation. Figure 2 illustrates the typical process we followed in performing the simulation.

Typically, NV-Diamond is realized by electron bombardment and annealing in a nitrogen atmosphere. Several different types of diamond in principle can be used in this process. These include:

- *Type IA Diamond:* This contains nitrogen as an impurity in fairly substantial amounts (of the order of 0.1%), and which appears to have segregated into small aggregates. Also contains platelets, associated with the nitrogen impurity, the exact structure of which is not known. It has an absorption edge at $\sim 300\text{nm}$ and a broad absorption band between 7 and $10\mu\text{m}$. Most natural diamonds are of this type.
- *Type IB diamond:* This also contains nitrogen as an impurity but in dispersed substitutional form. Almost all synthetic diamonds are of this type.
- *Type IIA Diamond:* This is effectively free of nitrogen impurity. Very rare in nature, these diamonds have enhanced optical and thermal properties. The high purity results in an ultraviolet transmission band down to approximate $230\mu\text{m}$ and absence of infrared absorption in the $7\text{-}10\mu\text{m}$ band.
- *Type IIB Diamond:* A very pure type of diamond which has semiconducting properties: generally blue in color. Extremely rare in nature.
- *CVD Grown Diamond:* These are diamond films grown on a substrate via chemical vapor deposition. These films can be made very thick, and are used for a wide range of industrial applications.
- *UNCD(Ultra Nano-Crystalline Diamond):* UNCD is the name for thin-film diamond material grown through a patented plasma-enhanced chemical vapor deposition process. UNCD is not a diamond-like carbon material, but crystalline diamond consisting of nano-sized grains.

We obtained several different types of diamond for our project. These include:

- *CVD Diamond Wafer:* $3\mu\text{m}$ thick diamond on a $3''$ dia x $0.060''$ thick Si substrate. Vendor: Delaware Diamond Knives (DDK), Inc.
- *Bulk Diamond Crystal:* 2 mm diameter X 0.25 mm thick [110 cut] diamond disk cut from bulk diamond crystal. Vendor: Drukker International
- *Crystalline Optical Grade Diamond:* 0.15mm thick x 5.0 mm diameter disc. Vendor: Harris Int.
- *Polycrystalline Optical Grade Diamond:* 0.25mm thick x 5.0 mm diameter disc. Vendor: Harris Int.
- *UNCD Diamond Films:* UNCD film on Si wafer of several different thicknesses (from $0.5\ \mu\text{m}$ to $5\ \mu\text{m}$) and diameters. Supplier: the group of Dr. J. Carlisle's at Argonne National Lab.

Our initial approach was to perform lithography on a single crystal diamond (the bulk diamond crystal from Drukker International). However, the orientation of the crystal made it essentially inert against the range of etching chemicals we tried. In principle, it would be possible to make use of a single crystal diamond with a different orientation that would be etchable. However, another constraint of the type of PBG structure needed for this project is that the substrate must be very thin, ideally close to 2 microns, backed by a silicon substrate. Single crystal diamonds this thin are not available. A possible alternative is to polish a thicker crystal down to this thickness. We were unable to find any vendor that would be able to perform this polishing. Harris offered to make a film

with a thickness down to 18 microns, without guaranteeing good surface quality, and stated that they do not know how to make it any thinner.

Given this impasse, we proceeded to explore the other types of diamond that were available as films deposited on a substrate. First, we tried the CVD films obtained from

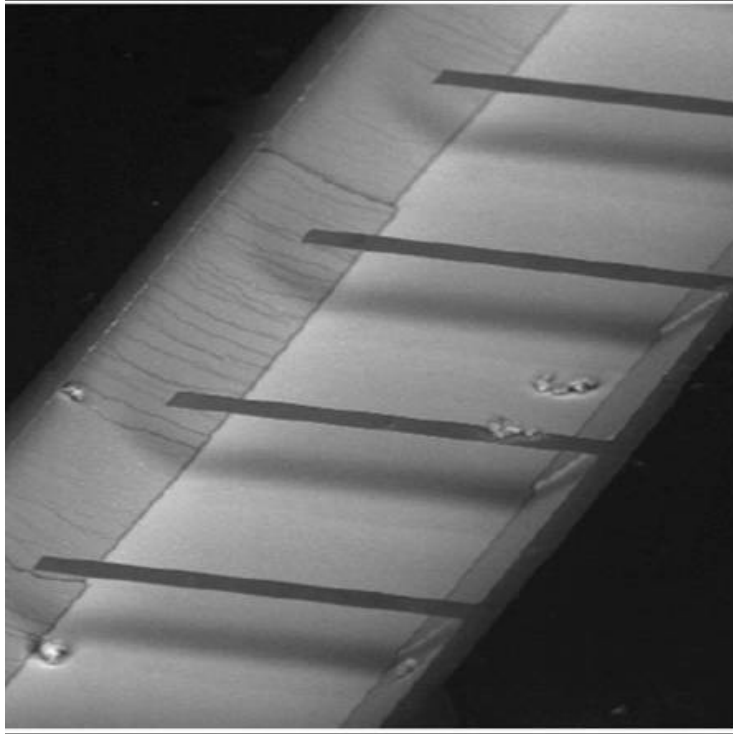


Figure 2: A cantilever structure produced in a UNCD film.

DDK Inc. However, the surface of this crystal was very rough, and clearly unsuited for lithography. At this point, we were made aware of the use of UNCD diamond crystals that were used by our colleagues in the Mechanical Engineering department for creating cantilevers, as shown in figure 2. As such, we decided to pursue the use of this material for creating PBG structure.

Figure 3 summarizes the first result we obtained with UNCD. Figure 3a shows the photolithographic steps used for transferring a computer generated mask to the diamond substrate covered by Silicon Nitride. Figure 3b shows the actual wafer, which consists of a silicon dioxide base under the diamond, and a Silicon Nitride film above it, produced by CVD. This choice was made after several different trials with other types of layers. Figure 3c shows the details of the patterns etched in diamond. Of course, the feature size here is rather large, due to the fact that we used photolithography for the pattern transfer.

The next step was to repeat this process, but with much smaller feature size, employing E-Beam techniques instead of photolithography. Before doing this, we embarked first on designing an actual band-gap structure, tailored specifically to the index of this diamond film. Figure 4 summarizes our two-dimensional modeling of PBG

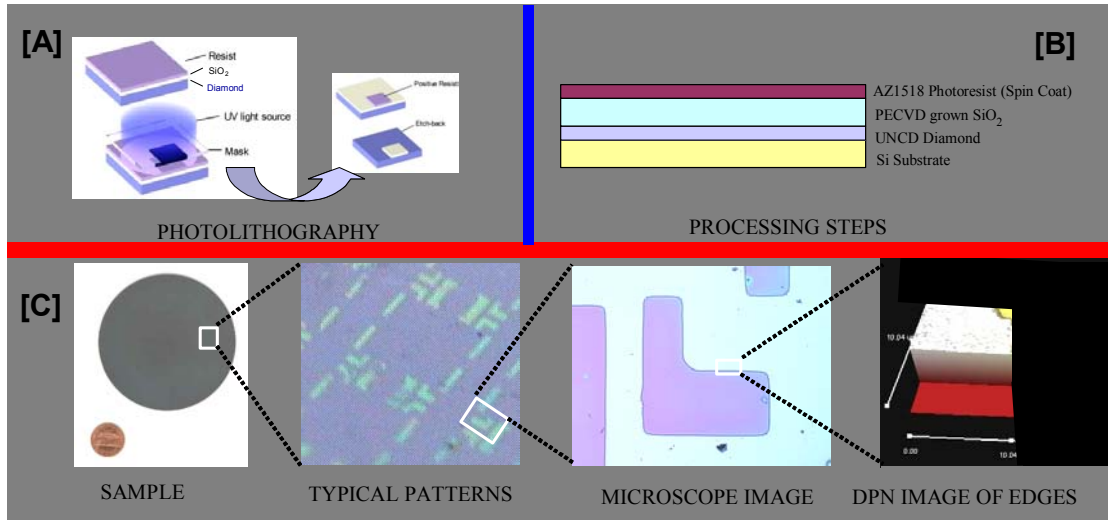


Figure 3: Illustration of the lithographic processes performed for producing pattern in diamond. [A] photolithography used to transfer mask pattern. [B] the layers used for performing the lithography sequentially. [C] observation of patterns produced in diamond film.

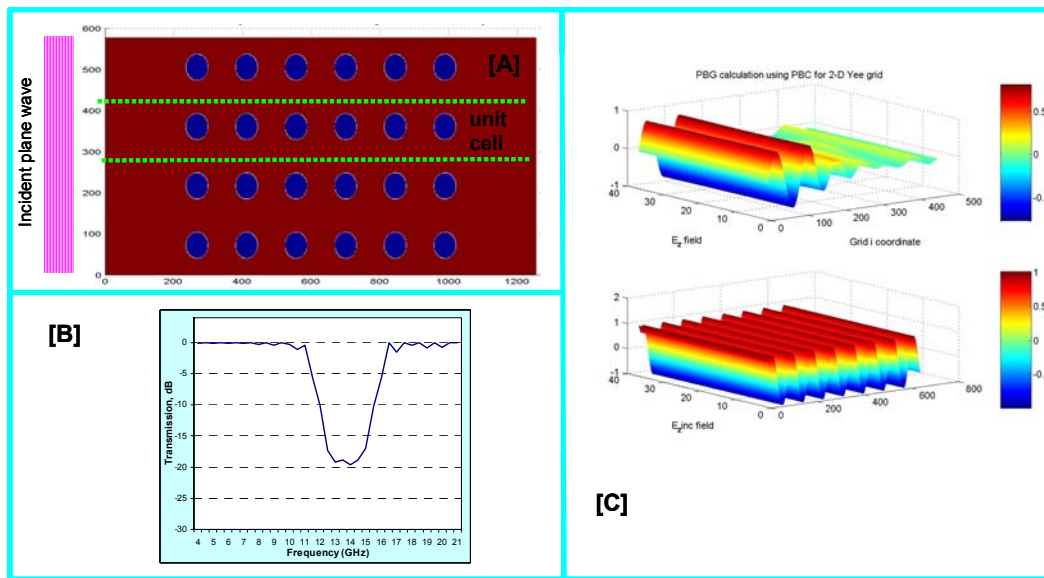


Figure 4: FDTD simulation for photonic bandgap structure, performed for GHz-scale signals. This is then used, through scaling laws, to develop the corresponding structure for diamond [A] Two-dimensional structure with plane wave input [B] The calculated bandgap. [C] typical profiles of input fields and field propagating into the structure.

structure. It is well known that a PBG structure can be designed first at any wavelength, and for any index variation, and then scaling rules can be used to transfer the design to any other wavelength range and indices. As such, we chose to perform the simulation in the GHz range. This makes it possible to compare easily the predictions of our model to existing calculation, without concerning ourselves with the scaling issue up front. The result shown in figure 4c is in close agreement with known calculations of this type.

Figure 5 shows the parameters for the corresponding PBG structure in NVD. The larger hole added in the center leads to a cavity structure. We have also calculated the mode pattern of several cavity designs, as summarized in figure 6.

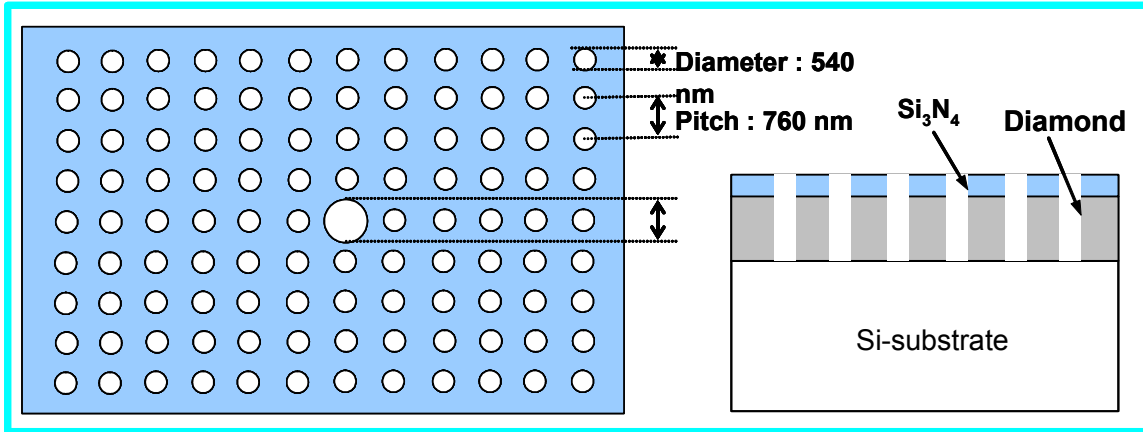


Figure 5: Design of a photonic bandgap structure for diamond, by scaling the parameters from figure 6. The larger whole inserted in the middle leads to a cavity. We have also calculated (not shown) the cavity field mode pattern.

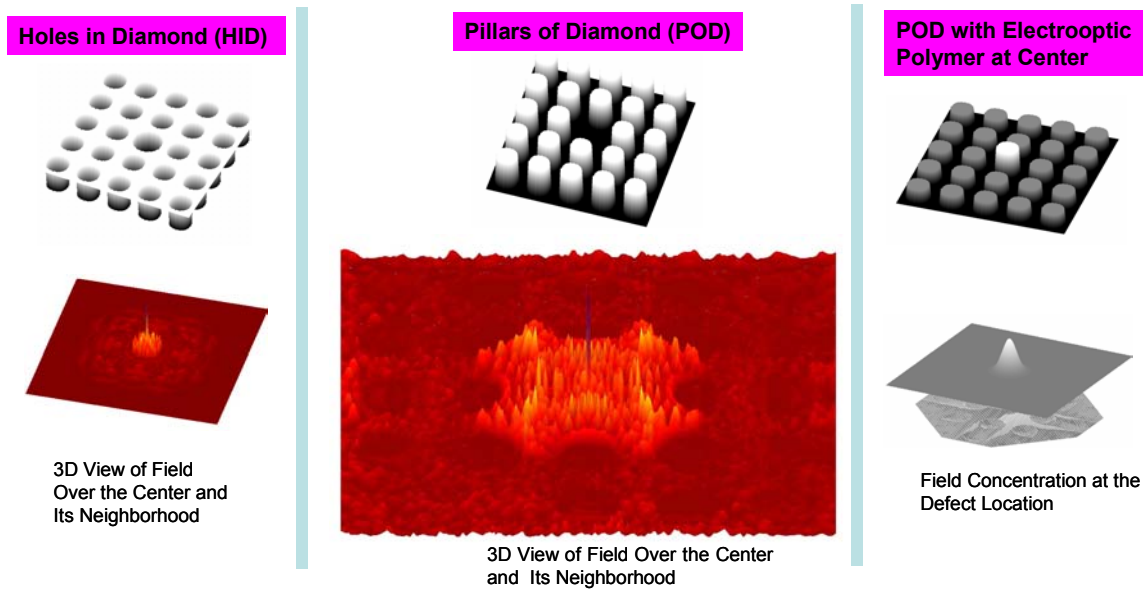


Figure 6: The field concentrations produced in several alternate designs of PBG cavities in diamond.

Figure 7 illustrates schematically the E-beam lithographic process we used to produce very small patterns in an UNCD film. The substrate produced here is similar to the one shown in figure 3b., except that the photoresist is replaced by a layer of PMMA, and the SiO_2 layer is replaced by Al, in order to allow the proper etch stop.

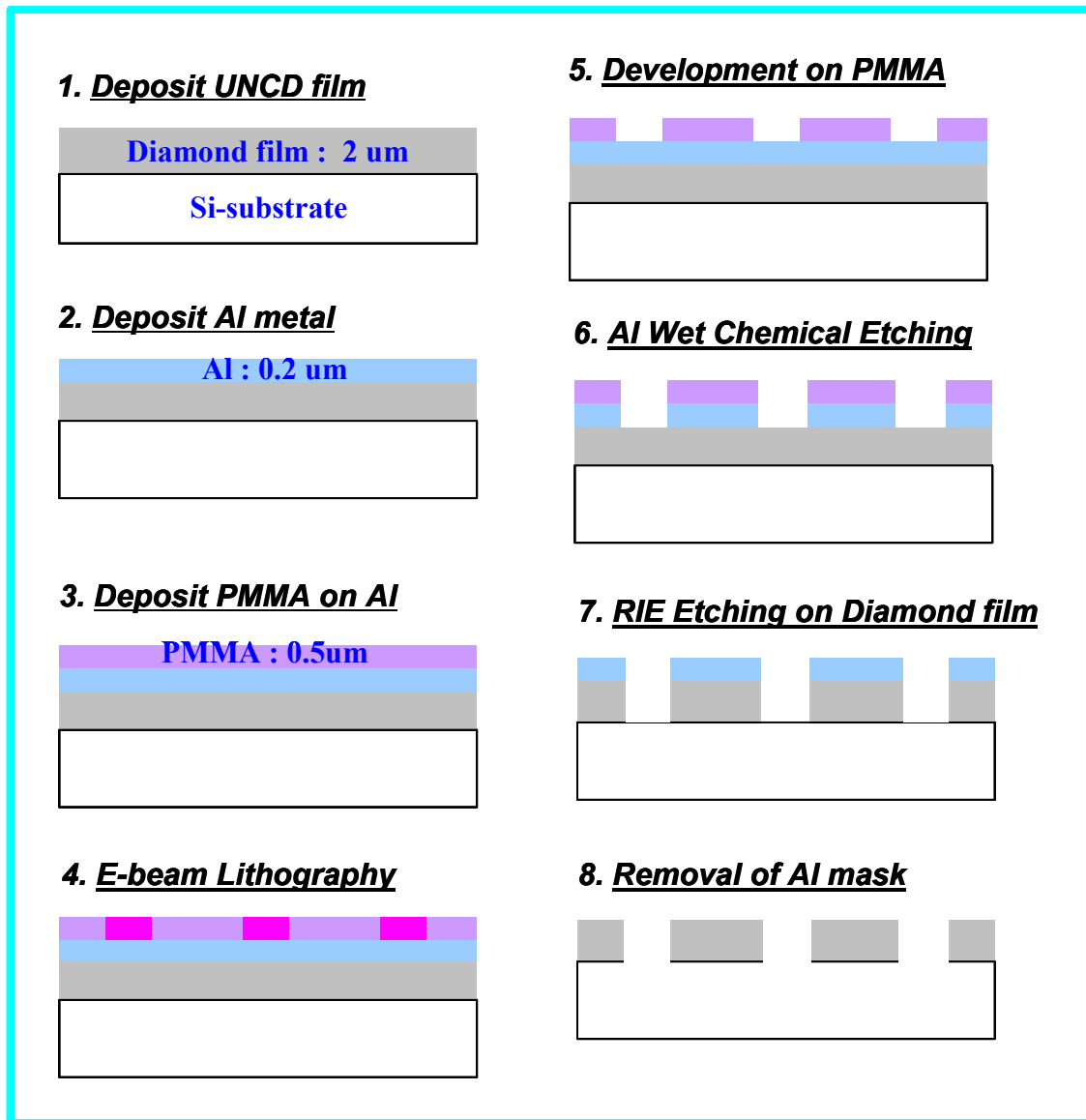


Figure 7: Schematic illustration of the E-beam lithographic process we used to produce very small patterns in an UNCD film. The substrate produced here is similar to the one shown in figure 3b., except that the photoresist is replaced by a layer of PMMA, and the SiO₂ layer is replaced by Al, in order to allow the proper etch stop.

Figure 8 shows a typical pattern produced on a PMMA substrate. Briefly, we placed a thin film of PMMA, using spin coating, on top of the type of wafer shown in figure 7, step 2. We then used an E-beam (with a resolution of 20 nm) to transfer the desired pattern to the PMMA. Here, we have shown an AFM picture of the PMMA layer.

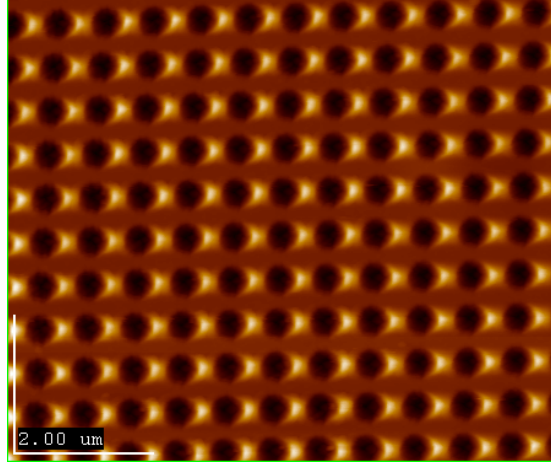


Figure 8: 20 nm resolution E-beam lithography was used to produce this pattern (AFM picture) in a PMMA film produced on top of a Silicon Nitride film, which in turn is above a diamond film. The next step is to use this PMMA pattern to etch the nitride film, and then etch the diamond film.

Figure 9 shows in greater details the AFM data obtained from this structure. As can be seen, the patterns are not very smooth at the bottom. This is attributable primarily to the surface quality of the underlying UNCD film. When we attempted to transfer this pattern to the Aluminum and then to the diamond, this non-uniformity produced very uneven patterns, making it obvious that it would be very difficult using this approach to produce the high-quality PBG cavity in the UNCD film.

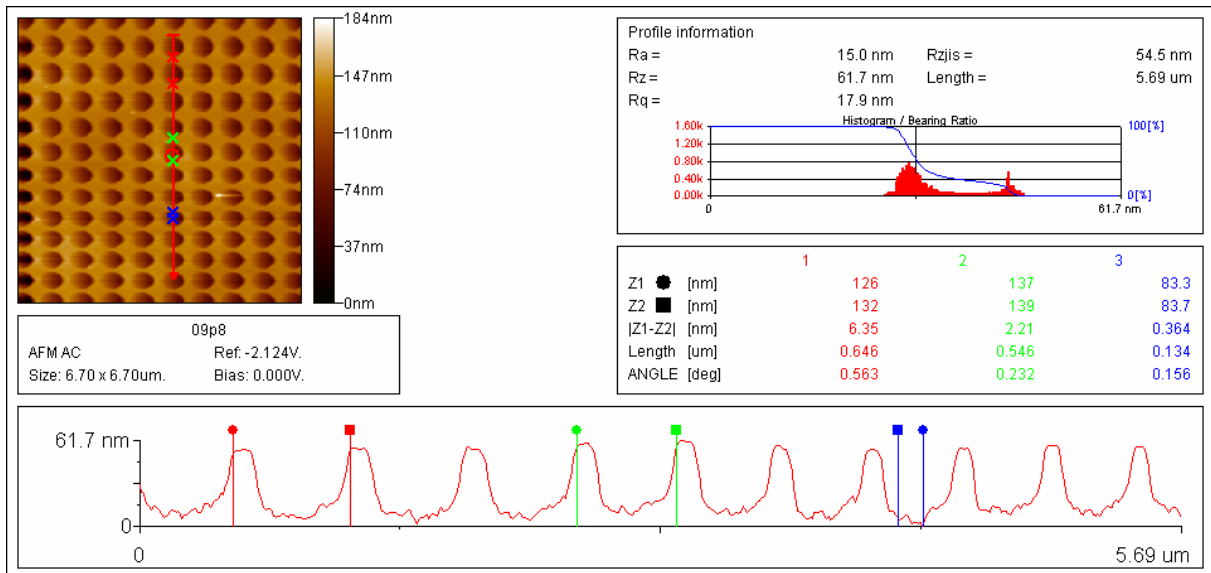


Figure 9: More details of the AFM data obtained from this structure. As can be seen, the patterns are not very smooth at the bottom. This is attributable primarily to the surface quality of the underlying UNCD film.

At this point, we decided that we must go back to the idea of etching single crystal diamond. However, as described above, we were unable to find any vendor willing or able to polish a crystal down to few microns while maintaining the optical quality surface. As such, we decided to collaborate with the group of Steven Prawer at

University of Melbourne in Australia. His group was pursuing the use of focused ion beam (FIB) etching to produce micro-structure in a single crystal diamond. Figure 10 shows some typical structures produced by his group using the FIB process.

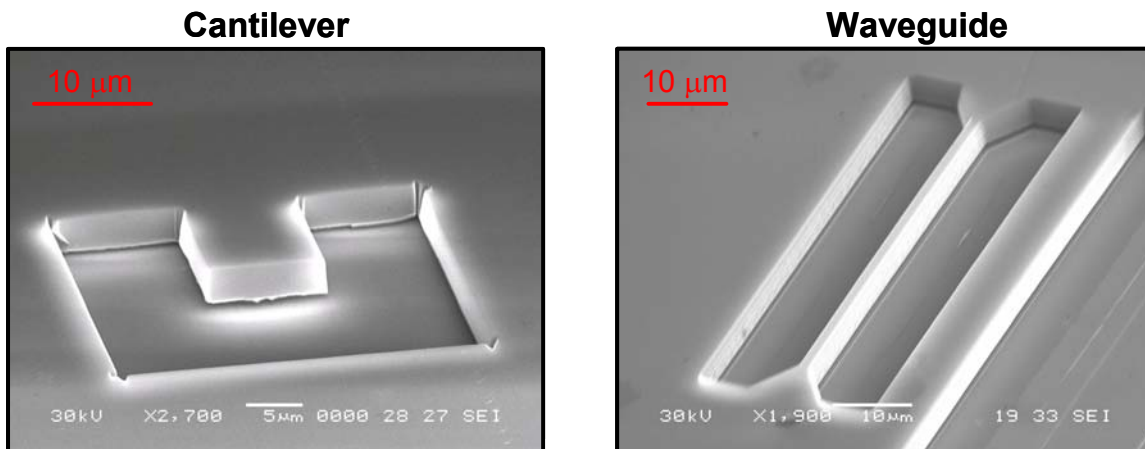


Figure 10. Cantilever and waveguide structures produced by FIB etching of a single crystal diamond by the group of Steven Prawer at Melbourne University.

They also produced a PBG pattern; however, the FIB process produced microscopic damages that severely degraded the quality of the pattern, making this process unsuitable for a high-Q PBG cavity of the type needed for our project. Annealing after the FIB etching process improved the quality of the PBG pattern somewhat, but not enough. It is plausible that further refinement of the FIB process as well as annealing may suppress the damages to a level that would be adequate for a high quality PBG cavity.

Given our findings, we envision only one possible route for realizing high-Q PBG cavities suitable for NV-Diamond quantum computing. This idea is summarized in figure 11. Briefly, we will start with a polished, 18 micron thick single crystal diamond film on a silicon substrate, to be obtained from Harris International, with an etchable crystal orientation. We will then follow the process of E-beam lithography summarized above to produce arrays of PBG cavity structures on the top surface of this film (steps 1 through 3). The process will then be repeated on the other side, thus ending up with a thin (2 microns) layer of diamond with the PBG cavities (steps 4 through 6), backed by a silicon substrate on the top. Finally, electron bombardment would be used to produce the color centers in order to convert the diamond into NVD.

This approach is promising. However, the quality of the structure that can be realized this way can only be determined through experimental studies. We had exhausted the funds and the time allotted under this project by the time we reached this conclusion. As such, this task can only be carried out with additional support from AFOSR or other funding agencies.

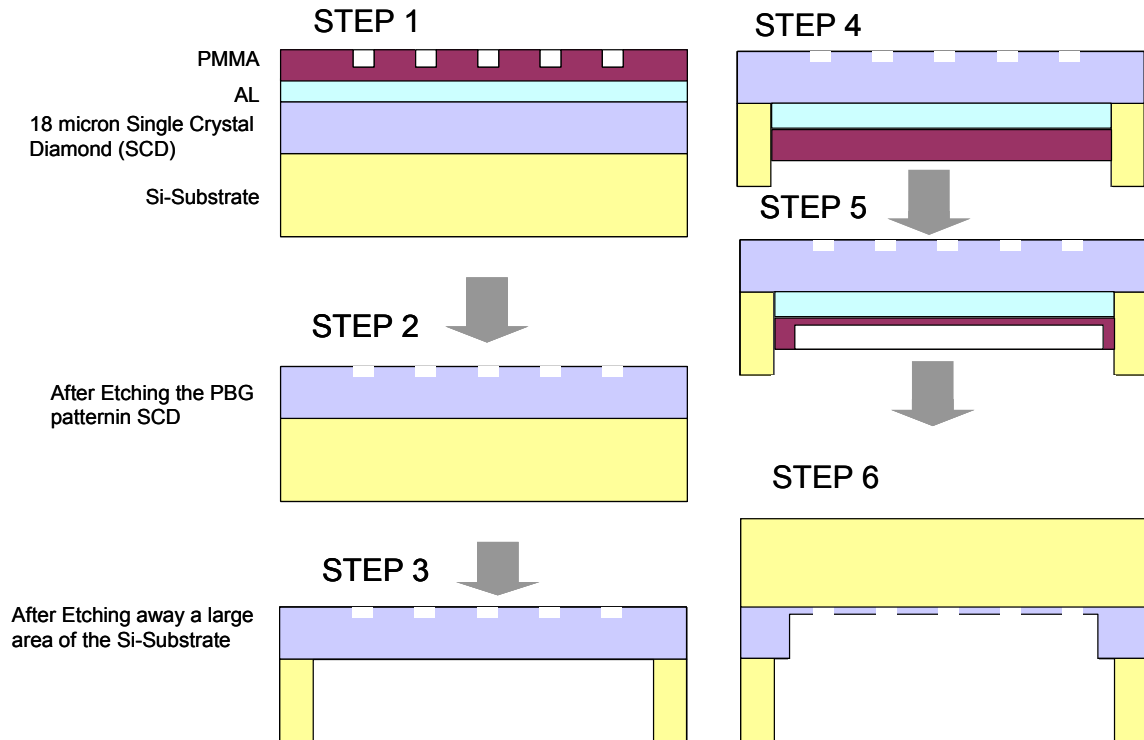


Figure 11: Schematic illustration for creating PBG cavities with E-beam lithography and a single crystal diamond film. Briefly, we will start with a polished, 18 micron thick single crystal diamond film on a silicon substrate, to be obtained from Harris International, with an etchable crystal orientation. We will then follow the process of E-beam lithography summarized above to produce arrays of PBG cavity structures on the top surface of this film (steps 1 through 3). The process will then be repeated on the other side, thus ending up with a thin (2 microns) layer of diamond with the PBG cavities (steps 4 through 6), backed by a silicon substrate on the top.

B.2. Arbitrary Pattern Lithography Using Bose-Condensate Based Atomic Interferometry

Summary:

As a possible alternative to the E-beam lithography, we have developed a scheme for the lithography of arbitrary, two-dimensional nanostructures via matter-wave interference. The required quantum control is provided by a $\pi/2$ - π - $\pi/2$ atom interferometer with an integrated atom lens system. The lens system is developed such that it allows simultaneous control over the atomic wave-packet spatial extent, trajectory, and phase signature. We demonstrate arbitrary pattern formations with two-dimensional ^{87}Rb wave packets through numerical simulations of the scheme in a practical parameter space. Prospects for experimental realizations of the lithography scheme are also discussed. This technique may be able to produce patterns as small as 2 nm, and could be of widespread utility for many applications. The high resolution of this technique could also make it possible to make the PBG patterns with higher precision, which would ultimately be required for precision quantum computing

Reproduction of published journal paper: (15 pages)

This work was published in Physical Review A, and is reproduced below.

Two-dimensional nanolithography using atom interferometry

A. Gangat, P. Pradhan, G. Pati, and M. S. Shahriar

Department of Electrical and Computer Engineering, Northwestern University, Evanston, Illinois 60208, USA

(Received 4 May 2004; published 12 April 2005)

We propose a scheme for the lithography of arbitrary, two-dimensional nanostructures via matter-wave interference. The required quantum control is provided by a $\pi/2$ - π - $\pi/2$ atom interferometer with an integrated atom lens system. The lens system is developed such that it allows simultaneous control over the atomic wave-packet spatial extent, trajectory, and phase signature. We demonstrate arbitrary pattern formations with two-dimensional ^{87}Rb wave packets through numerical simulations of the scheme in a practical parameter space. Prospects for experimental realizations of the lithography scheme are also discussed.

DOI: 10.1103/PhysRevA.71.043606

PACS number(s): 03.75.Dg, 39.20.+q, 04.80.-y, 32.80.Pj

I. INTRODUCTION

The last few decades have seen a great deal of increased activity toward the development of a broad array of lithographic techniques [1,2]. This is because of their fundamental relevance across all technological platforms. These techniques can be divided into two categories: parallel techniques using light and serial techniques using matter. The optical lithography techniques have the advantage of being fast because they can expose the entire pattern in parallel. However, these techniques are beginning to reach the limits imposed upon them by the laws of optics, namely, the diffraction limit [3]. The current state of the art in optical lithography that is used in industry can achieve feature sizes on the order of hundreds of nanometers. Efforts are being made to push these limits back by using shorter-wavelength light such as x rays [2], but this presents problems of its own. The serial lithography techniques, such as electron beam lithography [1], can readily attain a resolution on the order of tens of nanometers. However, because of their serial nature these methods are very slow and do not provide a feasible platform for the industrial mass fabrication of nanodevices.

A different avenue for lithography presents itself out of recent developments in the fields of atomic physics and atom optics, namely, the experimental realization of a Bose-Einstein condensate (BEC) [4,5] and the demonstration of the atom interferometer [6–12]. In essence, these developments provide us with the tools needed in order to harness the wave nature of matter. This is advantageous for lithography because the comparatively smaller de Broglie wavelength of atoms readily allows for a lithographic resolution on the nanometer scale. The atom interferometer provides a means of interfering matter waves in order to achieve lithography on such a scale. The BEC, on the other hand, provides a highly coherent and populous source with which to perform this lithography in a parallel fashion. The opportunity thus presents itself to combine the enhanced resolution of matter interferometry with the high throughput of traditional optical lithography.

It should be noted that, although there has been research activity on atom lithography [13–15] for a number of years, most of the work has involved using standing waves of light as optical masks for the controlled deposition of atoms on a substrate. The primary limitations of using such optical

masks are that the lithographic pattern cannot be arbitrary and that the resolution of the pattern is limited to the 100 nm scale. Since our scheme uses the atom interferometer, however, it allows for pattern formation by self-interference of a matter wave, and is thus unhampered by the inherent limitations of the optical mask technique.

In this paper we seek to demonstrate theoretically the use of the atom interferometer as a platform for nanolithography by proposing a technique that allows for the manipulation of a single-atom wave packet so as to achieve two-dimensional lithography of an arbitrary pattern on the single-nanometer scale. To do this our scheme employs a lens system along one arm of the interferometer that performs Fourier imaging [3] of the wave-packet component that travels along that arm. By investigating such a technique for a single atom wave packet, we hope to establish the viability of using a similar technique for a single BEC wave packet, which would allow for truly high-throughput lithography.

The paper is organized as follows. Section II presents an overview of the proposed technique. Sections III and IV provide a theoretical analysis of the atom interferometer itself and our proposed imaging system, respectively. Section V is devoted to some practical considerations of the setup and its parameter space, and Sec. VI gives the results of numerical simulations. Finally, we touch upon the issue of replacing the single-atom wave packet with the macroscopic wave function of a BEC in Sec. VII. Appendixes A and B show some of the steps in the derivations.

II. PROPOSED INTERFEROMETER

A. Principles of operation

In a $\pi/2$ - π - $\pi/2$ atom interferometer (AI), which was first theoretically proposed by Borde [6] and experimentally demonstrated by Kasevich and Chu [7], an atom beam is released from a trap and propagates in free space until it encounters a $\pi/2$ pulse, which acts as a 50-50 beam splitter [16–22]. The split components then further propagate in free space until they encounter a π pulse, which acts as a mirror so that the trajectories of the split beam components now intersect. The beams propagate in free space again until they encounter another $\pi/2$ pulse at their point of intersection, which now acts as a beam mixer. Because of this beam mixing, any

phase shift ϕ introduced between the beams before they are mixed will cause an interference to occur such that the observed intensity of one of the mixed beams at a substrate will be proportional to $1 + \cos \phi$, much as in the Mach-Zehnder interferometer [23] from classical optics. For our scheme we propose the same type of interferometer, but with a single atom released from the trap instead of a whole beam.

Now, if we introduce an arbitrary, spatially varying phase shift $\phi(x,y)$ between the two arms of the interferometer before they mix, the intensity of their interference pattern as observed on a substrate will be proportional to $1 + \cos \phi(x,y)$. Thus, in our system, we use an appropriate choice of $\phi(x,y)$ in order to form an arbitrary, two-dimensional pattern. This quantum phase engineering (already demonstrated for BECs [24,25]) is achieved by using the ac-Stark effect so that $I(x,y) \propto \phi(x,y)$, where $I(x,y)$ is the intensity of an incident light pulse.

Also, in order to achieve interference patterns on the nanoscale, $\phi(x,y)$ must itself be at nanometer resolution. However, reliable intensity modulation of a light pulse is limited to the submicrometer range due to diffraction effects. One way to address this is by focusing the wave packet after it is exposed to the submicrometer resolution phase shift $\phi(x,y)$, thereby further scaling down $\phi(x,y)$ to nanometer resolution after it is applied to the wave packet. Our scheme achieves this scaling via an atom lens system.

Additionally, just as with a Gaussian laser beam, exposing a single Gaussian wave packet to a spatially varying phase shift $\phi(x,y)$ will cause it to scatter. In order for both the phase-shifted and non-phase-shifted components of the wave packet to properly interfere, our lens system is also used to perform Fourier imaging [30] such that, at the substrate, the phase-shifted component of the wave packet is an unscattered Gaussian that is properly aligned with its non-phase-shifted counterpart and has the phase information $\phi(x,y)$ still intact. Indeed, the lens system, which is created using the ac-Stark effect, serves the double purpose of scaling down the phase information $\phi(x,y)$ from submicrometer resolution to single-nanometer resolution and neutralizing the wave-packet scattering caused by the same phase shift $\phi(x,y)$.

B. Schematic

In our overall scheme, represented by Fig. 1, the atoms are treated as Λ systems [26–33] (inset B) and are prepared in the ground state $|1\rangle$. A single-atom trap [34–36] is used to release just one atomic wave packet along the z axis. After traveling a short distance, the wave packet is split by a $\pi/2$ pulse into internal states $|1\rangle$ and $|3\rangle$. The state- $|3\rangle$ component gains additional momentum along the y axis and separates from the state- $|1\rangle$ component after they both travel further along the z axis. Next, a π pulse causes the two components to transition their internal states and thereby reflect their trajectories. The component along the top arm is now in the original ground state $|1\rangle$ and proceeds to be exposed to the lens system. The lenses of the lens system are pulses of light that intercept the state- $|1\rangle$ component of the wave packet at different times. By modulating their spatial intensity in the x - y plane, these pulses of light are tailored to impart a par-

ticular phase pattern in the x - y plane to the wave-packet component that they interact with via the ac-Stark effect. As shown in inset B, Fig. 1, the detuning of the light that the lenses are composed of is several times larger for state $|3\rangle$ than for state $|1\rangle$. The lenses can therefore be considered to have a negligible ac-Stark effect on the state- $|3\rangle$ wave-packet component as compared to the state- $|1\rangle$ component. This is important, because in a practical situation the separation between the wave packets for $|1\rangle$ and $|3\rangle$ may be small enough so that the transverse extent of the lens pulses could overlap both wave packets.

The first light pulse is intensity modulated to carry the phase information of the first lens of the lens system. It then intercepts the state- $|1\rangle$ wave-packet component and adds the phase $\phi_1(x,y)$. After some time the state- $|1\rangle$ component has evolved due to the first lens such that it is an appropriate size for exposure to the phase information corresponding to the arbitrary pattern image (inset A). Another light pulse is intensity modulated to carry the phase information of both the second lens and the inverse cosine of the arbitrary pattern. The pulse intercepts the state- $|1\rangle$ component and adds the additional phase $\phi_2(x,y)$. After some time a third light pulse is prepared and applied to the state- $|1\rangle$ component to add a phase of $\phi_3(x,y)$, which act as the third lens of the lens system. Soon after, the final $\pi/2$ pulse mixes the trajectories of the wave-packet components. A chemically treated wafer is set to intercept the state- $|1\rangle$ component in the x - y plane. Due to the mixing caused by the last $\pi/2$ pulse, only a part of what is now the state- $|1\rangle$ component has gone through the lens system. Because of the lens system, it arrives at the wafer with a phase that is a scaled-down version of the image phase $\phi_P(x,y) = \arccos P(x,y)$. The other part of what is now the state- $|1\rangle$ component did not go through the lens system. There is therefore a phase difference of $\phi_P(x,y)$ between the two parts of the state- $|1\rangle$ component and the wave packet strikes the wafer in an interference pattern proportional to $1 + \cos[\arccos P(x,y)] = 1 + P(x,y)$. The impact with the wafer alters the chemically treated surface, and the pattern is developed through chemical etching.

As a note, one preparation for the wafer is to coat it with a self-assembled monolayer [37]. However, Hill *et al.* [38] demonstrate an alternate approach using hydrogen passivation, which may be better suited for lithography at the single-nanometer scale due to its inherent atomic-scale granularity.

Finally, note that the coated wafer may reflect as well as scatter the pulses of the lens system. The phase fronts of the wave packets may potentially be distorted if exposed to these reflections and scatterings. However, this problem can be overcome easily as follows. During the time window over which the lens pulses are applied, a small mirror is placed at an angle in front of the wafer, so as to deflect the lens pulses in a harmless direction. This will also have the added benefit of not exposing the wafer to the lens pulses at all. Right after the last lens pulse has been applied and deflected, the mirror will be moved out of the way, thus allowing the atomic waves to hit the wafer surface.

III. ANALYSIS OF THE INTERFEROMETER ($\pi/2$ - π - $\pi/2$)

A. Formalism

As explained in the previous section, we consider the behavior of a single-atomic wave packet in our formulation of

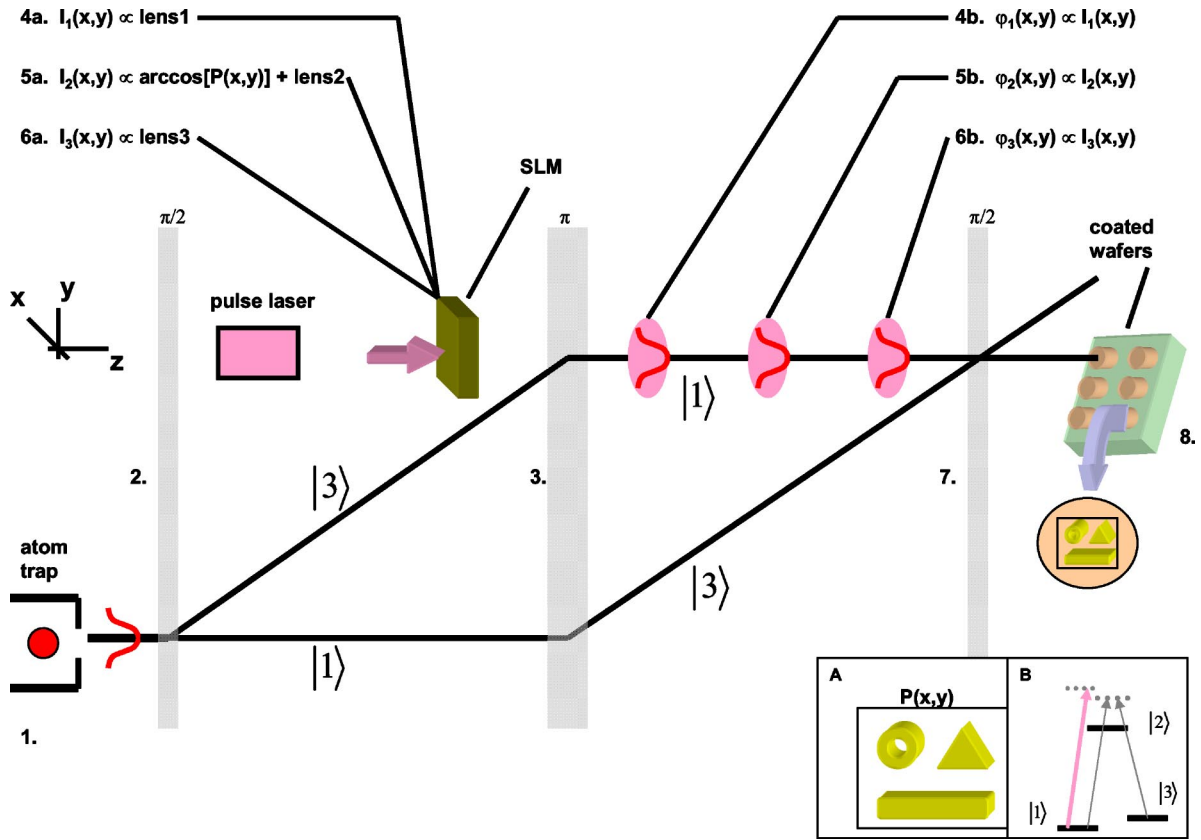


FIG. 1. A single-atomic wave packet is released from the atom trap. (2) The wave packet is split using a $\pi/2$ pulse. (3) The split components are reflected by a π pulse. (4a) The spatial light modulator (SLM) modulates a light pulse such that it will act as the first lens of the atom lens system. (4b) The light pulse intercepts the wave-packet component that is in state $|1\rangle$ and imparts a phase signature $\phi_1(x,y)$ via the ac-Stark effect. (5a) Now the SLM modulates a second light pulse such that it will impart both the phase information corresponding to the arbitrary image $\{\arccos[P(x,y)]\}$ and the phase information of the second lens of the lens system. (5b) The second light pulse intercepts the same wave-packet component as the first one and imparts the phase signature $\phi_2(x,y)$. (6a) The SLM modulates a third light pulse, preparing it to act as the third lens of the lens system. (6b) The third light pulse intercepts the same wave-packet component as the other two pulses and imparts a phase $\phi_3(x,y)$. (7) Both wave-packet components are mixed along the two trajectories by a $\pi/2$ pulse. (8) A chemically treated wafer intercepts the state- $|1\rangle$ component so that an interference pattern forms on the wafer proportional to $1 + \cos\{\arccos[P(x,y)]\} = 1 + P(x,y)$. Inset A: The image $P(x,y)$ that is to be transferred ultimately to the wafer. Inset B: The internal energy states of the wave packet modeled as a Λ system. The light pulses used for the atom lenses have a much larger detuning for ground state $|3\rangle$ than they do for ground state- $|1\rangle$ so that they effectively only interact with the state- $|1\rangle$ component of the wave packet. The $\pi/2$ pulses and the π pulse use light that is largely detuned for both ground states.

the problem. Also, in order to understand and simulate the AI [6–12] properly, the atom must be modeled both internally and externally. It is the internal evolution of the atom while in a laser field that allows for the splitting and redirecting of the beam to occur in the AI. However, the internal evolution is also dependent on the external state. Also, while the external state of the atom accounts for most of the interference effects which result in the arbitrary pattern formation, the internal state is responsible for some nuances here as well.

In following the coordinate system as shown in Fig. 1, we write the initial external wave function as

$$|\Psi_e(\vec{r}, t=0)\rangle = \frac{1}{\sigma\sqrt{\pi}} \exp\left(\frac{-|\vec{r}|^2}{2\sigma^2}\right) \quad (1)$$

where $\vec{r} = x\hat{i} + y\hat{j}$.

Internally, the atom is modeled as a three-level Λ system [26–33] (as shown in Fig. 1, inset B) and is assumed to be initially in state $|1\rangle$:

$$|\Psi_i(t)\rangle = c_1(t)|1\rangle + c_2(t)|2\rangle + c_3(t)|3\rangle, \quad (2)$$

where we consider $c_1(0)=1$, $c_2(0)=0$, $c_3(0)=0$. States $|1\rangle$ and $|3\rangle$ are metastable states, while state $|2\rangle$ is an excited state.

As will become evident later, in some cases it is more expedient to express the atom's wave function in k space [39]. To express our wave function, then, in terms of momentum, we first use Fourier theory to reexpress the external wave function as

$$|\Psi_e(x, y, t)\rangle = \frac{1}{2\pi} \int \int |\Phi_e(p_x, p_y, t)\rangle |p_x\rangle |p_y\rangle dp_x dp_y, \quad (3)$$

where we let $|p_x\rangle = e^{i(p_x/\hbar)x}$ and $|p_y\rangle = e^{i(p_y/\hbar)y}$. The complete wave function is simply the outer product of the internal and external states [Eqs. (2) and (3)]:

$$|\Psi(x, y, t)\rangle = \frac{1}{2\pi} \int \int [C_1(p_x, p_y, t)|1, p_x, p_y\rangle + C_2(p_x, p_y, t) \times |2, p_x, p_y\rangle + C_3(p_x, p_y, t)|3, p_x, p_y\rangle] dp_x dp_y, \quad (4)$$

where $C_n(p_x, p_y, t) = c_n(t)|\Phi_e(p_x, p_y, t)\rangle$. In position space, the outer product gives

$$|\Psi(\vec{r}, t)\rangle = c_1(t)|1, \Psi_e(\vec{r}, t)\rangle + c_2(t)|2, \Psi_e(\vec{r}, t)\rangle + c_3(t)|3, \Psi_e(\vec{r}, t)\rangle. \quad (5)$$

B. State evolution in free space

The free-space evolution of a wave function is fully derived in Appendix A. Presented here are simply the results cast in our particular formalism. For the free-space Hamiltonian $H = \int \int \sum_{n=1}^3 [(p_x^2 + p_y^2)/2m + \hbar\omega_n]|n, p_x, p_y\rangle \times \langle n, p_x, p_y| dp_x dp_y$, if the wave function is known at time $t=0$, then after a duration of time T in free space, the wave function becomes

$$\begin{aligned} |\Psi(\vec{r}, t=T)\rangle &= \frac{1}{2\pi} \int \int [C_1(p_x, p_y, 0)e^{-i[(p_x^2+p_y^2)/2m\hbar+\omega_1]T}|1, p_x, p_y\rangle \\ &+ C_2(p_x, p_y, 0)e^{-i[(p_x^2+p_y^2)/2m\hbar+\omega_2]T}|2, p_x, p_y\rangle \\ &+ C_3(p_x, p_y, 0)e^{-i[(p_x^2+p_y^2)/2m\hbar+\omega_3]T}|3, p_x, p_y\rangle] dp_x dp_y, \end{aligned} \quad (6a)$$

or

$$\begin{aligned} |\Psi(\vec{r}, t=T)\rangle &= e^{-i\omega_1 T} c_1(0)|1, \Psi_e(\vec{r}, T)\rangle + e^{-i\omega_2 T} c_2(0) \\ &\times |2, \Psi_e(\vec{r}, T)\rangle + e^{-i\omega_3 T} c_3(0)|3, \Psi_e(\vec{r}, T)\rangle. \end{aligned} \quad (6b)$$

C. State evolution in π and $\pi/2$ pulse laser fields

The electromagnetic fields encountered by the atom at points 2, 3, and 7 in Fig. 1 that act as the $\pi/2$, π , and $\pi/2$ pulses are each formed by two lasers that are counterpropagating in the y - z plane parallel to the y axis. We use the electric dipole approximation to write the Hamiltonian in these fields as

$$\begin{aligned} H &= \int \int \sum_{n=1}^3 \left(\frac{p_x^2 + p_y^2}{2m} + \hbar\omega_n \right) |n, p_x, p_y\rangle \langle n, p_x, p_y| dp_x dp_y \\ &- e_0 \vec{\epsilon} \cdot \frac{\vec{E}_{A0}}{2} [e^{i(\omega_A t - k_A \hat{y} + \phi_A)} + e^{-i(\omega_A t - k_A \hat{y} + \phi_A)}] \\ &- e_0 \vec{\epsilon} \cdot \frac{\vec{E}_{B0}}{2} [e^{i(\omega_B t + k_B \hat{y} + \phi_B)} + e^{-i(\omega_B t + k_B \hat{y} + \phi_B)}], \end{aligned} \quad (7)$$

where \vec{E}_{A0} and \vec{E}_{B0} are vectors denoting the magnitude and polarization of the fields traveling in the $+$ and $-y$ directions, respectively, $\vec{\epsilon}$ is the position vector of the electron, and e_0 is the electron charge. Refer to Appendix B for the complete derivation of the wave function evolution in these fields. Only the results are presented here.

If the atom begins completely in state $|1, \Psi_e(\vec{r}, t)\rangle$ then after a time T of evolving in the above described fields, the result is

$$\begin{aligned} |\Psi(\vec{r}, t=T)\rangle &= \cos\left(\frac{\Omega}{2}T\right)|1, \Psi_e(\vec{r}, 0)\rangle \\ &- i e^{i(\omega_B - \omega_A)T + i(\phi_B - \phi_A)} \sin\left(\frac{\Omega}{2}T\right)|3, \Psi_e(\vec{r}, 0)\rangle e^{-i(k_A + k_B)y}, \end{aligned} \quad (8)$$

where we have used the definitions given in Sec. III A. We see that for a π pulse ($T = \pi/\Omega$), Eq. (8) becomes

$$\begin{aligned} |\Psi(x, y, t = \pi/\Omega)\rangle &= -i e^{i(\omega_B - \omega_A)\pi/\Omega + i(\phi_B - \phi_A)} \\ &\times |3, \Psi_e(x, y, 0)\rangle e^{-i(k_A + k_B)y}, \end{aligned} \quad (9)$$

while for a $\pi/2$ pulse [$T = \pi/(2\Omega)$], Eq. (8) yields

$$\begin{aligned} |\Psi(x, y, t = \pi/(2\Omega))\rangle &= \frac{1}{\sqrt{2}}|1, \Psi_e(x, y, 0)\rangle - i e^{i(\omega_B - \omega_A)\pi/2\Omega + i(\phi_B - \phi_A)} \\ &\times \frac{1}{\sqrt{2}}|3, \Psi_e(x, y, 0)\rangle e^{-i(k_A + k_B)y}. \end{aligned} \quad (10)$$

Similarly, if the atom begins completely in state $|3, \Psi_e(\vec{r}, t)\rangle$, the wave function after a time T becomes

$$\begin{aligned} |\Psi(x, y, t=T)\rangle &= -i e^{i(\omega_A - \omega_B)T + i(\phi_A - \phi_B)} \sin\left(\frac{\Omega}{2}T\right) \\ &\times |1, \Psi_e(x, y, 0)\rangle e^{i(k_A + k_B)y} + \cos\left(\frac{\Omega}{2}T\right) \\ &\times |3, \Psi_e(x, y, 0)\rangle, \end{aligned} \quad (11)$$

so that for a π pulse, Eq. (11) gives

$$\begin{aligned} |\Psi(x, y, t = \pi/\Omega)\rangle &= -i e^{i(\omega_A - \omega_B)\pi/\Omega + i(\phi_A - \phi_B)} \\ &\times |1, \Psi_e(x, y, 0)\rangle e^{i(k_A + k_B)y}, \end{aligned} \quad (12)$$

and for a $\pi/2$ pulse, Eq. (11) becomes

$$\begin{aligned} |\Psi(x, y, t = \pi/(2\Omega))\rangle &= -i e^{i(\omega_A - \omega_B)\pi/2\Omega + i(\phi_A - \phi_B)} \frac{1}{\sqrt{2}} \\ &\times |1, \Psi_e(x, y, 0)\rangle e^{i(k_A + k_B)y} \\ &+ \frac{1}{\sqrt{2}}|3, \Psi_e(x, y, 0)\rangle. \end{aligned} \quad (13)$$

D. State evolution through the whole interferometer

To see the effects of phase explicitly, we make use of the analysis that we have done for the state evolution of the

wave packet. Take our initial wave packet $|\Psi\rangle$ to have initial conditions as discussed in Sec. III A. At time $t=0$ the first $\pi/2$ pulse equally splits $|\Psi\rangle$ into two components $|\Psi_a\rangle$ and $|\Psi_b\rangle$ such that

$$|\Psi_a\rangle = -ie^{i(\omega_B - \omega_A)\pi/2\Omega + i(\phi_{B1} - \phi_{A1})} \frac{1}{\sqrt{2}} |3, \Psi_e(x, y, 0)\rangle e^{-i(k_A + k_B)y}, \quad (14a)$$

$$|\Psi_b\rangle = \frac{1}{\sqrt{2}} |1, \Psi_e(x, y, 0)\rangle, \quad (14b)$$

where we used Eq. (8). After a time $t=T_0$ of free space [Eq. (6b)] and then a π pulse, Eqs. (8) and (11) yield

$$|\Psi_a\rangle = -e^{i(\omega_A - \omega_B)\pi/2\Omega + i(\phi_{A2} - \phi_{A1} + \phi_{B1} - \phi_{B2}) - i\omega_3 T_0} \frac{1}{\sqrt{2}} \times |1, \Psi_e(x, y - y_0, T_0)\rangle, \quad (15a)$$

$$|\Psi_b\rangle = -ie^{i(\omega_B - \omega_A)\pi/\Omega + i(\phi_{B2} - \phi_{A2}) - i\omega_1 T_0} \frac{1}{\sqrt{2}} |3, \Psi_e(x, y, T_0)\rangle \times e^{-i(k_A + k_B)y}. \quad (15b)$$

The $|\Psi_a\rangle$ component becomes shifted in space by y_0 due to the momentum it gained in the $+y$ direction from the π pulse. Now another zone of free space for a time T_0 [Eq. (7)] followed by the final $\pi/2$ pulse [using Eqs. (8) and (11)] forms

$$|\Psi_a\rangle = -e^{i(\omega_A - \omega_B)\pi/2\Omega + i(\phi_{A2} - \phi_{A1} + \phi_{B1} - \phi_{B2}) - i(\omega_1 + \omega_3)T_0} \times \frac{1}{2} |1, \Psi_e(x, y - y_0, 2T_0)\rangle + ie^{i(\phi_{A2} - \phi_{A1} - \phi_{A3} + \phi_{B1} - \phi_{B2} + \phi_{B3}) - i(\omega_1 + \omega_3)T_0} \times \frac{1}{2} |3, \Psi_e(x, y - y_0, 2T_0)\rangle e^{-i(k_A + k_B)y}, \quad (16a)$$

$$|\Psi_b\rangle = -e^{i(\omega_B - \omega_A)\pi/2\Omega + i(\phi_{B2} - \phi_{B3} - \phi_{A2} + \phi_{A3}) - i(\omega_1 + \omega_3)T_0} \times \frac{1}{2} |1, \Psi_e(x, y - y_0, 2T_0)\rangle - ie^{i(\omega_B - \omega_A)\pi/\Omega + i(\phi_{B2} - \phi_{A2}) - i(\omega_1 + \omega_3)T_0} \times \frac{1}{2} |3, \Psi_e(x, y - y_0, 2T_0)\rangle e^{-i(k_A + k_B)y}. \quad (16b)$$

Now the $|\Psi_b\rangle$ component is spatially aligned with the $|\Psi_a\rangle$ component. However, another split occurs because both of these components are partially in internal state $|3\rangle$. After some further time T_1 in free space, state $|3\rangle$ has drifted further in the $+y$ direction. The substrate can now intercept the two internal states of the total wave function in separate locations. We write the state- $|1\rangle$ and $-|3\rangle$ wave functions as

$$|\Psi_1\rangle = -\frac{1}{2} (e^{i(\omega_B - \omega_A)\pi/2\Omega + i(\phi_{B2} - \phi_{B3} - \phi_{A2} + \phi_{A3})} + e^{i(\omega_A - \omega_B)\pi/2\Omega + i(\phi_{A2} - \phi_{A1} + \phi_{B1} - \phi_{B2})}) \times |1, \Psi_e(x, y - y_0, 2T_0 + T_1)\rangle e^{-i(\omega_1 + \omega_3)T_0}, \quad (17a)$$

$$|\Psi_3\rangle = i\frac{1}{2} (e^{i(\phi_{A2} - \phi_{A1} - \phi_{A3} + \phi_{B1} - \phi_{B2} + \phi_{B3})} - e^{i(\omega_B - \omega_A)\pi/\Omega + i(\phi_{B2} - \phi_{A2})}) \times |3, \Psi_e(x, y - y_0 - y_1, 2T_0 + T_1)\rangle e^{-i(k_A + k_B)y - i(\omega_1 + \omega_3)T_0}. \quad (17b)$$

These have populations

$$\langle \Psi_1 | \Psi_1 \rangle = \frac{1}{2} [1 + \cos(\phi_0)], \quad \langle \Psi_3 | \Psi_3 \rangle = \frac{1}{2} [1 - \cos(\phi_0)], \quad (18)$$

where $\phi_0 = (\pi/\Omega)(\omega_A - \omega_B) - \phi_{A1} + \phi_{B1} + 2\phi_{A2} - 2\phi_{B2} - \phi_{A3} + \phi_{B3}$. We see that the state populations are functions of the phase differences of the laser fields. Since we can choose these phase differences arbitrarily, we can populate the states arbitrarily. If we choose the phases, for example, such that ϕ_0 is some multiple of 2π , then the wave-packet population will end up entirely in internal state $|1\rangle$.

IV. ARBITRARY IMAGE FORMATION

If, however, between the π pulse and the second $\pi/2$ pulse we apply a spatially varying phase shift $\phi_P(\vec{r})$ to $|\Psi_a\rangle$, but keep ϕ_0 as a multiple of 2π , then the populations in Eqs. (20) become instead

$$\langle \Psi_1 | \Psi_1 \rangle = \frac{1}{2} \{1 + \cos[\phi_P(\vec{r})]\}, \quad \langle \Psi_3 | \Psi_3 \rangle = \frac{1}{2} \{1 - \cos[\phi_P(\vec{r})]\}. \quad (19)$$

Therefore, if we let $\phi_P(\vec{r}) = \arccos[P(\vec{r})]$, where $P(\vec{r})$ is an arbitrary pattern normalized to 1, the state $|1\rangle$ population will be

$$\langle \Psi_1 | \Psi_1 \rangle = \frac{1}{2} [1 + P(\vec{r})]. \quad (20)$$

If the substrate at 8 in Fig. 1 intercepts just this state, the population distribution will be in the form of the arbitrary image. Over time, depositions on the substrate will follow the population distribution, and thereby physically form the image on the substrate.

A. Imparting an arbitrary, spatially varying phase shift for arbitrary image formation

We now review how to do such phase imprinting [24,25] to a single wave packet using the ac-Stark effect. First, consider the Schrödinger equation (SE) for the wave packet expressed in position space:

$$i\hbar \frac{\partial |\Psi(\vec{r}, t)\rangle}{\partial t} = \frac{-\hbar^2}{2m} \nabla^2 |\Psi(\vec{r}, t)\rangle + V(\vec{r}) |\Psi(\vec{r}, t)\rangle. \quad (21)$$

If we consider a very short interaction time τ with the potential $V(\vec{r})$, we find

$$i\hbar \frac{\partial |\Psi(\vec{r}, t + \tau)\rangle}{\partial t} \approx V(\vec{r}) |\Psi(\vec{r}, t + \tau)\rangle \quad (22a)$$

$$\Rightarrow |\Psi(\vec{r}, t + \tau)\rangle \approx |\Psi(\vec{r}, t)\rangle e^{-(i/\hbar)V(\vec{r})\tau}. \quad (22b)$$

Thus, we see that an arbitrary phase shift $\phi_P(\vec{r})$ is imparted on the wave packet in position space by choosing $V(\vec{r}) = (\hbar/\tau)\phi_P(\vec{r})$. Although this would give the negative of the desired phase, it makes no difference because it is the cosine of the phase that gives the interference pattern.

In order to create the arbitrary potential needed to impart the arbitrary phase shift, we use the ac-Stark effect (light shift). As illustrated in Fig. 1 at 4b, 5b, and 6b, the atom will be in the internal state $|1\rangle$. If exposed to a detuned laser field that only excites the $|1\rangle \rightarrow |2\rangle$ transition, the eigenstates become perturbed such that their energies shift in proportion to the intensity of the laser field. A spatially varying intensity will yield a spatially varying potential energy. Specifically, in the limit that $g/\delta \rightarrow 0$, where g is proportional to the square root of the laser intensity and δ is the detuning, it is found that the energy of the ground state is approximately $\hbar g^2/(4\delta)$. To impart the pattern phase, then, we subject the atomic wave packet at 4b, 5b, and 6b in Fig. 1 to a laser field that has an intensity variation in the x - y plane such that

$$g^2(\vec{r}) = (4\delta/\tau)\phi_P(\vec{r}) = (4\delta/\tau)\arccos[P(\vec{r})], \quad (23)$$

where $P(\vec{r})$ is the arbitrary pattern normalized to 1 and τ is the interaction time.

B. The need for a lens system

The need for a lens system for the atomic wave packet arises due to two separate considerations. First, there is a need for expanding and focusing the wave packet in order to shrink down the phase pattern imparted at 5b in Fig. 1. We have shown above how the phase pattern is imparted using an intensity variation on an impinging light pulse. However, due to the diffraction limit of light, the scale limit of this variation will be on the order of 100 nm. This will cause the interference at 8 to occur on that scale. To reach a smaller scale, we require a lens system that allows expansion and focusing of the wave packet to occur in the transverse plane. Using such a system, we could, for example, expand the wave packet by two orders of magnitude prior to 5b, impart the phase pattern at 5b, and then focus it back to its original size by the time it reaches 8. The interference would then occur on the scale of 1 nm.

The second consideration that must be made is that an arbitrary phase shift $\phi(x, y)$ introduced at 5b, if it has any variation at all in the transverse plane, will cause the wave packet traveling along that arm of the AI to alter its momentum state. Any free-space evolution after this point will make the wave packet distort or go off trajectory, causing a noisy

interference or even eliminating interference at 8 all together.

Our lens system, then, must accomplish two objectives simultaneously: (1) allow for an expansion and focusing of the wave packet to occur and (2) have the wave packet properly aligned and undistorted when it reaches 8. To do this, we employ techniques similar to those developed in classical Fourier optics [3]. First we develop a diffraction theory for the two-dimensional (2D) quantum-mechanical wave packet; then we use the theory to set up a lens system that performs spatial Fourier transforms on the wave packet in order to achieve the two above stated objectives.

C. Development of the quantum-mechanical wave-function diffraction theory

Consider the 2D SE in freespace

$$i\hbar \frac{\partial |\Psi(\vec{r}, t)\rangle}{\partial t} = \frac{-\hbar^2}{2m} \left(\frac{\partial^2}{\partial x^2} + \frac{\partial^2}{\partial y^2} \right) |\Psi(\vec{r}, t)\rangle. \quad (24)$$

By inspection, we see that it is linear and shift independent. If we can then find the impulse response of this ‘‘system’’ and convolve it with an arbitrary input, we can get an exact analytical expression for the output. To proceed, we first try to find the transfer function of the system.

Using the method of separation of variables, it is readily shown that all solutions of the system (the 2D SE in free space) can be expressed as linear superpositions of the following function:

$$\Psi(\vec{r}, t) = A e^{i[\vec{k}\cdot\vec{r} - (\hbar/2m)|\vec{k}|^2 t]} \quad (25)$$

where A is some constant and $\vec{k} = k_x \hat{i} + k_y \hat{j}$ can take on any values. Now let us take some arbitrary input to our system at time $t=0$ and express it in terms of its Fourier components:

$$|\Psi_{\text{in}}(\vec{r})\rangle = \frac{1}{2\pi} \int |\Phi_{\text{in}}(\vec{k})\rangle e^{i\vec{k}\cdot\vec{r}} d\vec{k}. \quad (26)$$

We can then evolve each Fourier component for a time T by using Eq. (25) to get the output

$$\begin{aligned} |\Psi_{\text{out}}(\vec{r})\rangle &= \frac{1}{2\pi} \int |\Phi_{\text{in}}(\vec{k})\rangle e^{i[\vec{k}\cdot\vec{r} - (\hbar/2m)|\vec{k}|^2 T]} d\vec{k} \\ &= \frac{1}{2\pi} \int (|\Phi_{\text{in}}(\vec{k})\rangle e^{-i(\hbar/2m)|\vec{k}|^2 T}) e^{i\vec{k}\cdot\vec{r}} d\vec{k} \\ &= \frac{1}{2\pi} \int |\Phi_{\text{out}}(\vec{k})\rangle e^{i\vec{k}\cdot\vec{r}} d\vec{k}. \end{aligned} \quad (27)$$

It follows that

$$|\Phi_{\text{out}}(\vec{k})\rangle = |\Phi_{\text{in}}(\vec{k})\rangle e^{-i(\hbar/2m)|\vec{k}|^2 T}. \quad (28)$$

Our transfer function, then, for a free-space system of time duration T is

$$H(\vec{k}) = e^{-i(\hbar/2m)|\vec{k}|^2 T}. \quad (29)$$

After taking the inverse Fourier transform, we find the impulse response to be

$$h(\vec{r}) = -i \left(\frac{m}{\hbar T} \right) e^{i(m/2\hbar T)|\vec{r}|^2}. \quad (30)$$

Finally, convolving this with some input to the system at time $t=0$, $|\Psi_{\text{in}}(\vec{r})\rangle$, gives the output at time $t=T$, $|\Psi_{\text{out}}(\vec{r})\rangle$, to be

$$|\Psi_{\text{out}}(\vec{r})\rangle = -i \left(\frac{1}{2\pi\hbar T} \frac{m}{\hbar T} \right) e^{i(m/2\hbar T)|\vec{r}|^2} \int |\Psi_{\text{in}}(\vec{r}')\rangle \times e^{i(m/2\hbar T)|\vec{r}'|^2} e^{-i(m/\hbar T)\vec{r}\cdot\vec{r}'} d\vec{r}'. \quad (31)$$

This expression is analogous to the *Fresnel diffraction integral* from classical optics.

D. Fourier transform lens scheme

Consider now the following.

(1) Take as input some wave function $|\Psi(\vec{r})\rangle$, and use the light shift to apply a “lens” (in much the same way as we show above how to apply the arbitrary pattern phase) such that it becomes

$$|\Psi(\vec{r})\rangle e^{-i(m/2\hbar T)|\vec{r}|^2}.$$

(2) Pass it through the free-space system for a time T using the above derived integral to get

$$-i \left(\frac{1}{2\pi\hbar T} \frac{m}{\hbar T} \right) e^{i(m/2\hbar T)|\vec{r}|^2} \int |\Psi(\vec{r}')\rangle e^{-i(m/\hbar T)\vec{r}\cdot\vec{r}'} d\vec{r}'$$

(3) Now use the light shift again to create another “lens” where the phase shift is $e^{-i[(m/2\hbar T)|\vec{r}|^2 - \pi/2]}$ so that we are left with

$$\left(\frac{1}{2\pi\hbar T} \frac{m}{\hbar T} \right) \int |\Psi(\vec{r}')\rangle e^{-i(m/\hbar T)\vec{r}\cdot\vec{r}'} d\vec{r}'.$$

We see that this is simply a scaled version of the Fourier transform (FT) of the input. This lens system, then, is such that

$$|\Psi_{\text{out}}(\vec{r})\rangle = \left(\frac{1}{2\pi\hbar T} \frac{m}{\hbar T} \right) \left| \Phi_{\text{in}} \left(\frac{m}{\hbar T} \vec{r} \right) \right\rangle, \quad (32)$$

where $|\Phi_{\text{in}}\rangle$ is the FT of $|\Psi_{\text{in}}\rangle$.

E. Using the FT lens scheme to create a distortion-free expansion and focusing system for applying the pattern phase

In order to achieve our desired goals of doing expansion and focusing and preventing distortion, we propose the system illustrated in Fig. 2(a). We first input our Gaussian wave packet into a FT scheme with a characteristic time parameter $T=T_A$. We will then get the Fourier transform of the input (also a Gaussian) scaled by $m/(\hbar T_A)$. Then, we give the wave packet a phase shift that corresponds to the desired interference pattern (pattern phase) and put it through another FT scheme with the same time parameter T_A . The wave function is now the convolution of the original input with the pattern phase. Finally, a third FT scheme is used with $T=T_B$ so that the output is the same as the wave function just before the second FT scheme, but is now reflected about the origin and scaled by $m/(\hbar T_B)$ instead of $m/(\hbar T_A)$. The pattern phase, therefore, has been scaled down by a factor of

T_A/T_B . Since both T_A and T_B can be chosen arbitrarily, we can, in principle, scale down the pattern phase by orders of magnitude. If, for example, the pattern phase is first imparted on a scale of ~ 100 nm, we can choose T_A/T_B to be 100 so that at the output of our lens system, it is on a scale of ~ 1 nm. By scaling down the pattern phase, we can scale down the interference pattern at point 8 in Fig. 1.

Within the context of the interferometer, our lens system is placed at 4b, 5b, and 7 in Fig. 1. Now, since the system provides us with the desired output immediately in time after the final lens [lens 3b in Fig. 2(a)], this final lens, the final $\pi/2$ pulse, and the substrate 6 all need to be adjacent. If they are not, the wave packet will undergo extra free-space evolution and may distort. However, such a geometry is difficult to achieve experimentally so we propose a modification to the lens system [Fig. 2(b)]. Specifically, we can move the lens 3b in Fig. 2(a) to occur immediately before lens 2a, as long as we rescale it to account for the different wave-packet size at that location. We call the rescaled version 3b', which is the same as 3b except for the parameter T_A in place of T_B . We can then place the substrate at 8 in Fig. 2(a) to be where the lens 3b previously was; that is, a time T_B away from lens 3a. The final $\pi/2$ pulse can occur anywhere between lens 3a and the substrate, as long as it is far enough away from the substrate to allow sufficient time for the state- $|3\rangle$ component to separate from the state- $|1\rangle$ component. To avoid disturbing the requisite symmetry of the AI, we accomplish this by choosing T_B to be sufficiently large while leaving the final $\pi/2$ pulse itself in its original location. This geometry will allow the substrate to intercept the state- $|1\rangle$ component exclusively and at precisely the right moment such that it does not undergo too little or too much free-space evolution without having any of the final $\pi/2$ pulse, final lens, or substrate adjacent. Finally, we can simplify the lens system's implementation if we combine the lenses that are adjacent. Lenses 1b, 2a, 3b', and $\phi_p(\vec{r})$ can be combined into lens α ; lenses 2b and 3a can be combined into lens β . Explicitly, lens α has phase shift

$$\phi_\alpha(\vec{r}) = - \left(\frac{3m}{2\hbar T_A} \right) |\vec{r}|^2 + \pi - \phi_p(\vec{r}) \quad (33)$$

and lens β has phase shift

$$\phi_\beta(\vec{r}) = - \left(\frac{m}{2\hbar T_A} + \frac{m}{2\hbar T_B} \right) |\vec{r}|^2 + \frac{\pi}{2}. \quad (34)$$

Figure 2(c) shows the implementation of the lens system within the context of the whole AI.

A cause for concern may arise in the fact that with the lens system in place, the part of the wave packet that travels along the arm without the lens will be interfering not with a phase-modified version of itself, but with a phase-modified Fourier transform of itself. That is, the output of the lens system is a phase-modified Fourier transform of its input. As such, the effective width of the wave packet coming from the lens system may be significantly larger than the effective width of that coming from the arm without lenses, thus causing a truncation of the pattern formation around the edges. This problem is addressed by selecting T_B such that the wave

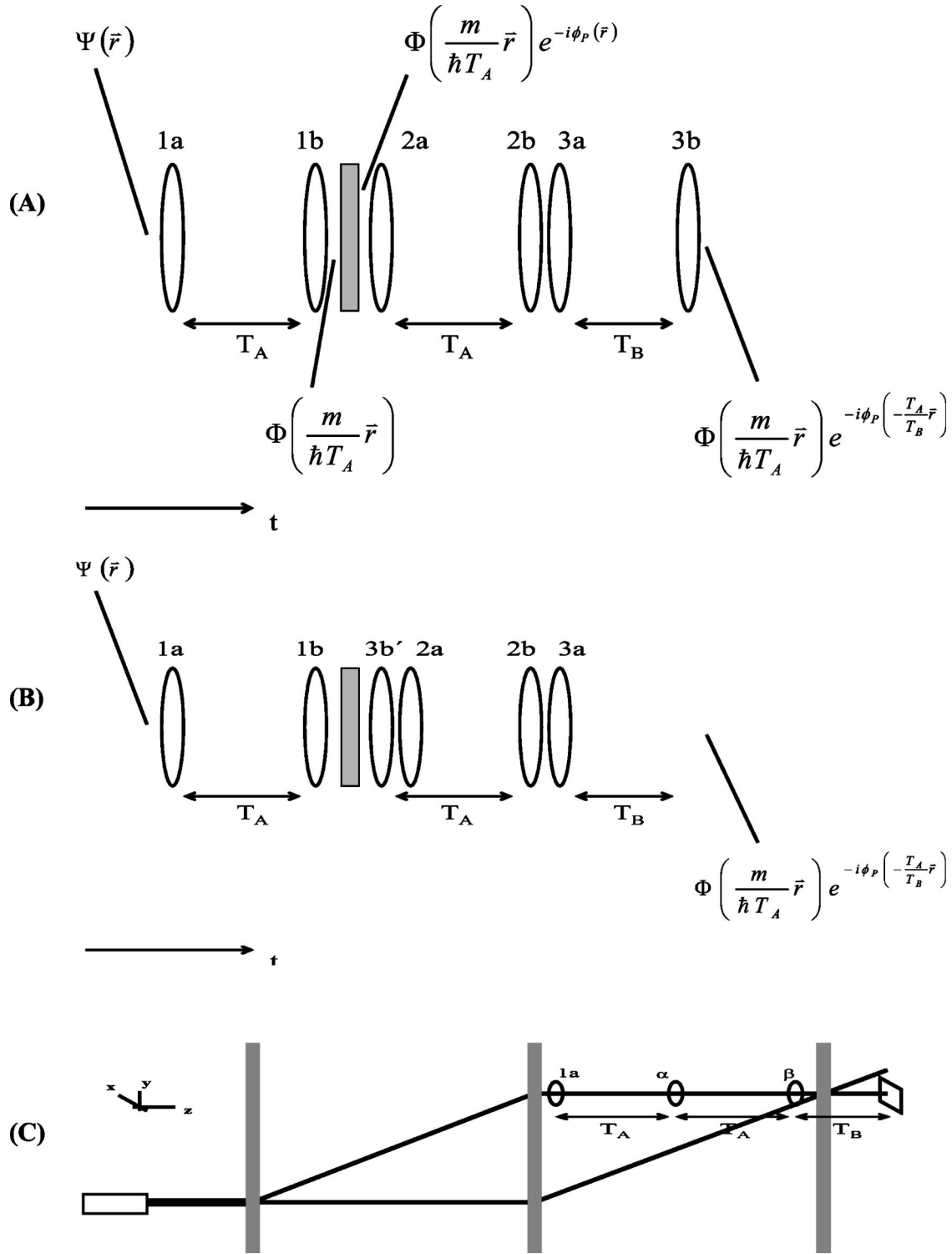


FIG. 2. (A) The lens system. Each lens is actually a pulse of light with a transverse intensity modulation. Between lenses 1a and 1b and 2a and 2b are free-space regions of time duration T_A , while between lenses 3a and 3b there is a free-space region of duration T_B . Lenses 1a and 2a give the wave function a phase $\phi_{1a}=\phi_{2a}=-\frac{m}{2\hbar T_A}|\vec{r}|^2$, lenses 1b and 2b impart a phase $\phi_{1b}=\phi_{2b}=-\frac{m}{2\hbar T_A}|\vec{r}|^2+\pi/2$, lens 3a gives a phase $\phi_{3a}=-\frac{m}{2\hbar T_B}|\vec{r}|^2$, and lens 3b gives a phase $\phi_{3b}=-\frac{m}{2\hbar T_B}|\vec{r}|^2+\pi/2$. (B) The lens system from (A) rearranged. The input and output are still the same, but the output is no longer immediately preceded by a lens. Lens 3b is the same as lens 3b from (A) except for T_A in place of T_B so that it gives a phase shift of $\phi_{3b'}=-\frac{m}{2\hbar T_A}|\vec{r}|^2+\pi/2$. (C) The modified lens system in context. Lenses α and β are composites of the lenses from the system of (B). Between lenses 1a and α is a free-space region of time length T_A , as well as between lenses α and β . Between lens β and the substrate is a free-space region of time duration T_B . Values of $\phi_\alpha(\vec{r})$ and $\phi_\beta(\vec{r})$ are as in Eqs. (33) and (34), respectively.

packet from the lens system is scaled to have an effective width equivalent to or smaller than the wave packet from the other arm. Also, because of the Fourier transform, the wave packet coming from the lens system, even without an added pattern phase, may have a different phase signature from the wave packet coming from the other arm. Regarding this issue, our numerical experiments show that after free-space propagation for a time on the order of the time scale determined as practical (see Sec. V), the phase difference between the original wave packet and its Fourier transform is very small over the span of the effective width of the wave packet. Thus, the effect of this phase noise on the interference pattern is negligible.

V. SOME PRACTICAL CONSIDERATIONS

A. Wave-packet behavior

The behavior of the wave packet primarily has implications for the time and wave-packet effective width parameters of the lithography scheme. As mentioned earlier, the scale limit of the intensity variation that creates the pattern phase when it is first applied is $\sim 10^{-7}$ m. The lens system then further reduces the scale of the pattern phase by a factor of T_A/T_B . To achieve lithography features on the scale of ~ 1 nm, this ratio needs to be ~ 100 . However, we must also take into consideration the extent of the entire intensity variation. In other words, referring to Fig. 2(c), the effective width of the wave packet at lens α must be large enough to accommodate the entire pattern on the light pulse bearing the phase pattern information. We assume that this dimension will be on the order of a millimeter. We know that the wave packet at lens α is a scaled Fourier transform of the wave packet immediately before lens 1a, so that its effective width at lens α is $\hbar T_A/m\sigma_{\text{in}}$. This must be on the order of 10^{-3} m. Also, another way in which the time parameters are restricted is by the total amount of time that the atom spends in the AI.

Now, as shown earlier, it is the state- $|1\rangle$ component in our scheme that will form the desired interference pattern. The substrate must therefore intercept this component exclusive of the state- $|3\rangle$ component. Fortunately, the state- $|3\rangle$ component will have an additional velocity in the y direction due to photon recoil so that the two states will separate if given enough time. Also recall that each wave-packet state after the final $\pi/2$ pulse is composed of two elements, one that went through the lens system and one that did not, such that the elements that traveled along the arm without the lens system will have larger effective widths (since the output of the lens system is smaller than its input). The two states will be sufficiently separated, then, when the state- $|3\rangle$ component has traveled far enough in the $+y$ direction after the final $\pi/2$ pulse such that there is no overlap of the larger effective widths. Since we know that photon recoil gives the state- $|3\rangle$ component an additional momentum of $2\hbar k$ in the $+y$ direction, we have $mv=2\hbar k$. Also, it can be shown that the effective width of a wave packet after passing through free space for a time T is $\sigma\sqrt{1+(T/\tau)}$, where $\tau=m\sigma/\hbar$ and σ is the original effective width. Therefore, for sufficient spatial separation of the states (assuming that the time between the

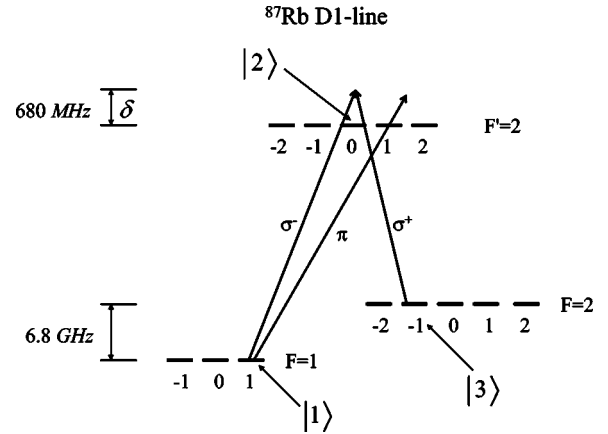


FIG. 3. The proposed transition scheme. We consider $5^2S_{1/2}(F=1, m=1) \equiv |1\rangle$, $5^2P_{1/2}(F'=2, m=0) \equiv |2\rangle$, and $5^2S_{1/2}(F=2, m=-1) \equiv |3\rangle$, where the quantization axis corresponds to the \hat{y} direction in Fig. 1. σ^- -polarized light excites the $|1\rangle \leftrightarrow |2\rangle$ transition and σ^+ -polarized light excites the $|2\rangle \leftrightarrow |3\rangle$ transition. Both lasers are detuned by 680 MHz. For the $\pi/2$, π , and $\pi/2$ pulses, the above mentioned two transitions are simultaneously excited. For the light-shift-based lens system, as shown in the picture, a different transition from the state $|1\rangle$ to the sublevel $5^2P_{1/2}(F'=2, m=1)$ is used, and π -polarized light is applied. Since this field is highly detuned from the $F=2 \leftrightarrow F'=2$ transitions, the light shift for $|3\rangle$ can be neglected.

final $\pi/2$ pulse and the substrate is on the order of T_B) we need $v \times T_B \geq \sigma_{\text{in}} \sqrt{1+(T_B/\tau)}$.

To summarize, our restrictions are

$$T_A \leq 10 \text{ s}, \quad T_B \leq 10^{-2} T_A,$$

and

$$\frac{\hbar T_A}{m\sigma_{\text{in}}} \geq 10^{-3} \text{ m}, \quad \frac{2\hbar}{m} T_B \geq \sigma_{\text{in}} \sqrt{1 + \left(\frac{\hbar T_B}{m\sigma_{\text{in}}}\right)}.$$

After using some simple algebra, we find that the first three restrictions are satisfied if we apply the following

$$\sigma_{\text{in}} \leq 10^{-5} \text{ m}, \quad \sim \sigma_{\text{in}}/T_A \leq 10^{-6} \text{ m/s}, \quad T_B \leq 10^{-2} T_A.$$

We can, for example, choose $\sigma_{\text{in}}=10^{-5}$ m, $T_A \sim 10$ s, $T_B \sim 10^{-1}$ s. A simple check shows that these choices also satisfy the fourth restriction.

Finally, since our proposed lithography scheme involves the use of a single atom at a time, it entails the drawback of being very slow. To make this type of lithography truly practical, a Bose-Einstein condensate [4,5] would have to be used instead of a single-atomic wave packet.

B. Proposed ^{87}Rb levels and transitions for the nanolithography scheme

For practical implementation of our three-level atom, we use the D1 transitions in ^{87}Rb [40]. Figure 3 illustrates. One of the restrictions is that, in order to be able to neglect spontaneous emission, we need for each single transition

$$\left(\frac{g_0}{\delta}\right)^2 \times \Gamma \times \tau \ll 1, \quad (35)$$

where g_0 is the Rabi frequency, δ is the detuning, Γ is the decay rate, and τ is the interaction time. Both the Raman pulse scheme and the light shift scheme also require

$$g_0 \ll \delta. \quad (36)$$

We have the following relation:

$$g_{0,\max}^2 = \left(\frac{I_{\max}}{I_{\text{sat}}}\right)\Gamma^2. \quad (37)$$

If we assume $I_{\text{sat}}=3 \text{ mW/cm}^2$, $I_{\max}=2 \text{ mW/mm}^2$, and $\Gamma = 3.33 \times 10^7 \text{ s}^{-1}$, we find that $g_{0,\max} \approx 8.6 \times 10^9 \text{ Hz}$.

We choose the relevant Raman Λ transition levels to be $|1\rangle \equiv 5^2S_{1/2}(F=1, m=1)$, $|2\rangle \equiv 5^2P_{1/2}(F=2, m=0)$, and $5^2S_{1/2}(F=2, m=-1) \equiv |3\rangle$, with the quantization axis being in the \hat{y} direction of Fig. 1. The energy difference between the levels $|1\rangle$ and $|2\rangle$ is 6.8 GHz. The $|1\rangle \rightarrow |2\rangle$ and $|2\rangle \rightarrow |3\rangle$ transitions are performed by simultaneously applying σ^- - and σ^+ -polarized fields. The two ground states $|1\rangle$ and $|3\rangle$ have equal and opposite g factors, so that they will experience the same force for a given magnetic field gradient used for slowing them. For the ac-Stark shift, we apply π -polarized light that couples $|1\rangle$ to the $F'=2, m=1$ excited state. Because this field is highly detuned from the $F=2 \leftrightarrow F'=2$ transition, the corresponding light shift of level $|3\rangle$ can be neglected.

In order to satisfy the constraint that the Rabi frequency be much less than the detuning, we choose $g_0=68 \text{ MHz}$. This is well below the maximum limit calculated above.

As far as the interaction time for the $\pi/2$ and π pulse scheme, it is the Raman Rabi frequency that is of interest:

$$\Omega = \frac{g_0^2}{2\delta}. \quad (38)$$

Using this in Eq. (36), we get

$$\begin{aligned} 2\frac{\Omega}{\delta} \times \Gamma \times \tau &\ll 1 \\ \Rightarrow \Omega \tau &\ll \frac{\delta}{2\Gamma}. \end{aligned} \quad (39)$$

Plugging in the chosen value for δ and the typical value of 33.33 MHz for Γ , we find that $\Omega \tau \ll 10.2$. We can satisfy this restraint by choosing $\Omega \tau = \pi$ for the π pulse and half as much for the $\pi/2$ pulse, giving a pulse duration of $\tau = \pi/\Omega \approx 924 \text{ ns}$ for a π pulse and $\tau \approx 462 \text{ ns}$ for a $\pi/2$ pulse.

For the light shift we use the same π -polarized excitation of state $|1\rangle \rightarrow 5^2P_{1/2}(F'=2, m=1)$ as shown in Fig. 3. The time constraint in this case is

$$\frac{g_0^2}{4\delta} \tau = 2\pi. \quad (40)$$

This gives an interaction time of $\tau \approx 3.7 \mu\text{s}$. Ideally, the light shift pulse will only interact with the wave packet in state $|1\rangle$. This may actually be possible if we choose T_A to be

large enough such that the two states gain enough of a transverse separation. If, as by example above, we choose $T_A \sim 10 \text{ s}$, then the separation between the two states will be on the order of a centimeter and there will be virtually no overlap between the two components of the wave packet in the separate arms. The light pulse could then simply intercept only state $|3\rangle$. If, however, the situation is such that the states are overlapping, then state $|1\rangle$ will also experience the light shift, but it will be about a factor of ten less because of the detuning being approximately ten times larger for it than for the state- $|3\rangle$ transition.

VI. NUMERICAL EXPERIMENTS

The numerical implementation of our lithography scheme was done by distributing the wave packets across finite meshes and then evolving them according to the Schrödinger equation. This evolution was done in both position and momentum space according to expediency. To go between the two domains, we used two-dimensional Fourier transform and inverse Fourier transform algorithms.

The initial wave packet was taken in momentum space and completely in internal state $|1\rangle$. Specifically, the wave packet was given by the Fourier transform of Eq. (1):

$$|\Phi_e(\vec{k}, t=0)\rangle = \sqrt{\frac{\sigma}{\sqrt{\pi}}} \exp\left(\frac{-|\vec{k}|^2 \sigma^2}{2}\right). \quad (41)$$

The evolution of the wave packets in the π and $\pi/2$ pulses was done in momentum space in order to be able to account for the different detunings that result for each momentum component due to the Doppler shift. Specifically, we numerically solved Eq. (B15) for the different components of the k -space wave packet mesh, then applied the inverse of the transformation matrix given by Eq. (B9) to go to the original basis.

Outside of the lens system, the free-space evolution of the wave packets was also done in momentum space. This was achieved easily by using Eqs. (A4). Within the lens system, however, it was more computationally efficient to use Eq. (31) for the free-space evolution because of the need to apply the lenses in position space. The results of using Eq. (32) were initially cross-checked with the results of using Eqs. (A4) and were found to agree.

Figure 4(a) is a targeted (arbitrary) pattern. Figures 4(b) and 4(c) demonstrate the formation of the arbitrary pattern by interference of the state- $|1\rangle$ wave packets at the output of the interferometer. Both figures were the result of applying the same arbitrary pattern phase, but Fig. 4(b) was formed without any shrinking implemented (i.e., $T_A=T_B$). Figure 4(c), however, demonstrates the shrinking ability of the lens system by yielding a version of Fig. 4(b) that is scaled by a factor of $2(T_A/T_B=2)$. The length scales are in arbitrary units due to the use of naturalized units for the sake of computational viability.

VII. SUGGESTIONS FOR EXTENSION TO BEC

As mentioned above, in order to make the lithography scheme truly practical, a Bose-Einstein condensate is re-

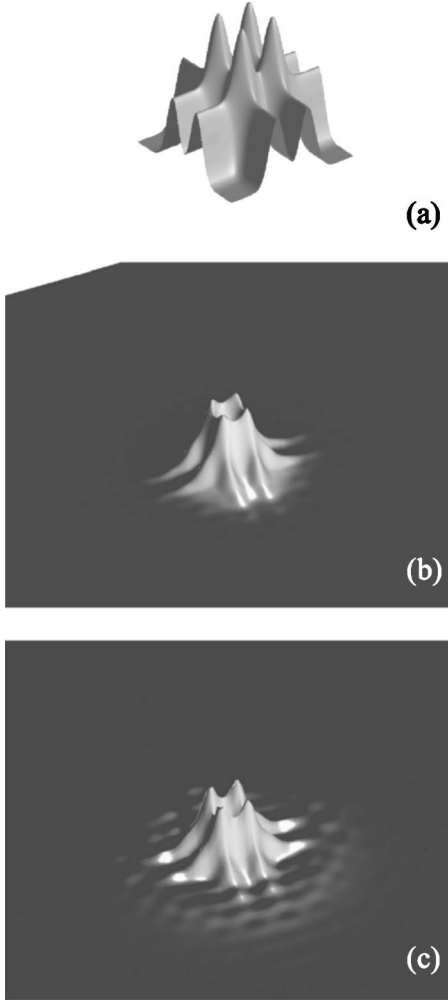


FIG. 4. (a) A targeted arbitrary (e.g., a tic-tac-toe board here) image. (b) The arbitrary image is now formed with the lens system in place, but without any scaling. We see that it is a more complex pattern than just a simple periodic structure such as sinusoidal fringes. (c) The same image as in (b) is formed with the lens system still in place, but a scaling factor of 2 has been used to shrink the pattern.

quired in place of the single atom. Indeed, the self-interference of a BEC has already been demonstrated [41,42]. The difficulty in using the BEC for controlled imaging, however, arises from the nonlinear term in the Gross-Pitaevskii equation (GPE). Our lens system, for example, would not be valid as it was developed from the linear SE.

One approach to getting around this problem is to try to eliminate the nonlinear term in the GPE. Specifically, the GPE for the BEC takes the form

$$i\hbar \frac{\partial \Psi}{\partial t} = \left(\frac{-\hbar^2}{2m} \nabla^2 + V + U_0 |\Psi|^2 \right) \Psi, \quad (42)$$

where the nonlinear term coefficient is $U_0 = 4\pi\hbar^2 a/m$ and a is the scattering length for the atom. It has been demonstrated for ^{87}Rb that the scattering length can be tuned over a broad range by exposing the BEC to magnetic fields of varying strength near Feshbach resonances [43,44]. The relation-

ship between the scattering length and the applied magnetic field B when near a Feshbach resonance can be written as

$$a = a_{\text{bg}} \left(1 - \frac{\Delta}{B - B_{\text{peak}}} \right), \quad (43)$$

where a_{bg} is the background scattering length, B_{peak} is the resonance position, and $\Delta = B_{\text{zero}} - B_{\text{peak}}$. Setting $B = B_{\text{zero}}$ would therefore set the scattering length to zero and eliminate the nonlinear term in the GPE. While the atom-atom interaction may not be completely eliminated in reality due to the fluctuation in density that we wish to effect through the lens system, it is worth investigating if it could be made to be negligible over an acceptable range. We could then use our previously developed lens system to perform the imaging and thereby interfere a large number of atoms simultaneously. Alternatively, one must redevelop the design of the lenses and the imaging optics as applied to the equation of motion for a BEC [Eq. (42)] for a nonzero value of U_0 . This effort is in progress.

ACKNOWLEDGMENTS

This work was supported by DARPA Grant No. F30602-01-2-0546 under the QUIST program, ARO Grant No. DAAD19-001-0177 under the MURI program, NRO Grant No. NRO-000-00-C-0158, and AFOSR Grants: No. F49620-02-1-0400 and No. FA9550-04-1-0189.

APPENDIX A: STATE EVOLUTION IN FREE SPACE

In free space, the Hamiltonian can be expressed in the momentum domain as

$$H = \int \int \sum_{n=1}^3 \left(\frac{p_x^2 + p_y^2}{2m} + \hbar \omega_n \right) |n, p_x, p_y\rangle \langle n, p_x, p_y| dp_x dp_y, \quad (A1)$$

where ω_n is the frequency corresponding to the eigenenergy of internal state $|n\rangle$. For a single momentum component ($p_x = p_{x0}$ and $p_y = p_{y0}$), the Hamiltonian for the total evolution in momentum space is given by

$$H = \begin{bmatrix} \frac{p_{x0}^2 + p_{y0}^2}{2m} + \hbar \omega_1 & 0 & 0 \\ 0 & \frac{p_{x0}^2 + p_{y0}^2}{2m} + \hbar \omega_2 & 0 \\ 0 & 0 & \frac{p_{x0}^2 + p_{y0}^2}{2m} + \hbar \omega_3 \end{bmatrix}. \quad (A2)$$

Using this in the SE, we get the equations of the amplitude evolution in momentum space:

$$\begin{aligned} \dot{C}_1(p_{x0}, p_{y0}, t) &= -\frac{i}{\hbar} \left(\frac{p_{x0}^2 + p_{y0}^2}{2m} + \hbar \omega_1 \right) C_1(p_{x0}, p_{y0}, t), \\ \dot{C}_2(p_{x0}, p_{y0}, t) &= -\frac{i}{\hbar} \left(\frac{p_{x0}^2 + p_{y0}^2}{2m} + \hbar \omega_2 \right) C_2(p_{x0}, p_{y0}, t), \end{aligned} \quad (A3)$$

$$\dot{C}_3(p_{x0}, p_{y0}, t) = -\frac{i}{\hbar} \left(\frac{p_{x0}^2 + p_{y0}^2}{2m} + \hbar\omega_3 \right) C_3(p_{x0}, p_{y0}, t).$$

These yield the solutions

$$\begin{aligned} C_1(p_{x0}, p_{y0}, t) &= C_1(p_{x0}, p_{y0}, 0) e^{-i[(p_{x0}^2 + p_{y0}^2)/2m\hbar + \omega_1]t}, \\ C_2(p_{x0}, p_{y0}, t) &= C_2(p_{x0}, p_{y0}, 0) e^{-i[(p_{x0}^2 + p_{y0}^2)/2m\hbar + \omega_2]t}, \\ C_3(p_{x0}, p_{y0}, t) &= C_3(p_{x0}, p_{y0}, 0) e^{-i[(p_{x0}^2 + p_{y0}^2)/2m\hbar + \omega_3]t}. \end{aligned} \quad (\text{A4})$$

We see that if the wave function is known at time $t=0$, then after a duration of time T in free space, the wave function becomes

$$\begin{aligned} |\Psi(\vec{r}, t=T)\rangle &= \frac{1}{2\pi} \int \int [C_1(p_x, p_y, 0) e^{-i[(p_x^2 + p_y^2)/2m\hbar + \omega_1]T} |1, p_x, p_y\rangle \\ &+ C_2(p_x, p_y, 0) e^{-i[(p_x^2 + p_y^2)/2m\hbar + \omega_2]T} |2, p_x, p_y\rangle \\ &+ C_3(p_x, p_y, 0) e^{-i[(p_x^2 + p_y^2)/2m\hbar + \omega_3]T} |3, p_x, p_y\rangle] dp_x dp_y. \end{aligned} \quad (\text{A5})$$

We can also write it as

$$\begin{aligned} |\Psi(\vec{r}, t=T)\rangle &= e^{-i\omega_1 T} c_1(0) |1, \Psi_e(\vec{r}, T)\rangle + e^{-i\omega_2 T} c_2(0) \\ &\times |2, \Psi_e(\vec{r}, T)\rangle + e^{-i\omega_3 T} c_3(0) |3, \Psi_e(\vec{r}, T)\rangle. \end{aligned} \quad (\text{A6})$$

APPENDIX B: STATE EVOLUTION IN π AND $\pi/2$ PULSE LASER FIELDS

The electromagnetic fields encountered by the atom at points 2, 3, and 7 in Fig. 1 that act as the π and $\pi/2$ pulses are each formed by two lasers that are counterpropagating in the y - z plane parallel to the y axis. We will refer to the laser propagating in the $+y$ direction as \vec{E}_A , and the one propagating in the $-y$ direction as \vec{E}_B . In deriving the equations of motion under this excitation, we make the following assumptions: (1) the laser fields can be treated semiclassically [45], (2) the intensity profiles of the laser fields forming the π and $\pi/2$ pulses remain constant over the extent of the atomic wave packet, (3) the wavelengths of the lasers are significantly larger than the separation distance between the nucleus and electron of the atom, (4) \vec{E}_A excites only the $|1\rangle \leftrightarrow |2\rangle$ transition and \vec{E}_B only the $|3\rangle \leftrightarrow |2\rangle$ transition, (5) \vec{E}_A and \vec{E}_B are far detuned from the transitions that they excite, and (6) \vec{E}_A and \vec{E}_B are of the same intensity.

Using assumptions (1) and (2), we write the laser fields as

$$\begin{aligned} \vec{E}_A &= \vec{E}_{A0} \cos(\omega_A t - k_A \hat{y} + \phi_A) \\ &= \frac{\vec{E}_{A0}}{2} [e^{i(\omega_A t - k_A \hat{y} + \phi_A)} + e^{-i(\omega_A t - k_A \hat{y} + \phi_A)}] \end{aligned} \quad (\text{B1})$$

and

$$\begin{aligned} \vec{E}_B &= \vec{E}_{B0} \cos(\omega_B t + k_B \hat{y} + \phi_B) \\ &= \frac{\vec{E}_{B0}}{2} [e^{i(\omega_B t + k_B \hat{y} + \phi_B)} + e^{-i(\omega_B t + k_B \hat{y} + \phi_B)}] \end{aligned} \quad (\text{B2})$$

where \vec{E}_{A0} and \vec{E}_{B0} are vectors denoting the magnitude and polarization of their respective fields. Keeping in mind that our wave function is expressed in the momentum domain, we take position as an operator.

The Hamiltonian here is expressed as the sum of two parts: $H = H_0 + H_1$. The first part corresponds to the noninteraction energy:

$$H_0 = \int \int \sum_{n=1}^3 \left(\frac{p_x^2 + p_y^2}{2m} + \hbar\omega_n \right) |n, p_x, p_y\rangle \langle n, p_x, p_y| dp_x dp_y. \quad (\text{B3})$$

The second part accounts for the interaction energy, for which we use assumption (3) from above to make the electric dipole approximation and get

$$\begin{aligned} H_1 &= -e_0 \vec{\epsilon} \cdot \frac{\vec{E}_{A0}}{2} [e^{i(\omega_A t - k_A \hat{y} + \phi_A)} + e^{-i(\omega_A t - k_A \hat{y} + \phi_A)}] \\ &- e_0 \vec{\epsilon} \cdot \frac{\vec{E}_{B0}}{2} [e^{i(\omega_B t + k_B \hat{y} + \phi_B)} + e^{-i(\omega_B t + k_B \hat{y} + \phi_B)}] \end{aligned} \quad (\text{B4})$$

where $\vec{\epsilon}$ is the position vector of the electron, and e_0 is the electron charge. Now, seeing that expressions of the form $\langle n | \vec{\epsilon} \cdot \vec{E}_{A0} | n \rangle$ and $\langle n | \vec{\epsilon} \cdot \vec{E}_{B0} | n \rangle$ are zero, and using assumption (4), we can express Eq. (B4) as

$$\begin{aligned} H_1 &= \int \int \left[\frac{\hbar g_A}{2} (|1, p_x, p_y\rangle \langle 2, p_x, p_y| + |2, p_x, p_y\rangle \langle 1, p_x, p_y|) \right. \\ &\times [e^{i(\omega_A t - k_A \hat{y} + \phi_A)} + e^{-i(\omega_A t - k_A \hat{y} + \phi_A)}] + \frac{\hbar g_B}{2} (|3, p_x, p_y\rangle \\ &\times \langle 2, p_x, p_y| + |2, p_x, p_y\rangle \langle 3, p_x, p_y|) [e^{i(\omega_B t + k_B \hat{y} + \phi_B)} \\ &\left. + e^{-i(\omega_B t + k_B \hat{y} + \phi_B)}] \right] dp_x dp_y, \end{aligned} \quad (\text{B5})$$

where we let $g_A = \langle 1 | \vec{\epsilon} \cdot \vec{E}_{A0} | 2 \rangle = \langle 2 | \vec{\epsilon} \cdot \vec{E}_{A0} | 1 \rangle$ and $g_B = \langle 3 | \vec{\epsilon} \cdot \vec{E}_{B0} | 2 \rangle = \langle 2 | \vec{\epsilon} \cdot \vec{E}_{B0} | 3 \rangle$. Finally, we can use the identities [39]

$$e^{ik\hat{y}} = \sum_n \int \int |n, p_x, p_y\rangle \langle n, p_x, p_y - \hbar k| dp_x dp_y, \quad (\text{B6a})$$

$$e^{-ik\hat{y}} = \sum_n \int \int |n, p_x, p_y\rangle \langle n, p_x, p_y + \hbar k| dp_x dp_y, \quad (\text{B6b})$$

and the rotating wave approximation [45] in Eq. (B5) to give

$$\begin{aligned}
H_1 = & \int \int \left[\frac{\hbar g_A}{2} e^{i(\omega_A t + \phi_A)} |1, p_x, p_y\rangle \langle 2, p_x, p_y + \hbar k_A| \right. \\
& + \frac{\hbar g_A}{2} e^{-i(\omega_A t + \phi_A)} |2, p_x, p_y + \hbar k_A\rangle \langle 1, p_x, p_y| + \frac{\hbar g_B}{2} e^{i(\omega_B t + \phi_B)} \\
& \times |3, p_x, p_y + \hbar k_A + \hbar k_B\rangle \langle 2, p_x, p_y + \hbar k_A| + \frac{\hbar g_B}{2} e^{-i(\omega_B t + \phi_B)} \\
& \left. \times |2, p_x, p_y + \hbar k_A\rangle \langle 3, p_x, p_y + \hbar k_B + \hbar k_A| \right] dp_x dp_y. \quad (B7)
\end{aligned}$$

We note that the full interaction between the internal states $|1\rangle$, $|2\rangle$, and $|3\rangle$ occurs across groups of three different momentum components: $|p_x, p_y\rangle$, $|p_x, p_y + \hbar k_A\rangle$, and $|p_x, p_y + \hbar k_A + \hbar k_B\rangle$. This can be understood physically in terms of photon absorption and emission and conservation of momentum. Keeping in mind assumption (4), if an atom begins in

state $|1, p_{x0}, p_{y0}\rangle$ and absorbs a photon from field \vec{E}_A , it will transition to internal state $|2\rangle$ because it has become excited, but it will also gain the momentum of the photon ($\hbar k_A$) traveling in the $+y$ direction. It will therefore end up in state $|2, p_{x0}, p_{y0} + \hbar k_A\rangle$. Now the atom is able to interact with field \vec{E}_B , which can cause stimulated emission of a photon with momentum $\hbar k_B$ in the $-y$ direction. If such a photon is emitted, the atom itself will gain an equal momentum in the opposite direction, bringing it into external state $|p_{x0}, p_{y0} + \hbar k_A + \hbar k_B\rangle$. The atom will also make an internal transition to state $|3\rangle$ because of the deexcitation. The total state will now be $|3, p_{x0}, p_{y0} + \hbar k_A + \hbar k_B\rangle$. We thereby see that our mathematics is corroborated by physical intuition.

Getting back to the Hamiltonian, we look at the general case of one momentum grouping so that we get in matrix form $H = H_0 + H_1$ from Eqs. (B3) and (B7):

$$H = \begin{bmatrix} \frac{p_x^2 + p_y^2}{2m} + \hbar\omega_1 & \frac{\hbar g_A}{2} e^{i(\omega_A t + \phi_A)} & 0 \\ \frac{\hbar g_A}{2} e^{-i(\omega_A t + \phi_A)} & \frac{p_x^2 + (p_y + \hbar k_A)^2}{2m} + \hbar\omega_2 & \frac{\hbar g_B}{2} e^{-i(\omega_B t + \phi_B)} \\ 0 & \frac{\hbar g_B}{2} e^{i(\omega_B t + \phi_B)} & \frac{p_x^2 + (p_y + \hbar k_A + \hbar k_B)^2}{2m} + \hbar\omega_3 \end{bmatrix}. \quad (B8)$$

In order to remove the time dependence we apply some transformation Q [39] of the form

$$Q = \begin{bmatrix} e^{i(\theta_1 t + \phi_1)} & 0 & 0 \\ 0 & e^{i(\theta_2 t + \phi_2)} & 0 \\ 0 & 0 & e^{i(\theta_3 t + \phi_3)} \end{bmatrix}, \quad (B9)$$

so that the SE becomes

$$i\hbar \frac{\partial |\tilde{\Psi}\rangle}{\partial t} = \tilde{H} |\tilde{\Psi}\rangle, \quad (B10)$$

where $|\tilde{\Psi}\rangle = Q|\Psi\rangle$ and $\tilde{H} = QHQ^{-1} + i\hbar(\partial Q/\partial t)Q^{-1}$. The matrix representation is

$$\tilde{H} = \begin{bmatrix} \frac{p_x^2 + p_y^2}{2m} + \hbar\omega_1 - \hbar\theta_1 & \frac{\hbar g_A}{2} e^{i(\omega_A + \theta_1 - \theta_2)t + i(\phi_A + \phi_1 - \phi_2)} & 0 \\ \frac{\hbar g_A}{2} e^{-i(\omega_A + \theta_1 - \theta_2)t - i(\phi_A + \phi_1 - \phi_2)} & \frac{p_x^2 + (p_y + \hbar k_A)^2}{2m} + \hbar\omega_2 - \hbar\theta_2 & \frac{\hbar g_B}{2} e^{-i(\omega_B + \theta_3 - \theta_2)t - i(\phi_B + \phi_3 - \phi_2)} \\ 0 & \frac{\hbar g_B}{2} e^{i(\omega_B + \theta_3 - \theta_2)t + i(\phi_B + \phi_3 - \phi_2)} & \frac{p_x^2 + (p_y + \hbar k_A + \hbar k_B)^2}{2m} + \hbar\omega_3 - \hbar\theta_3 \end{bmatrix}. \quad (B11)$$

Choosing $\theta_1 = -\omega_A$, $\theta_2 = 0$, $\theta_3 = -\omega_B$, $\phi_1 = -\phi_A$, $\phi_2 = 0$, and $\phi_3 = -\phi_B$, Eq. (B11) becomes

$$\tilde{H} = \begin{bmatrix} E_1(p_x, p_y) + \hbar\omega_1 + \hbar\omega_A & \frac{\hbar g_A}{2} & 0 \\ \frac{\hbar g_A}{2} & E_2(p_x, p_y) + \hbar\omega_2 & \frac{\hbar g_B}{2} \\ 0 & \frac{\hbar g_B}{2} & E_3(p_x, p_y) + \hbar\omega_3 + \hbar\omega_B \end{bmatrix}, \quad (\text{B12})$$

where we have taken

$$E_1(p_x, p_y) = \frac{p_x^2 + p_y^2}{2m}, \quad (\text{B13a})$$

$$E_2(p_x, p_y) = \frac{p_x^2 + (p_y + \hbar k_A)^2}{2m}, \quad (\text{B13b})$$

$$E_3(p_x, p_y) = \frac{p_x^2 + (p_y + \hbar k_A + \hbar k_B)^2}{2m}. \quad (\text{B13c})$$

In order to further simplify the analysis, we set the zero energy at $E_1(p_{x0}, p_{y0}) + \hbar\omega_1 + \hbar\omega_A$ for some specific momentum group with $p_x = p_{x0}$ and $p_y = p_{y0}$. Also, since ω_A and ω_B can be chosen independently, we can let $E_3(p_{x0}, p_{y0}) + \hbar\omega_3 + \hbar\omega_B = E_1(p_{x0}, p_{y0}) + \hbar\omega_1 + \hbar\omega_A$. With the energies thus set, Eq. (B12) becomes

$$\tilde{H} = \begin{bmatrix} 0 & \frac{\hbar g_A}{2} & 0 \\ \frac{\hbar g_A}{2} & -\delta & \frac{\hbar g_B}{2} \\ 0 & \frac{\hbar g_B}{2} & 0 \end{bmatrix}, \quad (\text{B14})$$

where $\delta = [E_1(p_{x0}, p_{y0}) + \hbar\omega_1 + \hbar\omega_A] - [E_2(p_{x0}, p_{y0}) + \hbar\omega_2]$. Using this Hamiltonian in Eq. (B10), we get the equations of motion as

$$\dot{\tilde{C}}_1(p_{x0}, p_{y0}, t) = -i \frac{g_A}{2} \tilde{C}_2(p_{x0}, p_{y0} + \hbar k_A, t), \quad (\text{B15a})$$

$$\begin{aligned} \dot{\tilde{C}}_2(p_{x0}, p_{y0} + \hbar k_A, t) = & -i \frac{g_A}{2} \tilde{C}_1(p_{x0}, p_{y0}, t) + i \delta \tilde{C}_2(p_{x0}, p_{y0} \\ & + \hbar k_A, t) - i \frac{g_B}{2} \tilde{C}_3(p_{x0}, p_{y0} + \hbar k_A \\ & + \hbar k_B, t), \end{aligned} \quad (\text{B15b})$$

$$\dot{\tilde{C}}_3(p_{x0}, p_{y0} + \hbar k_A + \hbar k_B, t) = -i \frac{g_B}{2} \tilde{C}_2(p_{x0}, p_{y0} + \hbar k_A, t). \quad (\text{B15c})$$

Assumption (5) allows us to make the adiabatic approximation so that we can set $\dot{\tilde{C}}_2(p_{x0}, p_{y0}, t) \approx 0$, and assumption

(6) gives us $g_A = g_B = g_0$. Equations (B15) then simplify to

$$\begin{aligned} \dot{\tilde{C}}_1(p_{x0}, p_{y0}, t) = & -i \frac{g_0^2}{4\delta} \tilde{C}_1(p_{x0}, p_{y0}, t) \\ & - i \frac{g_0^2}{4\delta} \tilde{C}_3(p_{x0}, p_{y0} + \hbar k_A + \hbar k_B, t), \end{aligned} \quad (\text{B16a})$$

$$\begin{aligned} \dot{\tilde{C}}_3(p_{x0}, p_{y0} + \hbar k_A + \hbar k_B, t) = & -i \frac{g_0^2}{4\delta} \tilde{C}_1(p_{x0}, p_{y0}, t) \\ & - i \frac{g_0^2}{4\delta} \tilde{C}_3(p_{x0}, p_{y0} + \hbar k_A + \hbar k_B, t), \end{aligned} \quad (\text{B16b})$$

where we have chosen to neglect state C_2 from here on due to the adiabatic approximation. We can now use another transformation on this system to make it more tractable. Let

$$\tilde{\tilde{C}}_1(p_{x0}, p_{y0}, t) = \tilde{C}_1(p_{x0}, p_{y0}, t) e^{i(g_0^2/4\delta)t}, \quad (\text{B17a})$$

$$\tilde{\tilde{C}}_3(p_{x0}, p_{y0} + \hbar k_A + \hbar k_B, t) = \tilde{C}_3(p_{x0}, p_{y0} + \hbar k_A + \hbar k_B, t) e^{i(g_0^2/4\delta)t}. \quad (\text{B17b})$$

The system in Eqs. (B16) then becomes

$$\dot{\tilde{\tilde{C}}}_1(p_{x0}, p_{y0}, t) = -i \frac{g_0^2}{4\delta} \tilde{\tilde{C}}_3(p_{x0}, p_{y0} + \hbar k_A + \hbar k_B, t), \quad (\text{B18a})$$

$$\dot{\tilde{\tilde{C}}}_3(p_{x0}, p_{y0} + \hbar k_A + \hbar k_B, t) = -i \frac{g_0^2}{4\delta} \tilde{\tilde{C}}_1(p_{x0}, p_{y0}, t). \quad (\text{B18b})$$

Solving this and reversing the transformations of Eqs. (B17) and (B9), we arrive at

$$\begin{aligned} C_1(p_{x0}, p_{y0}, t) = & C_1(p_{x0}, p_{y0}, 0) \cos\left(\frac{\Omega}{2}t\right) \\ & - i e^{i(\omega_A - \Omega/2)t + i\phi_A} \left[C_3(p_{x0}, p_{y0} + \hbar k_A \right. \\ & \left. + \hbar k_B, 0) e^{-i(\omega_B - \Omega/2)t - i\phi_B} \sin\left(\frac{\Omega}{2}t\right) \right], \end{aligned} \quad (\text{B19a})$$

$$\begin{aligned}
& C_3(p_{x0}, p_{y0} + \hbar k_A + \hbar k_B, t) \\
&= -ie^{i(\omega_B - \Omega/2)t + i\phi_B} \\
&\quad \times \left[C_1(p_{x0}, p_{y0}, 0) e^{-i(\omega_A - \Omega/2)t - i\phi_A} \sin\left(\frac{\Omega}{2}t\right) \right] \\
&\quad + C_3(p_{x0}, p_{y0} + \hbar k_A + \hbar k_B, 0) \cos\left(\frac{\Omega}{2}t\right), \quad (\text{B19b})
\end{aligned}$$

where we let $\Omega = g_0^2/2\delta$. It should be noted, however, that these solutions were arrived at only for the specific momen-

tum group where $p_x = p_{x0}$ and $p_y = p_{y0}$. This was the case where both laser fields were equally far detuned. Other momentum groups will have slightly different solutions due to the Doppler shift, which causes the detunings to be perturbed. For a more accurate description, we need to numerically solve each momentum group's original three equations of motion without making any approximations. This is what we do in our computational model. For a basic phenomenological understanding of the interferometer, however, it is sufficient to assume that the above analytical solution is accurate for all momentum components.

-
- [1] *Handbook of Micro-lithography, Micromachining and Micro-fabrication*, edited by P. Rai-Choudhury, SPIE Press, Bellingham, WA (1979).
- [2] *Microlithography Science and Technology*, edited by J. R. Sheats and Bruce W. Smith (Marcel Dekker, New York, 1997) Chap. 7.
- [3] Joseph W. Goodman, *Introduction To Fourier Optics* (McGraw-Hill, New York, 1996).
- [4] M. H. Anderson *et al.*, *Science* **269**, 198 (1995).
- [5] K. B. Davis *et al.*, *Phys. Rev. Lett.* **75**, 3969 (1995).
- [6] C. J. Borde, *Phys. Lett. A* **140**, 10 (1989).
- [7] M. Kasevich and S. Chu, *Phys. Rev. Lett.* **67**, 181 (1991).
- [8] L. Gustavson, P. Bouyer, and M. A. Kasevich, *Phys. Rev. Lett.* **78**, 2046 (1997).
- [9] M. J. Snadden, J. M. McGuirk, P. Bouyer, K. G. Haritos, and M. A. Kasevich, *Phys. Rev. Lett.* **81**, 971 (1998).
- [10] J. M. McGuirk, M. J. Snadden, and M. A. Kasevich, *Phys. Rev. Lett.* **85**, 4498 (2000).
- [11] Y. Tan, J. Morzinski, A. V. Turukhin, P. S. Bhatia, and M. S. Shahriar, *Opt. Commun.* **206**, 141 (2002).
- [12] D. Keith, C. Ekstrom, Q. Turchette, and D. E. Pritchard, *Phys. Rev. Lett.* **66**, 2693 (1991).
- [13] J. H. Thywissen and M. Prentiss, e-print physics/0209084.
- [14] B. Brezger *et al.*, *Europhys. Lett.* **46**, 148 (1999).
- [15] R. Stützel *et al.*, *J. Opt. B: Quantum Semiclassical Opt.* **5**, S164 (2003).
- [16] D. S. Weiss, B. C. Young, and S. Chu, *Phys. Rev. Lett.* **70**, 2706 (1993).
- [17] T. Pfau *et al.*, *Phys. Rev. Lett.* **71**, 3427 (1993).
- [18] U. Janicke and M. Wilkens, *Phys. Rev. A* **50**, 3265 (1994).
- [19] R. Grimm, J. Soding and Yu. B. Ovchinnikov, *Opt. Lett.* **19**, 658 (1994).
- [20] T. Pfau, C. S. Adams, and J. Mlynek, *Europhys. Lett.* **21**, 439 (1993).
- [21] K. Johnson, A. Chu, T. W. Lynn, K. Berggren, M. S. Shahriar, and M. G. Prentiss, *Opt. Lett.* **20**, 1310 (1995).
- [22] M. S. Shahriar, Y. Tan, M. Jheeta, J. Morzinsky, P. R. Hemmer, and P. Pradhan, e-print quant-ph/0311163; *J. Opt. Soc. Am. B* (2005) (in press).
- [23] B. E. A. Saleh and M. C. Teich, *Fundamentals of Photonics* (Wiley-Interscience, New York, 1991).
- [24] L. Dobrek *et al.*, *Phys. Rev. A* **60**, R3381 (1999).
- [25] J. Denschlag *et al.*, *Science* **287**, 97 (2000).
- [26] S. Swain, *J. Phys. B* **15**, 3405 (1982).
- [27] M. Prentiss, N. Bigelow, M. S. Shahriar, and P. Hemmer, *Opt. Lett.* **16**, 1695 (1991).
- [28] P. R. Hemmer, M. S. Shahriar, M. Prentiss, D. Katz, K. Berggren, J. Mervis, and N. Bigelow, *Phys. Rev. Lett.* **68**, 3148 (1992).
- [29] M. S. Shahriar and P. Hemmer, *Phys. Rev. Lett.* **65**, 1865 (1990).
- [30] M. S. Shahriar, P. Hemmer, D. P. Katz, A. Lee, and M. Prentiss, *Phys. Rev. A* **55**, 2272 (1997).
- [31] P. Meystre, *Atom Optics* (Springer Verlag, Berlin, 2001).
- [32] *Atom Interferometry*, edited by P. Berman (Academic Press, New York, 1997).
- [33] *Fiber Optic Rotation Sensors*, edited by S. Ezekiel and A. Arditty (Springer-Verlag, Berlin, 1982).
- [34] J. McKeever *et al.*, *Phys. Rev. Lett.* **90**, 133602 (2003).
- [35] S. J. van Enk *et al.*, *Phys. Rev. A* **64**, 013407 (2001).
- [36] A. C. Doherty *et al.*, *Phys. Rev. A* **63**, 013401 (2001).
- [37] K. K. Berggren *et al.*, *Science* **269**, 1255 (1995).
- [38] S. B. Hill *et al.*, *Appl. Phys. Lett.* **74**, 2239 (1999).
- [39] M. S. Shahriar, M. Jheeta, Y. Tan, P. Pradhan, and A. Gangat, *Opt. Commun.* **243**, 183 (2004).
- [40] A. Corney, *Atomic and Laser Spectroscopy* (Oxford Science, Oxford, 1976).
- [41] M. R. Andrews *et al.*, *Science* **275**, 637 (1997).
- [42] Y. Torii *et al.*, *Phys. Rev. A* **61**, 041602 (2000).
- [43] A. Marte, T. Volz, J. Schuster, S. Dürr, G. Rempe, E. G. M. van Kempen, and B. J. Verhaar, *Phys. Rev. Lett.* **89**, 283202 (2002).
- [44] T. Volz, S. Dürr, S. Ernst, A. Marte, and G. Rempe, *Phys. Rev. A* **68**, 010702(R) (2003).
- [45] L. Allen and J. H. Eberly, *Optical Resonance and Two-Level Atoms* (Dover, New York, 1974).

B.3. Development of a Quantum Computing Architecture Using Atomic Ensembles as Quantum Bits

Summary:

Given the technical difficulties encountered in realizing a quantum computer based on NV-diamond, coupled with the prospect that it may be very difficult to achieve a very small decoherence rate in such a system (a problem endemic to all solid state QC ideas), we worked on developing alternative ideas for robust and high-fidelity quantum computing, based on atomic ensembles as quantum bits.

Current proposals focusing on neutral atoms for quantum computing are mostly based on using single atoms as quantum bits (qubits), while using cavity induced coupling or dipole–dipole interaction for two-qubit operations. An alternative approach is to use atomic ensembles as quantum bits. However, when an atomic ensemble is excited, by a laser beam matched to a two-level transition (or a Raman transition) for example, it leads to a cascade of many states as more and more photons are absorbed. In order to make use of an ensemble as a qubit, it is necessary to disrupt this cascade, and restrict the excitation to the absorption (and emission) of a single photon only. We have shown how this can be achieved by using a new type of blockade mechanism, based on the light-shift imbalance (LSI) in a Raman transition. We developed first a simple example illustrating the concept of light-shift imbalance induced blockade (LSIIB) using a multi-level structure in a single atom, and show verifications of the analytic prediction using numerical simulations. We then extended this model to show how a blockade can be realized by using LSI in the excitation of an ensemble. Specifically, we showed how the LSIIB process enables one to treat the ensemble as a two-level atom that undergoes fully deterministic Rabi oscillations between two collective quantum states, while suppressing excitations of higher order collective states.

Finally, we developed an explicit scheme that shows how such a system can be used as a quantum bit (qubit) for quantum communication and quantum computing. Specifically, we showed how to realize a controlled-NOT (CNOT) gate using the collective qubit and an easily accessible ring cavity or a tapered nano-fiber, via an extension of the so-called Pellizzari scheme. We also describe how multiple, small-scale quantum computers realized using these qubits can be linked effectively for implementing a quantum internet. We developed an explicit description of the details of the energy levels and transitions in an ^{87}Rb atom that could be used for implementing these schemes.

Reproduction of published journal papers: (5+9 pages)

This work was published in two parts, as a paper in *Optic Communications*, followed by a paper in *Physical Review A*. These two papers are reproduced below.

Light-shift imbalance induced blockade of collective excitations beyond the lowest order

M.S. Shahriar, P. Pradhan, G.S. Pati ^{*}, V. Gopal, K. Salit

EECS Department, Northwestern University, Evanston, IL 60208, United States

Received 12 February 2007; received in revised form 25 April 2007; accepted 22 May 2007

Abstract

Current proposals focusing on neutral atoms for quantum computing are mostly based on using single atoms as quantum bits (qubits), while using cavity induced coupling or dipole–dipole interaction for two-qubit operations. An alternative approach is to use atomic ensembles as quantum bits. However, when an atomic ensemble is excited, by a laser beam matched to a two-level transition (or a Raman transition) for example, it leads to a cascade of many states as more and more photons are absorbed [R.H. Dicke, *Phys. Rev.* 93 (1954) 99]. In order to make use of an ensemble as a qubit, it is necessary to disrupt this cascade, and restrict the excitation to the absorption (and emission) of a single photon only. Here, we show how this can be achieved by using a new type of blockade mechanism, based on the light-shift imbalance (LSI) in a Raman transition. We describe first a simple example illustrating the concept of light-shift imbalance induced blockade (LSIIB) using a multi-level structure in a single atom, and show verifications of the analytic prediction using numerical simulations. We then extend this model to show how a blockade can be realized by using LSI in the excitation of an ensemble. Specifically, we show how the LSIIB process enables one to treat the ensemble as a two-level atom that undergoes fully deterministic Rabi oscillations between two collective quantum states, while suppressing excitations of higher order collective states.

© 2007 Elsevier B.V. All rights reserved.

OCIS: 020.1670; 270.0270; 270.1670

Many different technologies are currently being pursued for realizing a quantum computer (QC). One of the most promising approaches involve the use of neutral atoms. This approach is particularly attractive because, in principle, it is possible to achieve very long decoherence times and very high fidelities when using neutral atoms. Current proposals for quantum computing focusing on neutral atoms are based on using single atoms as quantum bits, often while using cavity induced coupling or dipole–dipole interaction for two-qubit operations. However, given the degree of difficulties encountered in isolating and controlling single atoms, this process has proven very difficult to realize, especially on a large scale. An alternative approach

is to use atomic ensembles as quantum bits. However, when an atomic ensemble is excited, by a laser beam matched to a two-level transition (or a Raman transition) for example, it leads to a cascade of many states as more and more photons are absorbed [1–3]. In order to make use of an ensemble as a qubit, it is necessary to disrupt this cascade, and restrict the excitation to the absorption (and emission) of a single photon only. In principle, this can be achieved through the use of the so-called dipole blockade, which can be particularly efficient if Rydberg transitions are used [4,5].

Dipole blockades generally occur between individual atoms within an ensemble. In order to make use of this blockade mechanism in a manner that is consistent with a quantum computing architecture, it is necessary to control the distribution of inter-atomic distances between each

^{*} Corresponding author. Tel.: +1 847 491 7308; fax: +1 847 491 4455.
E-mail address: gspati@ece.northwestern.edu (G.S. Pati).

pair of atoms in the ensemble in a precise manner. Furthermore, in order to achieve long decoherence times, it is necessary to make use of dipole blockades based on spin–spin coupling, which is necessarily much weaker than the optical dipole–dipole coupling.

Here, we show that a new type of blockade mechanism, based on the light-shift imbalance in a Raman transition, can overcome these limitations. The resulting system does not impose any constraint on the distribution of inter-atomic distance within an ensemble. Furthermore, no dipole–dipole coupling is necessary, so that a relatively low density system can be used.

In what follows, we describe first a simple example illustrating the concept of light-shift imbalance induced blockade (LSIIB) using a multi-level structure in a single atom, and show verifications of the analytic prediction using numerical simulations. We then extend this model to show how a blockade can be realized by using LSI in the excitation of an ensemble. Specifically, we show how the LSIIB process enables one to treat the ensemble as a two-level atom that undergoes fully deterministic Rabi oscillations between two collective quantum states, while suppressing excitations of higher order collective states. We then show how this transition can be used to realize a quantum bit (qubit) embodied by the ensemble. Using multiple energy levels inside each atom, the LSIIB enables the transfer of quantum information between neighboring ensembles, as well as the realization of a C-NOT gate. In effect, this represents a generalization of the so-called Pellizari scheme for quantum information processing [6]. Furthermore, the LSIIB can be used to link two separate quantum computers (QC), by transferring the quantum state of any ensemble qubit in one QC to any ensemble qubit in another QC. In a separate paper, we discuss details of these quantum computation and communication protocols, offer practical ways to implement this scheme, and propose experiments to demonstrate the feasibility of these schemes [7].

The significance of the LSIIB process can be summarized as follows: (a) It can be used to realize a deterministic quantum bit encoded in the collective excitation states of an atomic ensemble. (b) Along with a moderate-Q cavity, it can be used to realize a two-qubit gate (e.g., a C-NOT gate) between two ensemble-based qubits. (c) It can be used to transport, deterministically, the quantum state of an ensemble qubit from one location to another separated by macroscopic distances, and (d) It can be used to establish a quantum-link between two ensembles-and-cavity based quantum computers. The scheme proposed here and expanded further in Ref. [7] therefore offers a robust technique for realizing a quantum network without using the single atom and super-cavity based approaches [8–10].

In order to illustrate the basic mechanism that underlies the LSIIB, it is convenient to consider first a simple example of a set of five levels inside a single atom, as shown in Fig. 1. Under the rotating wave approximation (RWA),

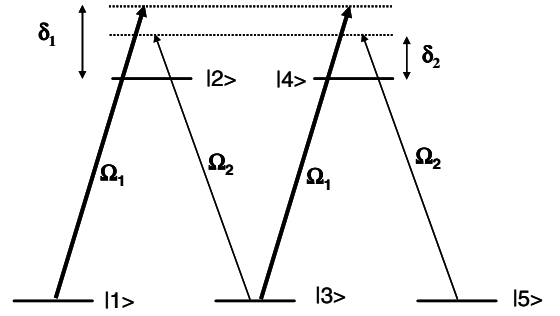


Fig. 1. Schematic illustration of a five level system, illustrating the process of LSIIB.

and the rotating wave transformation [11] (RWT), the Hamiltonian (with $\hbar = 1$) describing this interaction is given, in the bases of $\{|1\rangle, |2\rangle, |3\rangle, |4\rangle, |5\rangle\}$, by

$$H = \begin{bmatrix} \Delta/2 & \Omega_1/2 & 0 & 0 & 0 \\ \Omega_1/2 & -\delta & \Omega_2/2 & 0 & 0 \\ 0 & \Omega_2/2 & -\Delta/2 & \Omega_1/2 & 0 \\ 0 & 0 & \Omega_1/2 & -(\delta + \Delta) & \Omega_2/2 \\ 0 & 0 & 0 & \Omega_2/2 & -3\Delta/2 \end{bmatrix}, \quad (1)$$

where we have defined $\delta \equiv (\delta_1 + \delta_2)/2$ and $\Delta \equiv (\delta_1 - \delta_2)$. Under the conditions that $\delta \gg \Delta$, $\delta \gg \Omega_1$, and $\delta \gg \Omega_2$, one can eliminate the optically excited states $|2\rangle$ and $|4\rangle$ adiabatically. The effective Hamiltonian in the bases of $\{|1\rangle, |3\rangle, |5\rangle\}$ is then given by [12–15]

$$\tilde{H} = \begin{bmatrix} (\Delta/2 + \varepsilon_1) & \Omega_R/2 & 0 \\ \Omega_R/2 & [-\Delta/2 + (\varepsilon_1 + \varepsilon_2)] & \Omega_R/2 \\ 0 & \Omega_R/2 & (-3\Delta/2 + \varepsilon_2) \end{bmatrix}, \quad (2)$$

where $\Omega_R \equiv (\Omega_1\Omega_2)/2\delta$ is the Raman–Rabi frequency, and $\varepsilon_j \equiv \Omega_j^2/4\delta$ is the light-shift due to Ω_j ($j = 1, 2$). Note that the levels $|1\rangle$, $|3\rangle$ and $|5\rangle$ are light-shifted by different amounts. In general, this Hamiltonian describes a process wherein populations can oscillate between the states $|1\rangle$, $|3\rangle$ and $|5\rangle$, with the maximum amplitude in each level being determined by the relative values of the parameter.

Consider now the case where $\Omega_2 \ll \Omega_1$. Furthermore, assume that $\Delta = \varepsilon_2$. Under this condition, the Raman coupling between $|1\rangle$ and $|3\rangle$ become resonant, while the Raman coupling between $|3\rangle$ and $|5\rangle$ becomes detuned by $-(\varepsilon_1 + \varepsilon_2)$. Explicitly, this can be seen by subtracting an energy $(\varepsilon_1 + \Delta/2)$, to give

$$\tilde{\tilde{H}} = \begin{bmatrix} 0 & \Omega_R/2 & 0 \\ \Omega_R/2 & 0 & \Omega_R/2 \\ 0 & \Omega_R/2 & -(\varepsilon_1 + \varepsilon_2) \end{bmatrix}. \quad (3)$$

In the limit of $\varepsilon_2 \rightarrow 0$, $\Delta = 0$, the detuning for the $|3\rangle$ to $|5\rangle$ Raman coupling is simply $-\varepsilon_1$. For $\Omega_R \ll \varepsilon_1$ (which is the same condition as $\Omega_2 \ll \Omega_1$), the coupling to level $|5\rangle$ can be ignored. The net result is that the system will oscillate between $|1\rangle$ and $|3\rangle$. Note that this result is due to the fact that levels $|1\rangle$ and $|3\rangle$ get light-shifted by nearly the same amounts, thus remaining resonant for the Raman transition, while level $|5\rangle$ sees virtually no light-shift. Thus, the excitation to level $|5\rangle$ is essentially blockaded by the imbalance in the light-shifts.

In order to verify this blockade, we used numerical techniques to integrate the equation of motion of the system shown in Fig. 1. Since each of the optical detunings (δ_1 and δ_2) is assumed to be much larger than the Rabi frequencies and the spontaneous decay rates, the effect of the decay terms is not significant and was ignored for simplicity. The population of each of the levels with all the atoms starting in level 1, is shown in Fig. 2. These are calculated for the following parameter values: $\Delta = 0$, $\Omega_2/\Omega_1 = 0.1$, and $\delta/\Omega_1 = 10$. Analytically, the residual populations in levels $|2\rangle$ and $|4\rangle$ are expected to be of the order of $(\Omega_1/\delta)^2$ and that of level $|5\rangle$ is expected to be of the order of $(\Omega_R/\varepsilon_1)^2$, which in turn is of the order of $(\Omega_2/\Omega_1)^2$ and are consistent with the values seen here. These excitations can be suppressed further by making these ratios smaller.

Consider next the excitation of an ensemble of N atoms. To start with, we consider each atom in the ensemble to be a three-level system, as illustrated in Fig. 3. Using Dicke's model of collective excitation [1], we can show that the ensemble excitation can be represented as shown in Fig. 4. The collective states in this diagram are defined as follows:

$$\begin{aligned}
 |A\rangle &\equiv |a_1, a_2, \dots, a_N\rangle, \quad |G_1\rangle \equiv \frac{1}{\sqrt{N}} \sum_{j=1}^N |a_1, a_2, \dots, g_j, \dots, a_N\rangle, \\
 |C_1\rangle &\equiv \frac{1}{\sqrt{N}} \sum_{j=1}^N |a_1, a_2, \dots, c_j, \dots, a_N\rangle, \\
 |G_2\rangle &\equiv \frac{1}{\sqrt{N C_2}} \sum_{j,k(j \neq k)}^{N C_2} |a_1, a_2, \dots, g_j, \dots, g_k, \dots, a_N\rangle, \\
 |C_2\rangle &\equiv \frac{1}{\sqrt{N C_2}} \sum_{j,k(j \neq k)}^{N C_2} |a_1, a_2, \dots, c_j, \dots, c_k, \dots, a_N\rangle, \\
 |G_{1,1}\rangle &\equiv \frac{1}{\sqrt{2^N C_2}} \sum_{j,k(j \neq k)}^{2^N C_2} |a_1, a_2, \dots, g_j, \dots, c_k, \dots, a_N\rangle, \\
 |G_{2,1}\rangle &\equiv \frac{1}{\sqrt{Z}} \sum_{(j \neq k \neq l)}^Z |a_1, a_2, \dots, g_j, \dots, g_k, \dots, c_l, \dots, a_N\rangle, \\
 |G_{1,2}\rangle &\equiv \frac{1}{\sqrt{Z}} \sum_{(j \neq k \neq l)}^Z |a_1, a_2, \dots, g_j, \dots, c_k, \dots, c_l, \dots, a_N\rangle \quad [Z = 3^N C_3]
 \end{aligned} \tag{4}$$

The relevant coupling rates between these collective states are also illustrated in Fig. 4. Note that for large detunings, the excitations to the intermediate states $|G_1\rangle$ and $|G_{1,1}\rangle$ are small, so that higher order states such as $|G_2\rangle$ and $|G_{2,1}\rangle$ can be ignored. The remaining system looks very similar to the five level system considered earlier. (Parenthetically at this point, note that the coupling between $|G_1\rangle$ and $|C_1\rangle$ does not scale with \sqrt{N} , unlike the coupling between $|A\rangle$ and $|G_1\rangle$, which scales as \sqrt{N}). We can now proceed in a manner similar to the one described earlier. First, in the rotating wave transformation frame, the truncated, six level Hamiltonian, in the bases of $|A\rangle$, $|G_1\rangle$,

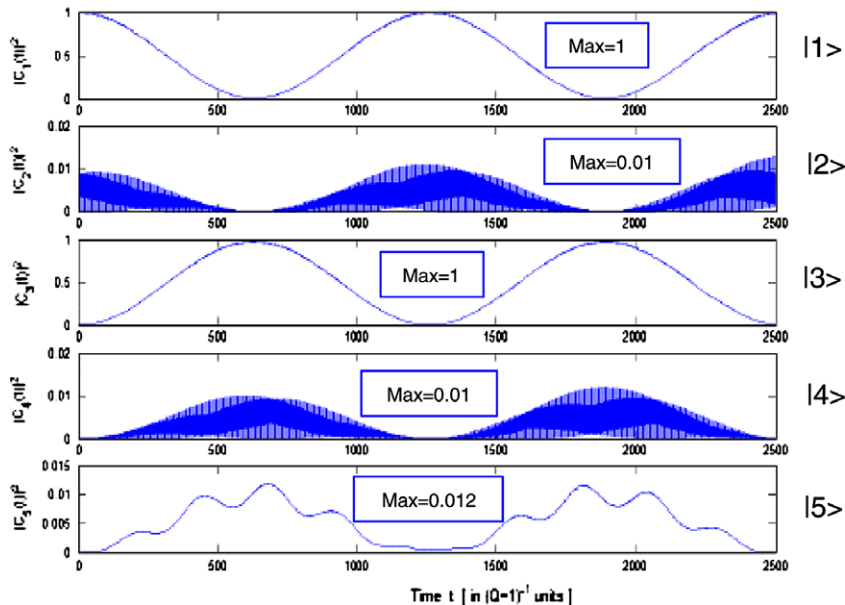


Fig. 2. Numerical results showing populations of the five level system, starting with all the atoms in level 1.

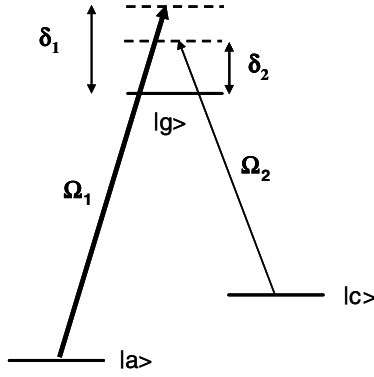


Fig. 3. Schematic illustration of a three-level transition in each atom in an ensemble.

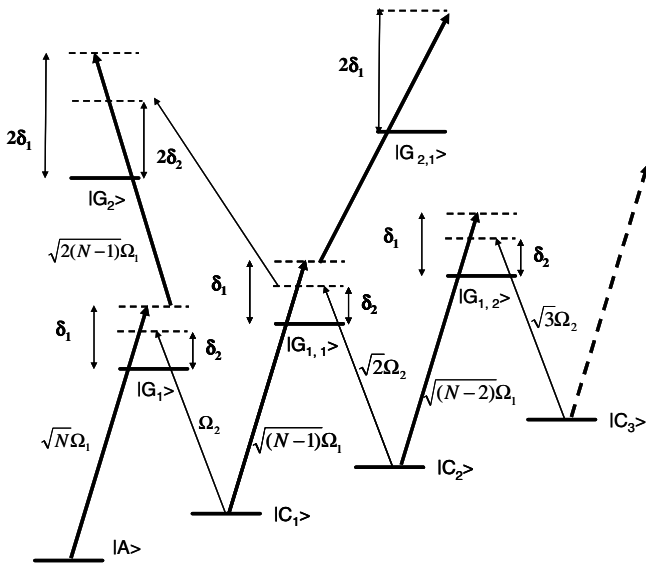


Fig. 4. Schematic illustration of the relevant collective states and the corresponding transition rates.

$|C_1\rangle$, $|G_{1,1}\rangle$, $|C_2\rangle$ and $|G_{1,2}\rangle$ is given by (the justification for not including the state $|C_3\rangle$ will be made by showing that the excitation to $|C_2\rangle$ can be suppressed, thus in turn making the amplitude of $|C_3\rangle$ insignificant)

$$H = \begin{bmatrix} \Delta/2 & \sqrt{N}\Omega_1/2 & 0 & 0 & 0 & 0 & 0 \\ \sqrt{N}\Omega_1/2 & -\delta & \Omega_2/2 & 0 & 0 & 0 & 0 \\ 0 & \Omega_2/2 & -\Delta/2 & (\sqrt{N-1})\Omega_1/2 & 0 & 0 & 0 \\ 0 & 0 & (\sqrt{N-1})\Omega_1/2 & -(\delta + \Delta) & \sqrt{2}\Omega_2/2 & 0 & 0 \\ 0 & 0 & 0 & \sqrt{2}\Omega_2/2 & -3\Delta/2 & (\sqrt{N-2})\Omega_1/2 & 0 \\ 0 & 0 & 0 & 0 & (\sqrt{N-2})\Omega_1/2 & -(\delta + 2\Delta) & 0 \\ 0 & 0 & 0 & 0 & 0 & 0 & 0 \end{bmatrix}, \quad (5)$$

where the detunings are defined just as before: $\delta \equiv (\delta_1 + \delta_2)/2$ and $\Delta \equiv (\delta_1 - \delta_2)$.

If the detunings are large compared to the transition rates, we can eliminate states $|G_1\rangle$, $|G_{1,1}\rangle$ and $|G_{1,2}\rangle$ adiabatically. Under this condition, the effective Hamiltonian

for the three remaining states ($|A\rangle$, $|C_1\rangle$, and $|C_2\rangle$) are given by (assuming $\delta \gg \Delta$)

$$\tilde{H} = \begin{bmatrix} \varepsilon_A + \Delta/2 & \Omega_{R0}/2 & 0 \\ \Omega_{R0}/2 & \varepsilon_{C1} - \Delta/2 & \sqrt{[2(N-1)/N]}\Omega_{R0}/2 \\ 0 & \sqrt{[2(N-1)/N]}\Omega_{R0}/2 & \varepsilon_{C2} - 3\Delta/2 \end{bmatrix}, \quad (6)$$

where ε_A , ε_{C1} , and ε_{C2} are the light-shifts of the states $|A\rangle$, $|C_1\rangle$, and $|C_2\rangle$, respectively and $\Omega_{R0} \equiv (\sqrt{N}\Omega_1\Omega_2)/(2\delta)$. To first order, these light-shifts are balanced, in the sense that $(\varepsilon_{C1} - \varepsilon_A) = (\varepsilon_{C2} - \varepsilon_{C1})$. This means that if the explicit two-photon detuning, Δ , is chosen to make the Raman transition between $|A\rangle$ and $|C_1\rangle$ resonant (i.e., $\Delta = (\varepsilon_{C1} - \varepsilon_A)$), then the Raman transition between $|C_1\rangle$ and $|C_2\rangle$ also becomes resonant. This balance is broken when the light-shifts are calculated to second order in intensity (which corresponds to fourth order in Ω), and the blockade shift is then given by

$$\Delta_B \equiv (\varepsilon_{C2} - \varepsilon_{C1}) - (\varepsilon_{C1} - \varepsilon_A) = -(\Omega_2^4 + \Omega_1^4)/(8\delta^3). \quad (7)$$

With the proper choice of two-photon detuning ($\Delta = (\varepsilon_{C1} - \varepsilon_A)$) to make the Raman transition between $|A\rangle$ and $|C_1\rangle$ resonant, the effective Hamiltonian (after shifting the zero of energy, and assuming $N \gg 1$) is now given by

$$\tilde{H} = \begin{bmatrix} 0 & \Omega_{R0}/2 & 0 \\ \Omega_{R0}/2 & 0 & \Omega_{R0}/\sqrt{2} \\ 0 & \Omega_{R0}/\sqrt{2} & \Delta_B \end{bmatrix}. \quad (8)$$

This form of the Hamiltonian shows clearly that when $\Omega_{R0} \ll \Delta_B$, the coupling to the state $|C_2\rangle$ can be ignored. As such, the collective excitation process leads to a Rabi oscillation in an *effectively closed two-level system* consisting of $|A\rangle$ and $|C_1\rangle$. This is the LSIIB in the context of ensemble excitation, and is the key result of this paper.

While it may be rather obvious at this point, we emphasize nonetheless that we can now represent a quantum bit by this effectively closed two-level system. In the process, we have also shown how to perform an arbitrary single qubit rotation, an essential pre-requisite for quantum com-

puting. The details of how such a qubit can be used for quantum computation, quantum communication, and the realization of a quantum network is described in Ref. [7].

To be explicit, let us consider a specific numerical example. Choosing the natural decay rate, Γ , of the excited state

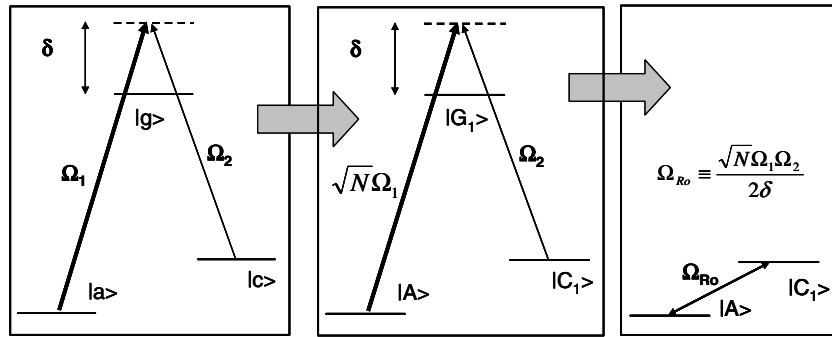


Fig. 5. Summary of the LSIIB process in an ensemble.

to be unity, assume $\Omega_2 = 100$, $\Omega_1 = \eta \ll 1$, and $\delta = 1000$. This corresponds to a value of $\Delta = \delta_1 - \delta_2 = \varepsilon_{C_1} - \varepsilon_A \cong 2.5$, satisfying the condition that $\delta \gg \Delta$. The value of the blockade shift is $\Delta_B \cong -1/80$. To be concrete, we satisfy the requirement that $\Omega_{Ro}/\sqrt{2} \ll \Delta_B$ by demanding that $(\Omega_{Ro}/\sqrt{2}) = \Delta_B/10$. This translates to the condition that $\eta\sqrt{N} = 0.035$. Note that these parameters satisfy the constraint that $\delta \gg \Omega_2$, and $\delta \gg \Omega_1\sqrt{N}$. The acceptable range for N will be dictated by the choice of η , or vice-versa, depending on the particular experiment at hand. As an example, for $\eta = 10^{-3}$, we need $N \cong 1200$. To see whether such a range of parameters are potentially realistic, let us consider an ensemble of cold ^{87}Rb atoms caught in a FORT trap, excited by control beams with a cross-sectional diameter of about $200 \mu\text{m}$. Assuming that the transitions employ dipole matrix element amplitudes that are half as strong as those of the strongest transitions, the power needed for the Ω_2 beam is about 100 mW , and that for the Ω_1 beam is about 10 pW . The time for a π -transition going from $|A\rangle$ to $|C_1\rangle$ is about $50 \mu\text{s}$. Given that the decoherence time in a FORT can be of the order of minutes, as many as 10^6 qubit operations can be carried out at this rate. The number of photons in the Ω_1 is close to 2000, so that its treatment as a classical beam is valid.

The essence of the LSIIB for ensemble excitation is summarized in Fig. 5. Briefly, whenever we have a three-level optically off-resonant transition for the individual atoms, this can be translated into a corresponding off-resonant three-level transition involving collective states, which in turn is reduced to an effective two-level transition. In order for this to hold, the primary constraint is that, for the collective states, the Rabi frequency on one leg must be much bigger than the same for the other.

To summarize, we have described a new type of blockade that allows one to treat an ensemble excitation as a sin-

gle, deterministic quantum bit consisting of only two-levels. Such a system can be used to realize a two-qubit gate (e.g., a C-NOT gate) between two ensemble-based qubits. It can also be used to transport, deterministically, the quantum state of an ensemble qubit from one location to another separated by macroscopic distances, and it can be used to establish a quantum-link between two ensembles-and-cavity based quantum computers.

References

- [1] R.H. Dicke, Phys. Rev. 93 (1954) 99.
- [2] L.M. Duan, M.D. Lukin, J.I. Cirac, P. Zoller, Nature 414 (2001) 413.
- [3] L.M. Duan, J.I. Cirac, P. Zoller, Phys. Rev. A 66 (2002) 023818.
- [4] G.K. Brennen, I.H. Deutsch, P.S. Jessen, Phys. Rev. A 61 (2000) 062309.
- [5] M.D. Lukin, M. Fleischhauer, R. Cote, L.M. Duan, D. Jaksch, J.I. Cirac, P. Zoller, Phys. Rev. Lett. 87 (2001) 037901.
- [6] T. Pellizzari, S.A. Gardiner, J.I. Cirac, P. Zoller, Phys. Rev. Lett. 75 (1995) 3788.
- [7] M.S. Shahriar, G.S. Pati, K. Salit, Phys. Rev. A, submitted for publication, preprint. <<http://arxiv.org/abs/quant-ph/0604121>>.
- [8] S. Lloyd, M.S. Shahriar, J.H. Shapiro, P.R. Hemmer, Phys. Rev. Lett. 87 (2001) 167903.
- [9] M.S. Shahriar, J. Bowers, S. Lloyd, P.R. Hemmer, P.S. Bhatia, Opt. Commun. 195 (2001) 5.
- [10] S. Lloyd, J. Shapiro, F. Wong, P. Kumar, M.S. Shahriar, H. Yuen, ACM SIGCOMM Computer Communication Review, October 2004.
- [11] P. Meystre, M. Sargent III, Elements of Quantum Optics, Springer-Verlag, Berlin, 1990 (Chapter 3).
- [12] M.S. Shahriar, P.R. Hemmer, M.G. Prentiss, P. Marte, J. Mervis, D.P. Katz, N.P. Bigelow, T. Cai, Phys. Rev. A (Rapid Commun.) 48 (1993) R4034.
- [13] M.S. Shahriar, P. Hemmer, D.P. Katz, A. Lee, M. Prentiss, Phys. Rev. A. 55 (1997) 2272.
- [14] P. Hemmer, M. Prentiss, M.S. Shahriar, P. Hemmer, Opt. Commun. 89 (1992) 335.
- [15] M.S. Shahriar, P. Hemmer, Phys. Rev. Lett. 65 (1990) 1865.

Quantum communication and computing with atomic ensembles using a light-shift-imbalance-induced blockade

M. S. Shahriar, G. S. Pati, and K. Salit

EECS Department, Northwestern University, Evanston, Illinois 60208, USA

(Received 2 September 2006; revised manuscript received 13 December 2006; published 21 February 2007)

Recently, we have shown that for conditions under which the so-called light-shift imbalance induced blockade occurs, the collective excitation of an ensemble of a multilevel atom can be treated as a closed two-level system. In this paper, we describe how such a system can be used as a quantum bit (qubit) for quantum communication and quantum computing. Specifically, we show how to realize a controlled-NOT gate using the collective qubit and an easily accessible ring cavity, via an extension of the so-called Pellizzari scheme. We also describe how multiple, small-scale quantum computers realized using these qubits can be linked effectively for implementing a quantum internet. We describe the details of the energy levels and transitions in an ^{87}Rb atom that could be used for implementing these schemes.

DOI: [10.1103/PhysRevA.75.022323](https://doi.org/10.1103/PhysRevA.75.022323)

PACS number(s): 03.67.Lx, 03.67.Hk, 32.80.Qk, 42.50.Ct

I. INTRODUCTION

When an atomic ensemble is excited, by a laser beam matched to a two-level transition (or a Raman transition), for example, it leads to a cascade of many states as more and more photons are absorbed [1–3]. In order to make use of an ensemble as a quantum bit (qubit), it is necessary to disrupt this cascade, and restrict the excitation to the absorption (and emission) of a single photon only. In principle, this can be achieved through the use of the so-called dipole blockade [4,5]. In order to make use of this blockade mechanism in a manner that is consistent with a quantum computing architecture, it is necessary to control the distribution of interatomic distances between each pair of atoms in the ensemble in a precise manner. Furthermore, in order to achieve long decoherence times, it is necessary to make use of dipole blockade based on spin-spin coupling, which is necessarily much weaker than the optical dipole-dipole coupling. Recently, we have shown that a different type of blockade mechanism, based on the light-shift imbalance in a Raman transition, can overcome these constraints. The resulting system does not impose any constraint on the distribution of interatomic distance within an ensemble. Furthermore, no dipole-dipole coupling is necessary, so that a relatively low density system can be used.

In Ref. [6], we have shown how this light-shift-imbalance-induced blockade (LSIIB) process enables one to treat the ensemble as a two-level atom that undergoes fully deterministic Rabi oscillations between two collective quantum states, while suppressing excitations of higher-order collective states. In this paper, we show how this transition can be used to realize a qubit embodied by the ensemble. Using multiple energy levels inside each atom, we show how the LSIIB enables the transfer of quantum information between neighboring ensembles, as well as the realization of a controlled-NOT gate. In effect, this represents a generalization of the so-called Pellizzari scheme for quantum information processing [7]. Furthermore, we show that the LSIIB can be used to link two separate quantum computers (QCs), by transferring the quantum state of any ensemble qubit in one QC to any ensemble qubit in another QC. We discuss

practical ways to implement this scheme using specific energy levels and transitions in ^{87}Rb atoms, and propose experiments to demonstrate the feasibility of these protocols.

The significance of the light-shift-imbalance-induced blockade (LSIIB) process can be summarized as follows: (i) It can be used to realize a deterministic quantum bit encoded in the collective-excitation states of an atomic ensemble. (ii) Along with an easily accessible ring cavity, it can be used to realize a two-qubit gate (e.g., a controlled-NOT gate) between two ensemble-based qubits. (iii) It can be used to transport, deterministically, the quantum state of an ensemble qubit from one location to another separated by macroscopic distances. (iv) It can be used to establish a quantum link between two ensembles-and-cavity based quantum computers. The scheme proposed here thus offers a robust technique for realizing a quantum internet without using the single-atom and ultrashort cavity based approaches [8–10].

II. FUNDAMENTALS OF THE LSIIB PROCESS

We summarize first the basic notations for describing the LSIIB process [6]. In the simplest version, we consider each atom in the ensemble to be a Λ -type three-level system, with two metastable states ($|a\rangle$ and $|c\rangle$), and an optically excited state ($|e\rangle$), as shown in Fig. 1. The collective states of interest are defined as follows [6]:

$$|A\rangle \equiv |a_1, a_2, \dots, a_N\rangle,$$

$$|G_1\rangle \equiv \frac{1}{\sqrt{N}} \sum_{j=1}^N |a_1, a_2, \dots, g_j, \dots, a_N\rangle,$$

$$|C_1\rangle \equiv \frac{1}{\sqrt{N}} \sum_{j=1}^N |a_1, a_2, \dots, c_j, \dots, a_N\rangle,$$

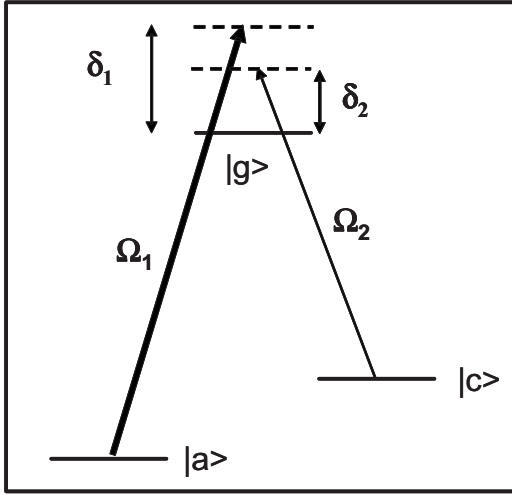


FIG. 1. Schematic illustration of a three-level transition in each atom in an ensemble.

$$|G_2\rangle \equiv \frac{1}{\sqrt{{}^N C_{2,j,k(j \neq k)}}} \sum |a_1, a_2, \dots, g_j, \dots, g_k, \dots, a_N\rangle,$$

$$|C_2\rangle \equiv \frac{1}{\sqrt{{}^N C_{2,j,k(j \neq k)}}} \sum |a_1, a_2, \dots, c_j, \dots, c_k, \dots, a_N\rangle,$$

$$|G_{1,1}\rangle \equiv \frac{1}{\sqrt{2^N C_{2,j,k(j \neq k)}}} \sum |a_1, a_2, \dots, g_j, \dots, c_k, \dots, a_N\rangle,$$

$$|G_{2,1}\rangle \equiv \frac{1}{\sqrt{Z}} \sum_{(j \neq k \neq l)}^Z |a_1, a_2, \dots, g_j, \dots, g_k, \dots, c_l, \dots, a_N\rangle,$$

$$|G_{1,2}\rangle \equiv \frac{1}{\sqrt{Z}} \sum_{(j \neq k \neq l)}^Z |a_1, a_2, \dots, g_j, \dots, c_k, \dots, c_l, \dots, a_N\rangle,$$

$$[Z = 3^N C_3], \quad (1)$$

where ${}^N C_M \equiv \binom{N}{M} \equiv N!/[M!(N-M)!]$. The relevant coupling rates between these collective states are also illustrated in Fig. 2. Note that for large detunings, the excitations to the intermediate states $|G_1\rangle$ and $|G_{1,1}\rangle$ are small, so that higher-order states such as $|G_2\rangle$ and $|G_{2,1}\rangle$ can be ignored. (Parenthetically at this point, note that the coupling between $|G_1\rangle$ and $|C_1\rangle$ does not scale with \sqrt{N} , unlike the coupling between $|A\rangle$ and $|G_1\rangle$, which scales as \sqrt{N} .)

In the rotating wave transformation frame, the truncated, six-level Hamiltonian, in the bases of $|A\rangle$, $|G_1\rangle$, $|C_1\rangle$, $|G_{1,1}\rangle$, $|C_2\rangle$, and $|G_{1,2}\rangle$ is given by (the justification for not including the state $|C_3\rangle$ will be made by showing that the excitation to $|C_2\rangle$ can be suppressed, thus in turn making the amplitude of $|C_3\rangle$ insignificant)

$$H = \begin{bmatrix} \Delta/2 & \sqrt{N}\Omega_1/2 & 0 & 0 & 0 & 0 \\ \sqrt{N}\Omega_1/2 & -\delta & \Omega_2/2 & 0 & 0 & 0 \\ 0 & \Omega_2/2 & -\Delta/2 & (\sqrt{N-1})\Omega_1/2 & 0 & 0 \\ 0 & 0 & (\sqrt{N-1})\Omega_1/2 & -(\delta+\Delta) & \sqrt{2}\Omega_2/2 & 0 \\ 0 & 0 & 0 & \sqrt{2}\Omega_2/2 & -3\Delta/2 & (\sqrt{N-2})\Omega_1/2 \\ 0 & 0 & 0 & 0 & (\sqrt{N-2})\Omega_1/2 & -(\delta+2\Delta) \end{bmatrix}, \quad (2a)$$

where the detunings are defined as $\delta \equiv (\delta_1 + \delta_2)/2$ and $\Delta \equiv (\delta_1 - \delta_2)$.

If the detunings are large compared to the transition rates, we can eliminate states $|G_1\rangle$, $|G_{1,1}\rangle$ and $|G_{1,2}\rangle$ adiabatically. Under this condition, the effective Hamiltonian for the three remaining states ($|A\rangle$, $|C_1\rangle$, and $|C_2\rangle$) are given by (assuming $\delta \gg \Delta$)

$$\tilde{H} = \begin{bmatrix} \varepsilon_A + \Delta/2 & \Omega_{Ro}/2 & 0 \\ \Omega_{Ro}/2 & \varepsilon_{C1} - \Delta/2 & \sqrt{[2(N-1)/N]}\Omega_{Ro}/2 \\ 0 & \sqrt{[2(N-1)/N]}\Omega_{Ro}/2 & \varepsilon_{C2} - 3\Delta/2 \end{bmatrix}, \quad (2b)$$

where ε_A , ε_{C1} , and ε_{C2} are the light shifts of the states $|A\rangle$, $|C_1\rangle$, and $|C_2\rangle$, respectively, and $\Omega_{Ro} \equiv (\sqrt{N}\Omega_1\Omega_2)/(2\delta)$. To

first order, these light shifts are given by $\varepsilon_A = N\Omega_1^2/4\delta$, $\varepsilon_{C1} = [\Omega_2^2 + (N-1)\Omega_1^2]/4\delta$, and $\varepsilon_{C2} = [2\Omega_2^2 + (N-2)\Omega_1^2]/4\delta$, and are balanced, in the sense that $(\varepsilon_{C1} - \varepsilon_A) = (\varepsilon_{C2} - \varepsilon_{C1})$. This means that if the explicit two-photon detuning Δ is chosen to make the Raman transition between $|A\rangle$ and $|C_1\rangle$ resonant [i.e., $\Delta = (\varepsilon_{C1} - \varepsilon_A)$], then the Raman transition between $|C_1\rangle$ and $|C_2\rangle$ also becomes resonant. This balance is broken when the light shifts are calculated to second order, and the blockade shift is then given by

$$\Delta_B \equiv (\varepsilon_{C2} - \varepsilon_{C1}) - (\varepsilon_{C1} - \varepsilon_A) = -(\Omega_2^4 + \Omega_1^4)/(8\delta^3). \quad (3)$$

With the proper choice of two-photon detuning [$\Delta = (\varepsilon_{C1} - \varepsilon_A)$] to make the Raman transition between $|A\rangle$ and $|C_1\rangle$

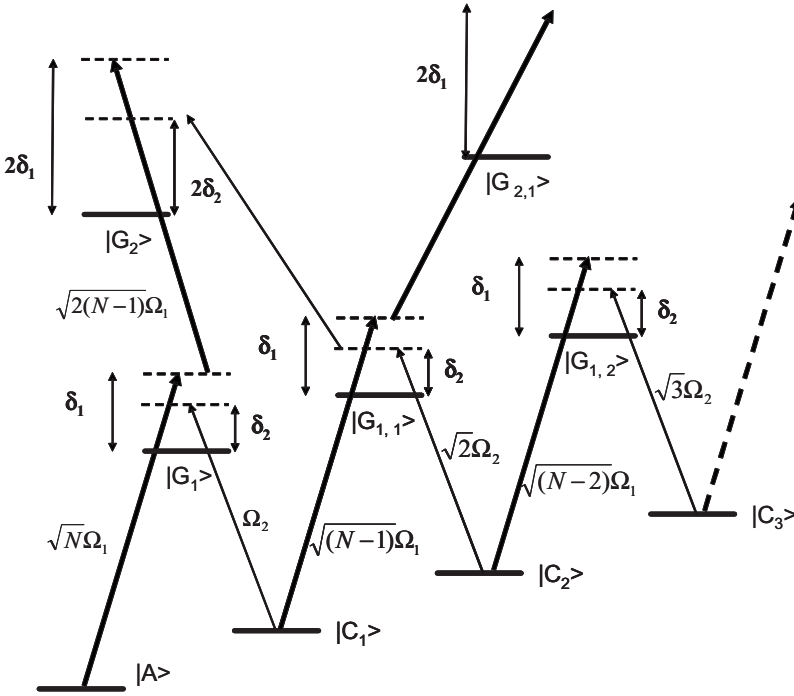


FIG. 2. Schematic illustration of the relevant collective states and the corresponding transition rates. See text for details.

resonant, the effective Hamiltonian (after shifting the zero of energy, and assuming $N \gg 1$) is now given by

$$\tilde{H} = \begin{bmatrix} 0 & \Omega_{Ro}/2 & 0 \\ \Omega_{Ro}/2 & 0 & \Omega_{Ro}/\sqrt{2} \\ 0 & \Omega_{Ro}/\sqrt{2} & \Delta_B \end{bmatrix}. \quad (4)$$

This form of the Hamiltonian shows clearly that when $[\Omega_{Ro}/\sqrt{2}] \ll \Delta_B$, the coupling to the state $|C_2\rangle$ can be ignored. As such, the collective excitation process leads to a Rabi oscillation in an *effectively closed two-level system* consisting of $|A\rangle$ and $|C_1\rangle$. This is the LSIIB in the context of ensemble excitation, and is the key result upon which most of the protocols we propose here are based.

Thus we can now represent a quantum bit by this effectively closed two-level system. In the process, we have also shown how to perform an arbitrary single qubit rotation, an essential prerequisite for quantum computing. The essence of the LSIIB for ensemble excitation can be summarized as follows. Whenever we have a three-level optically off-resonant transition for the individual atoms, this can be translated into a corresponding off-resonant three-level transition involving collective states, which in turn is reduced to an effective two-level transition, as illustrated in Fig. 3. In order for this to hold, the primary constraint is that, for the collective states, the Rabi frequency on one leg must be much bigger than the same for the other.

At this point, it is instructive to consider a specific numerical example. Choosing the natural decay rate Γ of the excited state to be unity, assume $\Omega_2=100$, $\Omega_1=\eta \ll 1$, and $\delta=1000$. This corresponds to a value of $\Delta=\delta_1-\delta_2=\epsilon_{C1}-\epsilon_A \cong 2.5$, satisfying the condition that $\delta \gg \Delta$. The value of the blockade shift is $\Delta_B \cong -1/80$. To be concrete, we satisfy the requirement that $\Omega_{Ro}/\sqrt{2} \ll \Delta_B$ by demanding that $(\Omega_{Ro}/\sqrt{2}) = \Delta_B/10$. This translates to the condition that $\eta/\sqrt{N}=0.035$.

Note that these parameters satisfy the constraint that $\delta \gg \Omega_2$, and $\delta \gg \Omega_1/\sqrt{N}$. The acceptable range for N will be dictated by the choice of η , or vice versa, depending on the particular experiment at hand. As an example, for $\eta=10^{-3}$, we need $N \cong 1200$. To see whether such a range of parameters is potentially realistic, let us consider an ensemble of cold ^{87}Rb atoms caught in a far off-resonant trap (FORT) trap, excited by control beams with a cross-sectional diameter of about $200 \mu\text{m}$. Assuming that the transitions employed dipole matrix element amplitudes that are half as strong as those of the strongest transitions, the power needed for the Ω_2 beam is about 100 mW, and that for the Ω_1 beam is about 10 pW. The time for a π transition going from $|A\rangle$ to $|C_1\rangle$ is about $50 \mu\text{s}$. Given that the decoherence time in a FORT can be of the order of minutes, as many as 10^6 qubit operations can be carried out at this rate. The number of photons in the Ω_1 is close to 2000, so that its treatment as a classical beam is valid.

III. REALIZATION OF A CONTROLLED-NOT GATE BETWEEN TWO ENSEMBLES

The LSIIB process can be used to perform two qubit operations between two ensembles. In particular, we show here

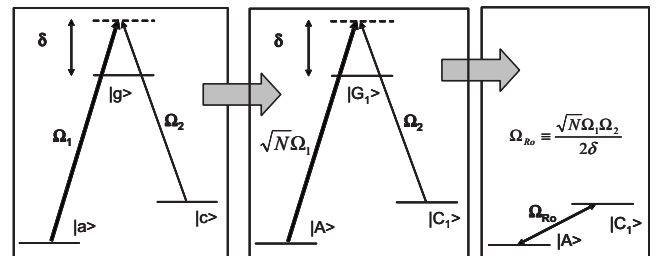


FIG. 3. Summary of the LSIIB process in an ensemble. See text for details.

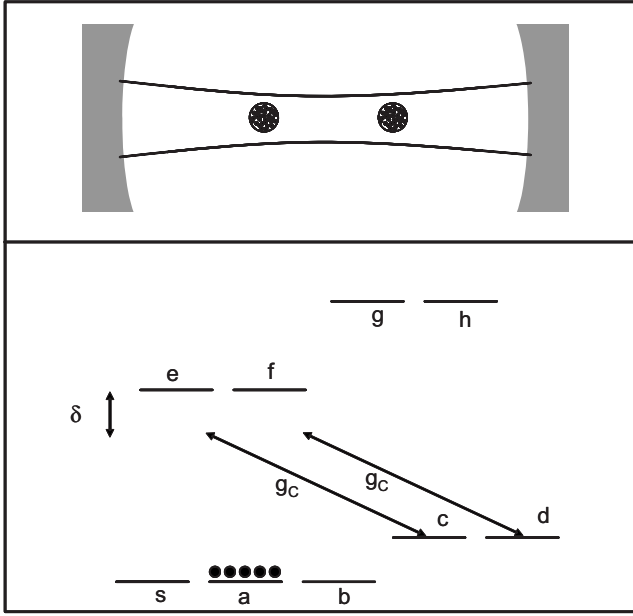


FIG. 4. Illustration of the basic configuration for coupling two ensembles (top), and the requisite energy levels for each atom (bottom). See text for details.

how a controlled-NOT gate can be realized in such a system. The process we describe is essentially the ensemble version of the well-known Pellizzari scheme [7]. Figure 4 (top) shows the basic configuration involving only two ensembles and a cavity. A more general scheme that can couple the nearest-neighbor ensembles in a large array of ensembles is described schematically later on. In what follows, the two ensembles will be denoted as ensembles I and II, respectively. Figure 4 (bottom) shows the necessary energy levels in each of the atoms. The transition corresponding to the cavity mode is also illustrated, with a vacuum Rabi frequency of g_c . Later on, we will discuss how an alkali-metal atom such as ^{87}Rb may be used to implement these energy levels.

We assume that both ensembles are prepared in the $|A\rangle$ state. For the other states, the only ones that will be relevant are the ones that are of the following form:

$$|Q_1\rangle \equiv \frac{1}{\sqrt{N}} \sum_{j=1}^N |a_1, a_2, \dots, q_j, \dots, a_N\rangle, \quad (5)$$

$q = s, b, c, d, e, f, g \text{ or } h \text{ (excluding } a).$

We now describe the controlled-NOT gate operation in multiple steps.

Step 1: Initialize each ensemble in an arbitrary quantum superposition. At $t=0$, we assume that each ensemble is in state $|A\rangle$: $|\psi\rangle_I = |A\rangle_I$; $|\psi\rangle_{II} = |A\rangle_{II}$. This can be achieved, in principle, by optical pumping in a real system. *Operations for ensemble I:* The transitions to be used for performing the single qubit rotation is shown in Fig. 5. With $\Omega_2 \ll \Omega_1$, we apply these two pulses simultaneously for duration T_1 . The state of ensemble I (E-I) is then given by $|\psi\rangle_I = \cos[\Omega_{Ro}T_1/2]|A\rangle_I + i\sin[\Omega_{Ro}T_1/2]|C_1\rangle_I \equiv \alpha|A\rangle_I + \beta|C_1\rangle_I$.

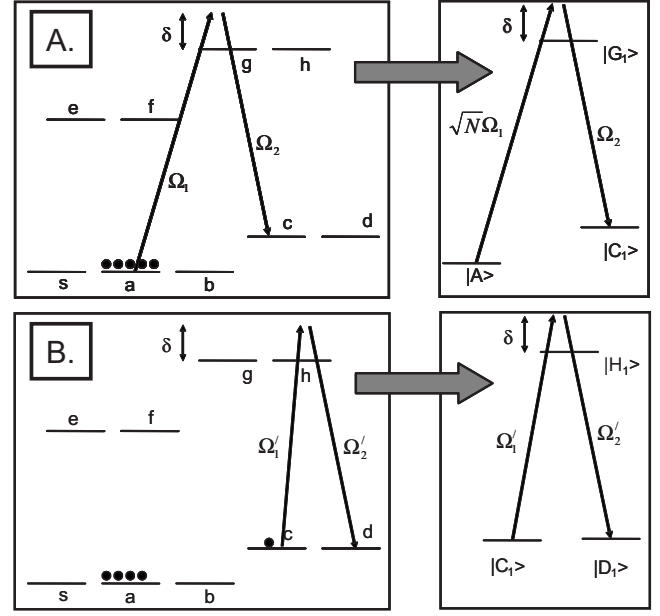


FIG. 5. (a) Schematic illustration of the single qubit state preparation in ensemble I. (b) Schematic illustration for the single qubit operation for ensemble II. See text for details.

Here, Ω_{Ro} is as defined in Eq. (2) above. This achieves the goal of producing an arbitrary quantum state in E-I. *Operations for ensemble II:* For the second ensemble, we apply the same transitions as in Fig. 5(a), but for a duration T_2 such that $\Omega_{Ro}T_2 = \pi$. This corresponds to a pi pulse, and ensemble II (E-II) is now in state $|C_1\rangle$. This is now followed by the excitation pulses shown in Fig. 5(b). Note in particular that the coupling rates for the collective states no longer include the \sqrt{N} factor. The pulses at Ω'_1 and Ω'_2 are applied for a duration T_3 (satisfying the condition that $\Omega'_2 \ll \Omega'_1$), so that the state for E-II is now given by $|\psi\rangle_{II} = \cos[\Omega'T_3/2]|C\rangle_{II} + i\sin[\Omega'T_3/2]|D\rangle_{II} \equiv \xi|C\rangle_{II} + \eta|D\rangle_{II}$. Thus we now have prepared E-II in an arbitrary qubit state. Finally, note that the cavity so far is in the ground state with no photons: $|\psi\rangle_C = |0\rangle_C$.

Step 2: Transfer state of E-I to the cavity. The transitions to be employed for this step is illustrated in Fig. 6(a). The pulse at Ω_I is applied for a duration T_4 such that $(\sqrt{N}\Omega_I g_c / 2\delta) T_4 = \pi$. As a result of this pi pulse, the states of E-II remain unchanged, but the states of E-I and the cavity become as follows: $|\psi\rangle_C = \alpha|0\rangle_C + \beta|1\rangle_C$; $|\psi\rangle_I = |C_1\rangle_I$. This accomplishes the goal of transferring the quantum state of E-I to the cavity.

Step 3: Transfer state of the cavity to E-II. The transitions used for this step, in E-II, is illustrated in Fig. 6(b). Note again that the transition rates for coupling the collective states now do not include the \sqrt{N} factor. The pulse at Ω_{II} is applied for a duration T_5 such that $(\Omega_{II} g_c / 2\delta) T_5 = \pi$. As a result of this pi pulse, the states of E-I remains unchanged, but the states of E-II and the cavity become as follows: $|\psi\rangle_C = |0\rangle_C$; $|\psi\rangle_{II} = \alpha\xi|S_1\rangle_{II} + \xi\beta|C_1\rangle_{II} + \eta\alpha|B_1\rangle_{II} + \eta\beta|D_1\rangle_{II}$. This accomplishes the goal of transferring the quantum information from the cavity to E-II. Of course, steps 2 and 3 together achieve the objective of transferring all the quantum infor-

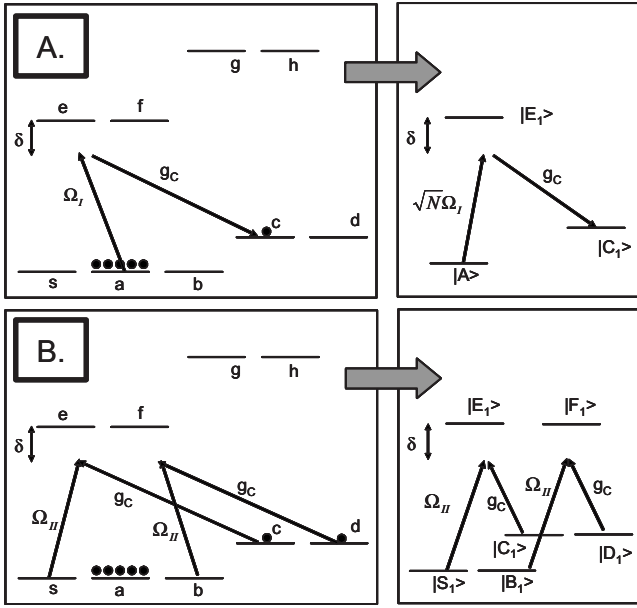


FIG. 6. (a) Illustration of the excitation step used to transfer the state of E-I to the cavity. (b) Schematic illustration of the pulses inside E-II to transform the cavity state to E-II. See text for details.

mation from both ensembles into ensemble II only.

Step 4: Perform “effective controlled-NOT transition” inside E-II. Using the transitions shown in Fig. 5(b), we apply a pi pulse to E-II, which exchanges the amplitudes of $|C_1\rangle_{II}$ and $|D_1\rangle_{II}$. As a result, while E-I and the cavity stays unchanged, the state of E-II now becomes $|\psi\rangle_{II} = \alpha\xi|S_1\rangle_{II} + \xi\beta|D_1\rangle_{II} + \eta\alpha|B_1\rangle_{II} + \eta\beta|C_1\rangle_{II}$.

Step 5: Transfer E-II quantum state partly to the cavity. Using the transitions shown in Fig. 6(b), we now apply another pi pulse in E-II. As a result, while E-I stays unchanged, the cavity and the E-II now become entangled: $|\psi\rangle_{II-C} = \alpha\xi|C_1\rangle_{II}|1\rangle_C + \xi\beta|D_1\rangle_{II}|0\rangle_C + \eta\alpha|D_1\rangle_{II}|1\rangle_C + \eta\beta|C_1\rangle_{II}|0\rangle_C$.

Step 6: Transfer cavity state back to E-I. Using the transitions shown in Fig. 3(a), we now apply another pi pulse in

E-I. As a result, the cavity returns to the zero-photon state, and E-I and E-II are now entangled: $|\psi\rangle_C = |0\rangle_C$; $|\psi\rangle_{I-II} = \alpha\xi|A\rangle_I|C_1\rangle_{II} + \eta\alpha|A\rangle_I|D_1\rangle_{II} + \beta\xi|C_1\rangle_I|D_1\rangle_{II} + \beta\eta|C_1\rangle_I|C_1\rangle_{II}$. This is to be compared with the direct-product state at the beginning of the protocol: $|\psi\rangle_{I-II}(\text{init}) = |\psi\rangle_I|\psi\rangle_{II} = \alpha\xi|A\rangle_I|C_1\rangle_{II} + \alpha\eta|A\rangle_I|D_1\rangle_{II} + \beta\xi|C_1\rangle_I|C_1\rangle_{II} + \beta\eta|C_1\rangle_I|D_1\rangle_{II}$. Thus the quantum state of E-II has been flipped only for the case where the quantum state of E-I is in $|C_1\rangle$, which, of course, corresponds to the controlled-NOT operation.

IV. QUANTUM COMMUNICATION BETWEEN LSIIB-BASED QUANTUM COMPUTERS

The whole operation for realizing interprocessor communication is illustrated in Fig. 7. Briefly, each QC is modeled as an array of ensembles that can be moved linearly, using several different possibilities, including quantum motors or sliding standing waves through a cavity [11–15]. It is also possible to consider an implementation where race-track-shaped microcavities are used on alternating sides, with the atom seeing the cavity mode through evanescent modes. Note also that while we are concentrating primarily on ensembles of neutral atoms here, there are solid material and systems that display the kind of narrow Raman transitions necessary for implementing such a scheme [16–18], although we have not yet worked out the details for an explicit solid-state system.

The objective of the communication link is to transfer the quantum state of the ensemble (Q1) on the edge of one QC (QC1) to the ensemble (Q2) on the edge of the other QC (QC2). To start with, assume that Q1 is in an arbitrary quantum state (the protocol would work just as well in the more useful case when this atom is entangled with the rest of QC1), and Q2 is in its ground state: $|\psi\rangle_{Q1} = \alpha|A\rangle_{Q1} + \beta|C_1\rangle_{Q1}$; $|\psi\rangle_{Q2} = |A\rangle_{Q2}$. The transitions to be used for the transfer process are illustrated in the bottom of Fig. 7. Note that here we are using the same set of transition as in Fig. 5(a), except that instead of using a semiclassical mode to

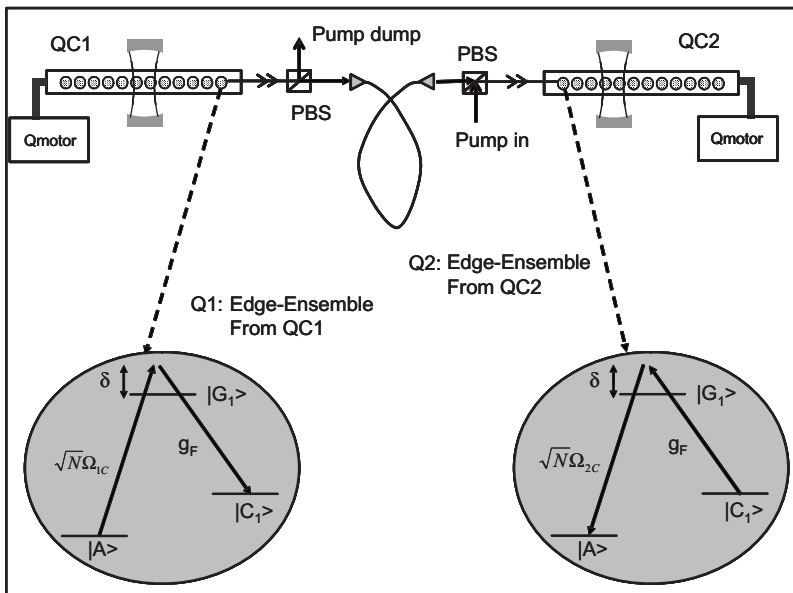


FIG. 7. Schematic illustration of quantum communication between two quantum computer. See text for details.

couple the $|g\rangle$ to $|c\rangle$ transition, we use a free-space single-photon mode. The parameters of this mode (such as the vacuum Rabi frequency g_F) is determined essentially by the pump pulse [3,18]. We now apply a pulse for a duration τ_R such that $(\sqrt{N}\Omega_{1c}g_F/2\delta)\tau_R=\pi$. The result would be a transfer of the quantum state of Q1 to the free-space photon mode (in essentially the same way as in step 2 of the controlled-NOT protocol). A fiber delay line will allow one to let this photon state leave QC1 completely. The pump pulse on Q2 will be timed with the anticipated arrival of this photon state (this can be done, since the delay between the photon state and the pump in Q1 can be precalibrated as well as calculated). This pump will then be applied for a duration τ_W such that $(\sqrt{N}\Omega_{2c}g_F/2\delta)\tau_W=\pi$. Note that the presence of the \sqrt{N} factor makes both of these processes fast enough even for a free-space photon mode. After the second pulse, the free-space photon mode will be in the zero photon state, and the quantum states of Q1 and Q2 would be $|\psi\rangle_{Q2}\equiv\alpha|A\rangle_{Q2}+\beta|C_1\rangle_{Q2}$; $|\psi\rangle_{Q1}=|A\rangle_{Q1}$. It is obvious that if Q1 were entangled with the rest of QC1, then Q2 will now be entangled with the rest of QC1. This is, of course, all that is needed to link the two quantum computers.

V. EXPERIMENTAL CONSTRAINTS ON CAVITY AND ENSEMBLE PARAMETERS

In order to see the feasibility of these operations, it is important to consider the relevant cavity parameters. When the ensemble qubit is interacting with the cavity mode (e.g., in step 2 above), the vacuum coupling rate is enhanced by a factor of \sqrt{N} , so that the cavity parameters for reaching the strong-coupling regime is significantly relaxed. To illustrate, consider the situation where a cavity holds an ensemble rubidium qubit of N atoms, with a length of L , and an effective mode diameter of d at the center. The single-photon electric-field amplitude is then given by $\sqrt{(2\hbar\omega)/(\epsilon_0V)}$ where $V\approx(\pi/4)d^2L$ is the effective mode volume [19], and ω is the frequency of the photon. For the rubidium atom, with $N=1$, the corresponding vacuum rabi frequency is proportional to this field amplitude, given by $g_o\approx 54.25\Gamma$ (where $\Gamma\approx 2\pi 6\times 10^6\text{ s}^{-1}$ is the natural linewidth) for $L_o=40\text{ }\mu\text{m}$ and $d_o=5\text{ }\mu\text{m}$ [20]. If we assume a matched pair of essentially lossless mirrors, each with an intensity transmittivity of 1.2×10^{-6} , the corresponding cavity finesse is about 2.6×10^6 , with a free spectral range (FSR) of about $3.8\times 10^{12}\text{ Hz}$ [21]. This yields a cavity decay rate, γ_o (half width at half maximum), of about 0.12Γ , so that the cavity lifetime, $\tau_o\equiv\gamma_o^{-1}$, is about 222 ns. From the discussion above, it is easy to see that these parameters scale as follows: $g=g_o(d_o/d)\times(L_o/L)^{1/2}N^{1/2}$, and $\tau=\tau_o(T_o/T)(L/L_o)$.

Consider next a situation where the number of atoms in the collective qubit is 3000. Using the scaling laws stated above, we see that the vacuum rabi frequency will remain unchanged if the length is increased by a factor of 3000 ($L=12\text{ cm}$). Here, we consider a cavity length of $L=5\text{ cm}$, so that the vacuum rabi frequency is $g_o\approx 84.04\Gamma$, and the FSR is $3.0\times 10^9\text{ Hz}$. For the same finesse as above, the cavity decay rate is now only $9.55\times 10^{-5}\Gamma$, with the corresponding cavity lifetime being close to 0.3 ms. With expected im-

provements in the mirror qualities, the cavity storage time may possibly become even longer. If we choose the strength of Ω_1 to be $7\times 10^{-4}\Gamma$, with a common-mode detuning of $\delta=10^3\Gamma$, the constraints for the LSIIB are easily satisfied. The time needed for a π pulse is about $50\text{ }\mu\text{s}$, which is considerably shorter than the cavity lifetime. In this context, we point out that a variant of the Pellizari scheme [7]—which makes use of the so-called Cavity Dark State [18]—can also be used to implement a controlled-NOT gate. When this approach is used, the cavity remains virtually unpopulated during the operation, thereby reducing the constraint on the cavity lifetime. Another important consequence of such a long cavity is that it allows one to use a ring-configuration rather than a conventional Fabry-Perot configuration, thereby avoiding the formation of standing waves in the cavity. The long cavity also makes it potentially easier to access the ensemble with the external control beams.

VI. PROPOSED EXPERIMENTS USING RUBIDIUM ATOMIC ENSEMBLES

The energy levels and selection rules necessary for implementing these schemes can be accommodated by using, for example, Zeeman sublevels in the D1 transition manifold in ^{87}Rb atoms. One explicit construct is shown in Fig. 8. A nonzero magnetic field is used to lift the degeneracy between the state $|a\rangle$ and states $\{|s\rangle$ and $|b\rangle\}$. This is necessary in order to ensure, for example, that during the process outlined in Fig. 5(a), there is no Raman coupling between $|s\rangle$ and $|c\rangle$ (or between $|b\rangle$ and $|d\rangle$). Similar constraints also apply for processes illustrated in Fig. 6(a). For the process in Fig. 6(b), the opposite constraint applies (that is, $|s\rangle$ to $|c\rangle$ as well as $|b\rangle$ to $|d\rangle$ are allowed, but $|a\rangle$ is not coupled due to Raman detuning). The amount of magnetic field to be applied can be rather small, (typically less than a gauss), with the constraint that the Zeeman shift should be larger than the Raman transition linewidths. The second-order Zeeman shift for the $|a\rangle$ state would be very small in this case, and can be taken into account in choosing the relevant Raman resonance conditions.

Note that the g factors for the $F=1$ and $F=2$ levels are equal and opposite, which ensures that the s - c transition and the b - d transitions can be simultaneously Raman resonant. Note also that the g factors for the $F'=1$ and $F'=2$ are also equal and opposite to each other, and are a factor of a 3 smaller than those for the $F=1$ and $F=2$ levels. More importantly, because the Raman transitions are far detuned from the F' sublevels optically, the Zeeman shifts of the sublevels for $F'=1$ and $F'=2$ are of virtually no significance.

The energy difference between the $F'=1$ and $F'=2$ is more than 816 MHz. Thus for processes that are detuned below resonance with respect to the $F'=1$ [e.g., for the process in Fig. 6(b)] sublevel will not be influenced significantly by the $F'=2$ level. By the same token, for processes that are detuned above resonance with respect to the $F'=2$ [e.g., for the process in Fig. 5(a)] sublevel will not be influenced significantly by the $F'=1$ level. This consideration was taken into account in designing the protocols, so that for some operations the detuning is negative [e.g., Fig. 2(a)], while for

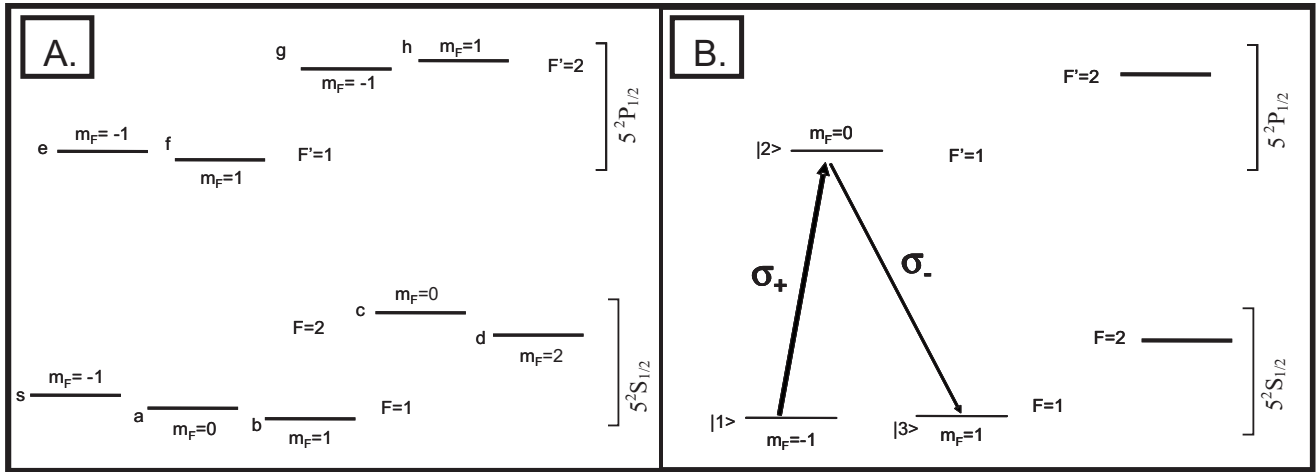


FIG. 8. (a) Schematic illustration of the Zeeman sublevels in the D1 manifold of ^{87}Rb atoms that can be used to implement the proposed schemes. (b) Schematic illustration of the ^{87}Rb transitions that can be used for demonstrating the LSIIB effect in a single cluster without a surrounding cavity. See text for details.

others the detuning is positive [e.g., Fig. 3(b)].

Finally, note that in order to allow for the selection rules assumed in the protocols, it is necessary to use a combination of σ_+ , σ_- , and π polarized light. This can be easily accommodated, since two orthogonal directions are free for applying classical field even in the presence of a cavity.

Using a configuration where a cluster of atoms are trapped using a FORT beam it should be possible to demonstrate the ensemble-based LSIIB process, without using a cavity. Note that, for an ensemble, this process occurs in a pure Λ system. This can be realized by using the states $|1\rangle$, $|2\rangle$, and $|3\rangle$ of Fig. 8(b). The atoms will first be optically pumped into state $|1\rangle$. The two-opposite circularly polarized beams, detuned from the $F'=1$ level, will then be used to excite the Raman transition between $|1\rangle$, $|2\rangle$, and $|3\rangle$. Since the off-resonant excitation produces negligible population in $|2\rangle$, no repump beam would be necessary.

The evidence of LSIIB in this case, of course, is not as simple as in the case of single atoms [6]. What is necessary in this case is to demonstrate that one and only one atom (on average) can be excited to level $|3\rangle$. In order to test this, one can operate the Raman transition process in a pulsed mode, with a variable pulse duration. After applying a Raman pulse, the beams exciting the 1-2-3 transition would be turned off, and another Raman transition would be applied to transfer the atom(s) in state $|1\rangle$ to the $F=2$, $m_F=2$ level. A cycling transition that couples this state to the $F=3$, $m_F=3$ level in the D2 manifold would then be used to collect fluorescence produced from this atom. The fluorescence could be collected by a high numerical aperture imaging system, and then transported through a fiber to a single-photon counter. By taking into account all the experimental parameters, one should thus be able to determine the number of atoms that were excited to state $|3\rangle$. The proof of ensemble-LSIIB would be established by showing that this never exceeds 1 for any pump-pulse duration.

The specific geometry of the experimental setup that could be used to demonstrate the ensemble-LSIIB based controlled-NOT gate is illustrated schematically in Fig. 9(a).

The FORT beams shown could be produced from a single beam with imaging optics. Using dichroic mirrors, additional beams (to be used for producing the control pulses for each ensemble) could be brought in, parallel to the FORT beams. Additional control beams would be brought in a direction perpendicular to both the cavity axis and the FORT axis. This degree of freedom would enable us to satisfy the polarization selection rules.

In order to keep the process as clean as possible, it is advisable to consider first the simplest nontrivial version of the controlled-NOT gate. Recall the most general form of the input (unentangled) state of the two ensembles, and the corresponding entangled state after the controlled-NOT operation, one could choose the parameters such that $\alpha=\beta=1/\sqrt{2}$, $\xi=1$, and $\eta=0$. The entangled state produced by the controlled-NOT gate would therefore be given by $|\psi\rangle_{I-II} = [|A\rangle_I |C_1\rangle_{II} + |C_1\rangle_I |D_1\rangle_{II}] / \sqrt{2}$. Here, Ens-I is the ensemble trapped by FORT1, and Ens-II is the one trapped by FORT2, for example.

In order to demonstrate that such a state has indeed been produced, one can proceed in several different ways. One option is to apply the pulse described in Fig. 7, with the pump beam parallel to the direction of FORT1 (which holds Ens-I). If Ens-I is in state $|A\rangle$, then application of a pulse so that $(\sqrt{N}\Omega_{1C}g_F/2\delta)\tau_R = \pi$ will produce a single photon in the free-space mode (characterized by the single-photon Rabi frequency of g_F). As described in detail previously, the field at Ω_{1C} is coupled to the $|a\rangle\text{-}|g\rangle$ transition with a large positive detuning, and the field for g_F is coupled to the $|c\rangle\text{-}|g\rangle$ transition with the same detuning. The frequency of the free-space mode is selected automatically in order to satisfy the two-photon transition condition. If Ens-I is in state $|C_1\rangle$, then application of the same pulse will not produce a photon in this free-space mode. The photon in this mode could be detected by using an additional fiber-coupled single-photon detector, preceded by polarization and spectral filters.

In parallel to this process, a pump beam (with Rabi-frequency Ω'_{2c}) would be applied along FORT2 (which

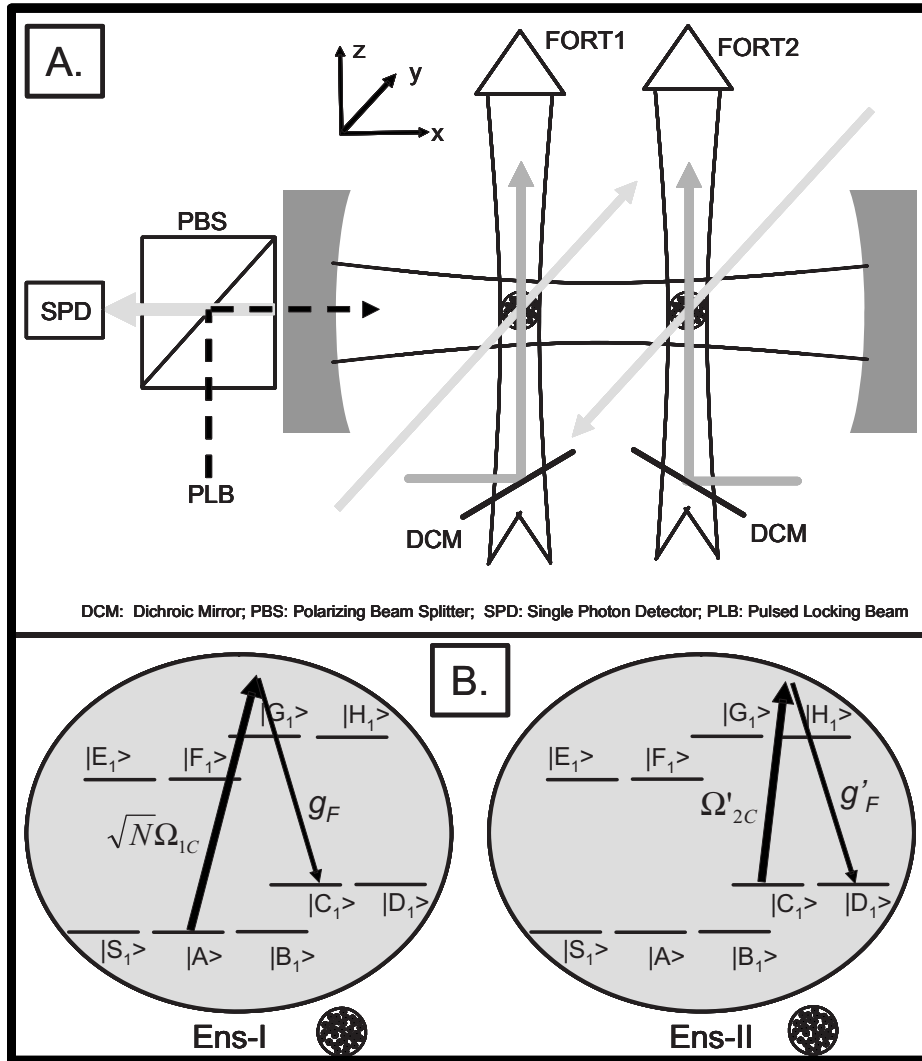


FIG. 9. (a) Schematic illustration of the configuration that can be employed for testing the controlled-NOT operation using the ensemble LSIIB. (b) Illustration of the excitations that could be employed for confirming the controlled-NOT gate operation. See text for details.

houses Ens-II), coupled to the $|c\rangle\text{-}|h\rangle$ transition, with a large, positive detuning. The corresponding free-space mode (with vacuum Rabi frequency of g'_F), coupled to the $|d\rangle\text{-}|h\rangle$ transition, would be automatically chosen to have the same detuning, in order to satisfy the two-photon resonance condition. This photon would be passed through the same set of three filters, and then detected by a fiber-coupled photon counter. As before, application of a pi pulse such that

$(\Omega'_{2C}g'_F/2\delta)\tau'_R = \pi$ would produce a single photon in the g'_F mode only if Ens-II is in state $|C_1\rangle$; otherwise, there would be no photons in this mode. Note, again, that there is no \sqrt{N} factor involved in this expression. A coincidence between the photon counts found in the g_F and the g'_F modes will prove that the controlled-NOT gate was applied correctly, and confirm the entanglement between the ensembles. The transitions are illustrated schematically in Fig. 9(b).

- [1] R. H. Dicke, Phys. Rev. **93**, 99 (1954).
- [2] L. M. Duan, M. D. Lukin, J. I. Cirac, and P. Zoller, Nature (London) **414**, 413 (2001).
- [3] L. M. Duan, J. I. Cirac, and P. Zoller, Phys. Rev. A **66**, 023818 (2002).
- [4] G. K. Brennen, I. H. Deutsch, and P. S. Jessen, Phys. Rev. A **61**, 062309 (2000).
- [5] M. D. Lukin, M. Flieschhauer, R. Cote, L. M. Duan, D. Jacksch, J. I. Cirac, and P. Zoller, Phys. Rev. Lett. **87**, 037901 (2001).
- [6] M. S. Shahriar, P. Pradhan, G. S. Pati, and K. Salit, e-print quant-ph/0604120, Opt. Lett. (to be published).
- [7] T. Pellizzari, S. A. Gardiner, J. I. Cirac, and P. Zoller, Phys. Rev. Lett. **75**, 3788 (1995).
- [8] S. Lloyd, M. S. Shahriar, J. H. Shapiro, and P. R. Hemmer, Phys. Rev. Lett. **87**, 167903 (2001).
- [9] S. Lloyd, J. Shapiro, F. Wong, P. Kumar, M. S. Shahriar, and H. Yuen, Comput. Commun. Rev. **34**, 9 (2004).
- [10] D. Gottesman and I. Chuang, Nature (London) **402**, 392

- (1999).
- [11] J. A. Sauer, K. M. Fortier, M. S. Chang, C. D. Hamley, and M. S. Chapman, *Phys. Rev. A* **69**, 051804 (2004).
- [12] W. Alt, D. Schrader, S. Kuhr, M. Muller, V. Gomer, and D. Meschede, *Phys. Rev. A* **67**, 033403 (2003).
- [13] P. Kruger, X. Luo, M. W. Klein, K. Brugger, A. Haase, S. Wildermuth, S. Groth, I. Bar-Joseph, R. Folman, and J. Schmiedmayer, *Phys. Rev. Lett.* **91**, 233201 (2003).
- [14] R. Dumke, M. Volk, T. Muther, F. B. J. Buchkremer, G. Birkl, and W. Ertmer, *Phys. Rev. Lett.* **89**, 097903 (2002).
- [15] G. Birkl, F. B. J. Buchkremer, R. Dumke, and W. Ertmer, *Opt. Commun.* **191**, 67 (2001).
- [16] A. V. Turukhin, V. S. Sudarshanam, M. S. Shahriar, J. A. Musser, B. S. Ham, and P. R. Hemmer, *Phys. Rev. Lett.* **88**, 023602 (2002).
- [17] M. S. Shahriar, P. R. Hemmer, S. Lloyd, P. S. Bhatia, and A. E. Craig, *Phys. Rev. A* **66**, 032301 (2002).
- [18] M. S. Shahriar, J. Bowers, S. Lloyd, P. R. Hemmer, and P. S. Bhatia, *Opt. Commun.* **195**, 5 (2001).
- [19] This can be seen as follows. For a Gaussian cavity mode, the effective mode diameter increases away from the center. As such, the amplitude of the electric field also drops off, in a manner so that the system is equivalent to a uniform intensity over the whole length of the cavity, with an effective diameter that is the same as that at the center.
- [20] C. J. Hood, T. W. Lynn, A. C. Doherty, A. S. Parkins, and H. J. Kimble, *Science* **287**, 1447 (2000).
- [21] G. Rempe, R. J. Thompson, H. J. Kimble, and R. Lalezari, *Opt. Lett.* **17**, 363 (1992).

B.4. Ultra-Low Power Non-Linear Optics in a Tapered Nanofiber as an Enabling Technology for Optically Linking Ensemble-Based Quantum Bits

Summary:

As described in section B.3 above, we have developed a new model of optical quantum computing using atomic ensembles as quantum bits. In our original model, these would make use of moderate-Q cavities in order to couple nearest neighbor quantum bits for CNOT operations. Alternatively, the coupling can be mediated by the evanescent field of a tapered nano-fiber (TNF). A key advantage of using the TNF for this purpose is that it can be effortlessly connected to regular optical fibers, thereby linking multiple quantum computers in the form of a quantum internet, or for Type-II quantum computing.

Under this grant, we have studied the extremely strong interaction between the evanescent field of a TNF and an atomic vapor. Specifically, we have observed ultra-low light level non-linear optical interactions in a TNF embedded in a hot rubidium vapor as well as in a cloud of trapped atoms. The small optical mode area plays a significant role in the optical properties of the hot vapor Rb-TNF system, allowing nonlinear optical interactions with nW level powers in a hot vapor even in the presence of transit-time dephasing rates much larger than the intrinsic linewidth. We demonstrate nonlinear absorption and V-type electromagnetically-induced transparency with cw powers below 10 nW, comparable to the best results in any Rb-optical waveguide system. Using a cloud of trapped atoms, we have also been able to see such an interaction at 100 pW. The good performance and flexibility of the Rb-TNF system makes it a very promising candidate for ultra-low power resonant nonlinear optical applications in general, and ensemble quantum computing in particular.

Reproduction of published journal paper: (4 pages)

This work has been *accepted* for publication in *Physical Review Letters*, and is reproduced below.

Observation of Ultra-Low Light Level Nonlinear Optical Interactions in a Tapered Optical Nanofiber Embedded in a Hot Rubidium Vapor

S. M. Spillane¹, G. S. Pati², K. Salit², M. Hall², P. Kumar², R. G. Beausoleil¹, and M. S. Shahriar²

¹*Hewlett-Packard Laboratories, Palo Alto, CA 94304*

²*Department of EECS, Northwestern University, Evanston, IL 60208*

(Dated: March 16, 2008)

We report the observation of low-light level optical interactions in a tapered optical nanofiber (TNF) embedded in a hot rubidium vapor. The small optical mode area plays a significant role in the optical properties of the hot vapor Rb-TNF system, allowing nonlinear optical interactions with nW level powers even in the presence of transit-time dephasing rates much larger than the intrinsic linewidth. We demonstrate nonlinear absorption and V-type electromagnetically-induced transparency with cw powers below 10 nW, comparable to the best results in any Rb-optical waveguide system. The good performance and flexibility of the Rb-TNF system makes it a very promising candidate for ultra-low power resonant nonlinear optical applications.

PACS numbers: 42.50.Gy, 42.81.Qb

The interaction of light with atomic ensembles[1–3] has created a number of advancements in generating and controlling classical and quantum states of light[4–6]. In order to enable optical interactions with few photons (as desired in some quantum information processing studies[7]), much effort has been invested into increasing the interaction between atoms and photons. This is often done by employing high finesse optical microcavities, where quantum effects are readily observed between a single atom and a single photon[8–11]. However, these systems are extremely complicated. For applications where single-photon interactions are not needed, atomic ensembles in a simple nonresonant geometry are used to observe quantum optic effects. Previously, most work was performed with optical beams focused into an alkali vapor, where the use of a bulk, free-space geometry fundamentally limited the interaction strength and/or length[6]. Recent experiments have resulted in significant increases in both interaction strength and interaction length by enclosing an atomic vapor into a waveguide[12, 13], with V-system electromagnetically-induced transparency (EIT) demonstrated in a photonic crystal fiber with approximately 3 nW of pulsed power[12]. In both of these cases, the enhanced interaction comes from reducing the optical mode area. Here we explore the use of tapered optical nanofibers (TNF) with optical mode areas smaller than in previous experiments, and demonstrate low light level nonlinear interactions with a rubidium atomic vapor.

A TNF consists of a single-mode silica optical fiber where the original fiber diameter is reduced to the sub-micron range. In this system, the optical mode which was initially guided by the core/cladding interface is adiabatically converted with negligible loss[14] into a mode guided by the cladding/environment interface. The evanescent field extends into the surrounding environment, which for the purposes of this work consists of a rubidium atom vapor. The use of an evanescent interaction maintains the benefit of independently controlling the

interaction strength (through cross-sectional geometry) and length (due to the invariance of the evanescent field along the waveguide), and allows an increase of interaction strength over previous waveguide approaches[12, 13]. This system has been previously used to study evanescent interactions with Cs atoms, such as probing atom fluorescence[15, 16]. In principle the interaction length can be arbitrary long, just like in any waveguide, with a limit due to intrinsic optical waveguide loss. For a TNF of diameter 400 nm, approximately 10% of the optical field interacts with the rubidium vapor. For this diameter, we estimate that the total number of atoms interacting with the TNF as 1400/cm, which for the typical taper length of 3 mm in this work gives a total number of atoms of ≈ 450 (assuming a Rb atomic density of 6×10^{12} atoms/cm³ for a vapor at 100°C).

We have investigated numerically the performance of the Rb-TNF system for different TNF geometries. Figure 1 shows a plot of the fraction of the optical energy located in the evanescent field and the optical mode area for a TNF versus diameter for an optical wavelength of 780 nm, corresponding to the Rb D₂ manifold. We see that as the diameter decreases the fraction of the optical energy that extends into the external Rb vapor increases monotonically. The optical mode area decreases as the diameter decreases to about 0.45 μm due to the added dielectric confinement, corresponding to a minimum optical mode area of 0.18 μm^2 . As the diameter is reduced further, the mode quickly delocalizes, causing a rise in mode area. This minimum mode area is significantly smaller than that found in alternate waveguiding geometries ($> 10\times$ smaller than ARROW waveguides[13] and $> 100\times$ smaller than PCF waveguides[12]), and is comparable to the atomic scattering cross-section of $3\lambda^2/2\pi$. Therefore, we expect that the TNF should have a dramatically increased interaction with an atomic vapor.

However, in an open environment such as the Rb-TNF system, this mode area is so miniscule that a single atom

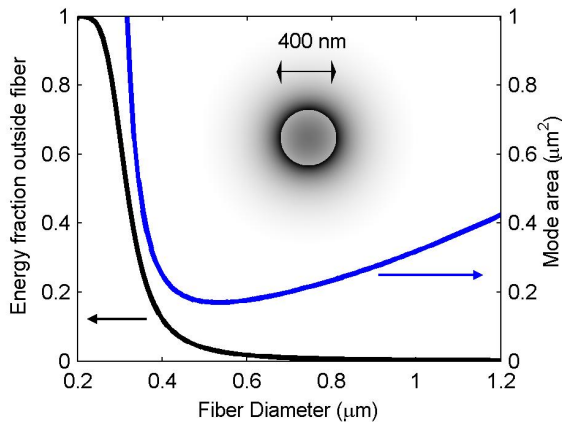


FIG. 1: Calculated mode area and external energy fraction for a TNF ($\lambda=780$ nm). Inset shows the electric field distribution for the fundamental mode of a 400 nm diameter TNF.

(with a velocity typically found in a hot vapor cell) passes through the optical field of the TNF in a few nanoseconds. This time is much shorter than the intrinsic decay time of the atom (≈ 25 ns), leading to an effect known as transit-time broadening. Fundamentally, transit-time broadening can be understood by considering the optical interaction in the atom's reference frame. Here, the stationary atom experiences a temporally-varying optical field, with a temporal shape dependent on the transverse optical mode field. In this case, the optical absorption linewidth is given by a combination of the intrinsic atomic decay rate and the transit time decay rate (determined from the Fourier transform of the time-varying optical field), leading to a broader absorption line when transit-time effects dominate. Additionally, the presence of transit-time broadening can significantly increase the threshold to observe nonlinear interactions. Figure 2 shows a calculation of the transit time dephasing rate expected for a Rb vapor interacting with a TNF of various diameters. For this calculation we used the exact TNF optical field profile to determine the dephasing rate for an atom passing through the evanescent field, assuming an isotropic angular distribution and that the atoms which struck the TNF bounced off with no delay and without dephasing (this gives an estimate of the smallest transit time linewidth possible). This procedure was performed for all possible atomic speeds, with the final linewidth determined by integrating over a Maxwell-Boltzmann velocity distribution for a vapor with a temperature of 100°C . The calculation shows that dephasing rates are on the order of 100 MHz, which is much larger than the intrinsic atom linewidth (≈ 6 MHz), with a minimum value of 89 MHz for a TNF diameter of 400 nm.

An easy way to describe the suitability of a system for nonlinear optical effects is to consider the power needed to saturate an atomic vapor. This is given by the relation

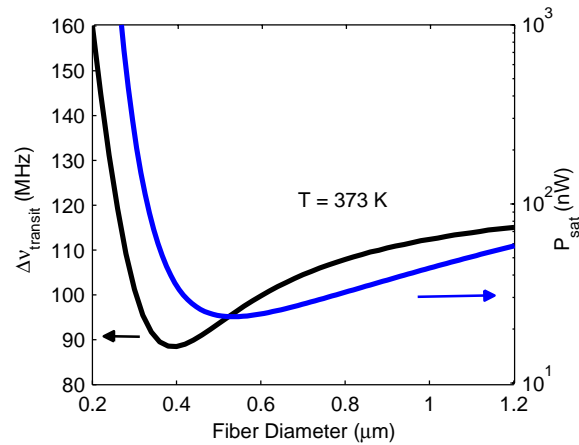


FIG. 2: Calculated transit time linewidth and saturation power for a hot rubidium vapor (vapor temperature of 100°C) coupled to a TNF. The saturation calculation assumes an intrinsic saturation intensity of 1.5 mW/cm 2 and a Doppler width of 575 MHz for the bulk vapor.

$P_{sat} = I_{sat} A_m (\gamma_T / \gamma_0)^2$, where I_{sat} is the saturation intensity for an atomic transition, A_m is the optical mode area, and γ_T / γ_0 represents the ratio of the total linewidth (including transit time dephasing and Doppler broadening) and the intrinsic linewidth. Figure 2 shows the calculated nonlinear saturation power as a function of diameter corresponding to an isotropic Rb vapor of 100°C , with $I_{sat} = 1.5$ mW/cm 2 for the D_2 manifold. In this case the Doppler width of 575 MHz is much larger than transit time dephasing, so that the calculated saturation power is effectively independent of transit time. The data show that due to the small mode area the nonlinear saturation power is on the order of tens of nanowatts even in the presence of significant Doppler broadening.

In our experimental setup (Fig. 3(a)), a TNF was inserted into a chamber containing hot rubidium vapor, which contained a natural mixture of Rb 85 and Rb 87 isotopes. A Newport single mode fiber at 780 nm was drawn adiabatically into a TNF with a waist diameter of approximately 400 nm using the 'flame-brush' technique[17] with a hydrogen-air torch. The resulting taper profile is nearly exponential with a $1/e$ length of ≈ 3 mm. During the adiabatic tapering process, monitoring of fiber transmission showed negligible loss (ranging from 1 – 10%) for final taper waist diameters of approximately 400 nm. The TNF is mounted to a copper chuck using UV-curable epoxy and inserted into the vacuum chamber using a set of Teflon fiber feedthroughs[18], which maintain fiber continuity into and out of the vacuum chamber. A gate valve isolates the optical fiber during loading/unloading from a rubidium metal source. During experiments, the vacuum chamber was heated to $\approx 100^\circ\text{C}$ (to minimize Rb condensation), and Rb vapor was created by heating the source region to $\approx 200^\circ\text{C}$, with the chamber pressure

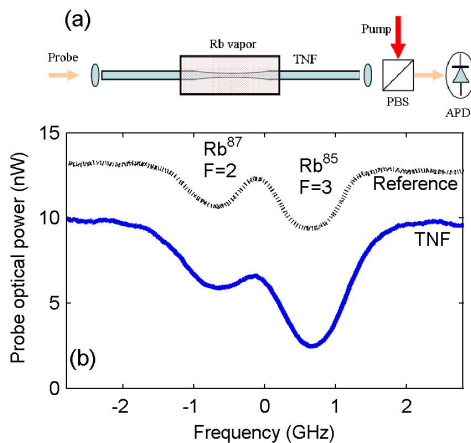


FIG. 3: (a) Diagram of the experimental setup. The tapered nanofiber passes through the Rb vapor-containing chamber using teftlon fiber feedthroughs. A polarization beamsplitter is used to inject a strong counterpropagating cross-polarized pump for the saturated absorption and EIT measurements. (b) Transmitted spectrum for a TNF and reference cell for the D_2 manifold of Rb vapor at 780 nm.

maintained at 5 mTorr by a roughing pump. For these measurements, we made no attempt to prevent dephasing for atoms which struck the TNF. Assuming the vapor inside the chamber is at an average temperature of 100°C , the atomic density is estimated to be $6 \times 10^{12}/\text{cm}^3$.

For the first set of experiments, a weak probe beam (approximately 10 nW) obtained from a Ti:Sapphire laser was transmitted through the TNF, and the optical transmission was monitored with an avalanche photodiode. The frequency of the probe was scanned over the Doppler broadened spectrum of the D_2 manifold. Figure 3(b) shows the transmission spectrum through the TNF (lower spectrum), and a reference Rb vapor cell kept at 100°C (upper spectrum). The dip on the left corresponds to the $F=2$ to $F'=2$ transition in the D_2 manifold of Rb^{87} , while the dip on the right corresponds to the $F=3$ to $F'=3$ transition in the same manifold of Rb^{85} . Far away from resonance, the probe was found to be attenuated by about 20% due to a combination of losses at the input couplers and by TNF absorption. The data clearly show transmission dips representative of rubidium vapor absorption, with peak locations similar to that of the reference cell. However, the shape of the transmission dips for the Rb-TNF system is slightly different than that for the reference cell, which is due to both differences in Doppler broadening and transit time dephasing present in this experimental measurement.

In optical saturation, the nonlinear absorption coefficient $\alpha_{NL} = \alpha_0/(1 + P/P_{sat})$, where α_0 is the linear absorption coefficient and P is the incident optical power. As the incident optical power increases in a nonlinear medium, the relative absorption decreases, and therefore the relative transmission increases. Figure 4 shows the

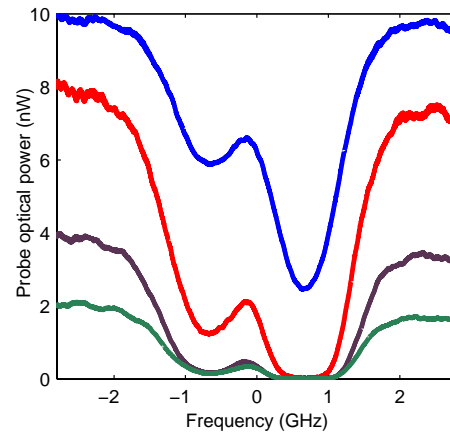


FIG. 4: Transmission spectrum for a TNF for increasing probe powers of {2, 4, 8, 10}nW for the Rb D_2 transition. The spectra show optical saturation with a saturation power of ≈ 8 nW.

transmitted power spectrum measured for a variety of incident power levels for a TNF with a waist diameter of approximately 400 nm. On the left edge, the output power is close to its value observed far away from resonance. The bottom (green) trace corresponds to an off-resonant, output probe power of about 2 nW. At this power level, the probe is found to be absorbed very strongly. As the probe power is increased, the relative transmission increases, as expected for a nonlinear medium. The absorption decrease with incident power can be used to extract the saturation power, which is approximately 8 nW. This value is lower than the theoretical value which we attribute to a nonisotropic atomic vapor in our experiment. Assuming an effective Doppler width of 210 MHz (inferred from measurements described below), we obtain a predicted saturation power of 4 nW. Accounting for the TNF profile, the saturation power increases to ≈ 8 nW, in good agreement with the measurement.

Next, a pump-probe measurement was performed, with the strong counterpropagating pump beam cross-polarized with respect to the probe. This measurement was performed on the D_1 manifold in order to delineate more clearly the spectral features in the presence of large transit time broadening. Figure 5 illustrates the probe transmission spectrum (power ≈ 1 nW) for counterpropagating pump powers of 10 nW (middle, green) and 30 nW (lower, red), for a TNF with a waist diameter of approximately 400 nm. For comparison, a reference trace is also shown for a conventional vapor cell (blue). The peaks on the left and the right correspond to self-induced transparency (SIT) for Rb^{85} atoms with zero axial velocities, corresponding to the $F=3-F'=2$ and the $F=3-F'=3$ hyperfine transitions, respectively. This measurement is similar to that of conventional saturated absorption spectroscopy, with a V-type three level EIT

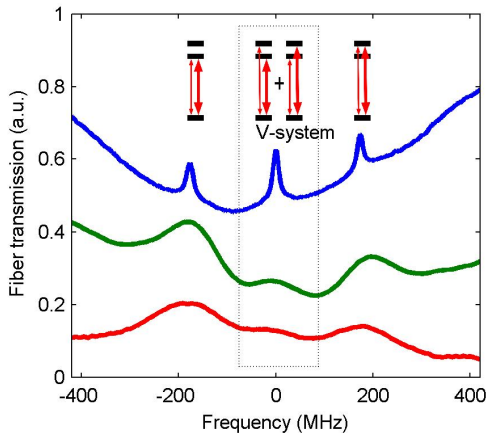


FIG. 5: Saturated absorption spectrum with cross-polarized pump and probe beams for a Rb vapor cell (blue) and a Rb-TNF system (green and red) for the D_1 manifold of Rb^{85} . The two side peaks correspond to the Doppler-free $F=3-F'=2$ and $F=3-F'=3$ hyperfine lines, which are composed of atoms with near zero longitudinal velocity. These widths indicate the power-broadened hyperfine linewidth, including transit time dephasing. The center peak corresponds to V-system EIT.

peak (with orthogonally polarized pump and probe) located at the cross-over resonance location. This peak is comprised of V-type EIT measurements of two groups of atoms (illustrated in figure 5): (a) one with an axial velocity such that the probe excites the $F=3-F'=3$ transition and the pump excites the $F=3-F'=2$ transition, and (b) the other with an equal but opposite axial velocity so that the probe excites the $F=2-F'=3$ transition and the pump excites the $F=3-F'=2$ transition. The EIT signal for the TNF is readily apparent for the lower pump power measurement, where the peak is clearly separated from the SIT peaks. The amplitude of this peak is measurably greater than the background signal for both the low and high power spectra, even though the high power spectrum is less resolvable due to power broadening.

For the conventional vapor cell, the transparency seen at the EIT resonance is larger than that at the SIT peaks due to the larger number of atoms in the combined ± 180 MHz Doppler-shifted groups (there is approximately 1.5 times the number of atoms in an isotropic vapor cell, which arises from the 575 MHz width of the Doppler distribution) than the individual zero axial velocity groups. Furthermore, the peak widths are the power broadened individual hyperfine transitions (≈ 6 MHz power broadened to ≈ 18 MHz). However, for the TNF signal, there is a noticeable difference between the linewidths and relative amplitudes of the SIT and EIT peaks. Here, the line broadening for the lower (middle) power curve is due primarily to the transit time effect. The transit time broadening is about 110 MHz, close to the theoretical prediction. The dramatically smaller amplitude of the V-system EIT peak in the TNF measurement is

likely due to a nonisotropic atomic velocity distribution in the Rb-TNF cell, which leads to a smaller population of atoms with the correct longitudinal Doppler-shifted velocity component for the EIT interaction. The relative magnitude of the three absorption peaks is consistent with a 210 MHz wide effective Doppler distribution, which also gives good agreement with the saturation power data in figure 4. The effective reduction of the Doppler width may be attributable to the geometry of the cell and the relative position of the TNF and the vacuum pump. Further investigation will be carried out in the future to study this effect.

In conclusion, we have shown that a TNF coupled to a Rb vapor exhibits optical saturation and EIT at very low pump power levels below 10 nW, comparable to the best results in any Rb-waveguide system. Numerical modeling indicates that the TNF's small mode area results in a significant linewidth broadening due to the short transit time of hot Rb atoms through the evanescent field, which combined with Doppler broadening increases the threshold for nonlinear optical effects. However, this is a limitation of the large atomic velocities in a high temperature Rb vapor, which can be reduced in principle. In particular, the use of cooled atoms from a magneto-optic trap[15, 16] will allow the elimination of transit time and Doppler broadening, which should lead to nonlinear interactions with pW level optical powers.

This work was supported in part by the Hewlett-Packard Co. through DARPA and the Air Force Office of Scientific Research under AFOSR contract no. FA9550-07-C-0030, and by AFOSR Grant Number FA9550-04-1-0189.

-
- [1] S. E. Harris, *Phys. Today* **50**, 36 (1997).
 - [2] M. D. Lukin, *Rev. Mod. Phys.* **75**, 457 (2003).
 - [3] M. Fleischhauer, A. Imamoglu, and J. P. Marangos, *Rev. Mod. Phys.* **77**, 633 (2005).
 - [4] S. E. Harris and Y. Yamamoto, *Phys. Rev. Lett.* **81**, 3611 (1998).
 - [5] M. C. Dawes *et al.*, *Science* **308**, 672 (2005).
 - [6] D. A. Braje *et al.*, *Phys. Rev. A* **68**, 041801(R) (2003).
 - [7] R. G. Beausoleil *et al.*, *J. Mod. Opt.* **51**, 2441 (2004).
 - [8] C. J. Hood *et al.*, *Phys. Rev. Lett.* **80**, 4157 (1998).
 - [9] C. J. Hood *et al.*, *Science* **287**, 1447 (2000).
 - [10] S. M. Spillane *et al.*, *Phys. Rev. A* **71**, 013817 (2005).
 - [11] T. Aoki *et al.*, *Nature* **443**, 671 (2006).
 - [12] S. Ghosh *et al.*, *Phys. Rev. Lett.* **97**, 023603 (2006).
 - [13] W. Yang *et al.*, *Nature Photonics* **1**, 331 (2007).
 - [14] G. Brambilla, V. Finazzi, and D. J. Richardson, *Optics Express* **12**, 2258 (2004).
 - [15] K. P. Nayak *et al.*, *Optics Express* **15**, 5431 (2007).
 - [16] G. Sague *et al.*, *Phys. Rev. Lett.* **99**, 163602 (2007).
 - [17] T. A. Birks and Y. W. Li, *IEEE J. Light. Technol.* **10**, 432 (1992).
 - [18] E. R. I. Abraham and E. A. Cornell, *App. Opt.* **37**, 1762 (1998).

B.5. Identification and Elimination of Driver Phase Correlated Fluctuations in the Rotation of a Strongly Driven Quantum Bit

Summary:

The need to maximize the number of operations of a quantum bit within its decoherence time may require the ratio of Rabi frequency to transition frequency to be large enough to invalidate the rotating-wave approximation. This is particularly important for the quantum computing model in NV-diamond, and is also relevant for the atomic ensemble based quantum computing model summarized in section B.3. We have shown, under work performed for this grant, that the state of the quantum bit under any initial condition in such a case depends explicitly on the phase of the driving field, resulting in driver-phase-correlated fluctuations and a violation of the rule that the degree of excitation depends only on the pulse area. This is due to the interference of the excitations caused by the co-rotating and counter-rotating fields, and is a significant source of error, correctable only by controlling the driver phase.

This effect also shows how one can measure the amplitude and absolute (i.e., temporal and initial) phase of a monochromatic microwave field at a specific point of space and time. In addition to suppressing error in high-speed quantum computing, this measurement process has other potential applications, including wavelength quantum teleportation. We have shown how such a measurement can indeed be made using resonant atomic probes via detection of incoherent fluorescence induced by a laser beam. This measurement is possible due to self-interference effects between the positive- and negative-frequency components of the field. In effect, the small cluster of atoms here act as a highly localized pickup coil, and the fluorescence channel acts as a transmission line.

Reproduction of published journal papers: (4+4 pages)

This work has been published in two articles in Physical Review A. These are reproduced below.

(Note: the first paper was carried with support from the precursor to this grant; however, it is included here since it provides the background material for the second paper).

Driver-phase-correlated fluctuations in the rotation of a strongly driven quantum bitM. S. Shahriar,^{1,2} Prabhakar Pradhan,^{1,2} and Jacob Morzinski²¹*Department of Electrical and Computer Engineering, Northwestern University, Evanston, Illinois 60208, USA*²*Research Laboratory of Electronics, Massachusetts Institute of Technology, Cambridge, Massachusetts 02139, USA*

(Received 20 July 2002; published 16 March 2004)

The need to maximize the number of operations of a quantum bit within its decoherence time may require the ratio of Rabi frequency to transition frequency to be large enough to invalidate the rotating-wave approximation. The state of the quantum bit under any initial condition then depends explicitly on the phase of the driving field, resulting in driver-phase-correlated fluctuations and a violation of the rule that the degree of excitation depends only on the pulse area. This is due to the interference of the excitations caused by the corotating and counterrotating fields, and is a significant source of error, correctable only by controlling the driver phase. We present a scheme for observing this effect under currently realizable parameters.

DOI: 10.1103/PhysRevA.69.032308

PACS number(s): 03.67.Hk, 03.67.Lx, 32.80.Qk

In order to minimize the decoherence rate of a two-state quantum bit (qubit) embodied in a massive particle, one often chooses to use low-energy transitions. In general, one is interested in performing these transitions as fast as possible [1–5] which demands a strong Rabi frequency. The ratio of Rabi frequency to qubit transition frequency is therefore not necessarily very small, thus invalidating the so-called rotating-wave approximation (RWA). A key effect due to violation of the RWA (VRWA) is the so-called Bloch-Siegert shift [6–9] which is negligible in optical transitions, but is manifested in nuclear magnetic resonance [10]. Here, we show that VRWA leads to another important effect, which can lead to controllable errors that are significant on the scale of precisions envisioned for a functioning quantum computer [11]. Specifically, we show that under VRWA the population difference between the two levels of the quantum bit, with any initial condition, depends explicitly on the phase of the driving field at the onset of an excitation pulse, which is a violation of the rule [6] that for a two-level system starting in the ground state, the population difference is a function of the integral of the field amplitude over the pulse duration and does not depend on the phase of the field. We provide a physical interpretation of this effect in terms of an interference of the excitations caused by the corotating and counterrotating fields, and present a scheme for observing this effect under currently realizable parameters.

To see the implication of this result, consider a scenario where one has a qubit, initialized to the ground state, and would like to prepare it to be in an equal superposition of the ground and excited states. To this end, one would apply a resonant pulse with an area of $\pi/2$ starting at a time $t=t_0$. Under the RWA, one does not have to know what the absolute phase of the field, ϕ_p , is at t_0 , and the population difference for the qubit would be zero. Under VRWA, however, the desired excitation would only occur if $\phi_p=0$. Otherwise, the population difference would have a component varying as $\eta \sin(2\phi_p)$, where η is a parameter that is proportional to the ratio of Rabi frequency to transition frequency. Suppose one has to apply this pulse to many such qubits, with a potentially different ϕ_p for each (e.g., because the pulses are applied at different times or the qubits are spatially sepa-

rated), but with identical pulse areas. The population difference for the qubits will then exhibit a fluctuation, correlated to their respective values of ϕ_p . For a quantum computer, this variation would represent a source of error. For some experiments (e.g., Ref. [5]), the value of η is already close to 0.01, so that the magnitude of this error is much larger than the ultimate accuracy (10^{-6}) desirable for a large-scale quantum computer [11] and must be controlled.

To illustrate this effect, we consider an ideal two-level system where a ground state $|0\rangle$ is coupled to a higher-energy state $|1\rangle$. We also assume that the $0\leftrightarrow 1$ transition is magnetic dipolar, with a transition frequency ω , and the magnetic field is of the form $B=B_0 \cos(\omega t + \phi)$. We now summarize briefly the two-level dynamics without the RWA. In the dipole approximation, the Hamiltonian can be written as

$$\hat{H} = \epsilon(\sigma_0 - \sigma_z)/2 + g(t)\sigma_x, \quad (1)$$

where $g(t) = -g_0[\exp(i\omega t + i\phi) + \text{c.c.}]/2$, σ_i are the Pauli matrices, and $\epsilon = \omega$ corresponds to resonant excitation. The state vector is written as

$$|\xi(t)\rangle = \begin{bmatrix} C_0(t) \\ C_1(t) \end{bmatrix}. \quad (2)$$

We perform a rotating-wave transformation by operating on $|\xi(t)\rangle$ with the unitary operator \hat{Q} , where

$$\hat{Q} = (\sigma_0 + \sigma_z)/2 + \exp(i\omega t + i\phi)(\sigma_0 - \sigma_z)/2. \quad (3)$$

The Schrödinger equation then takes the form (setting $\hbar=1$) $|\tilde{\xi}\rangle = -iH(t)|\tilde{\xi}(t)\rangle$ where the effective Hamiltonian is given by

$$\tilde{H} = \alpha(t)\sigma_+ + \alpha^*(t)\sigma_-, \quad (4)$$

with $\alpha(t) = -(g_0/2)[\exp(-i2\omega t - i2\phi) + 1]$, and in the rotating frame the state vector is

$$|\tilde{\xi}(t)\rangle \equiv \hat{Q}|\xi(t)\rangle = \begin{bmatrix} \tilde{C}_0(t) \\ \tilde{C}_1(t) \end{bmatrix}. \quad (5)$$

Now, one may choose to make the RWA, corresponding to dropping the fast-oscillating term in $\alpha(t)$. This corresponds to ignoring effects (such as the Bloch-Siegert shift) of the order of (g_0/ω) , which can easily be observable in an experiment if g_0 is large [6–10]. On the other hand, by choosing g_0 to be small enough, one can make the RWA for any value of ω . We explore both regimes in this paper. As such, we find the general results without the RWA.

From Eqs. (4) and (5), one gets two coupled differential equations

$$\dot{\tilde{C}}_0(t) = -(g_0/2)[1 + \exp(-i2\omega t - i2\phi)]\tilde{C}_1(t), \quad (6a)$$

$$\dot{\tilde{C}}_1(t) = -(g_0/2)[1 + \exp(+i2\omega t + i2\phi)]\tilde{C}_0(t). \quad (6b)$$

We assume $|C_0(t)|^2 = 1$ to be the initial condition and proceed further to find an approximate analytical solution of Eq. (6). Given the periodic nature of the effective Hamiltonian, the general solution to Eq. (6) can be written in the form

$$|\tilde{\xi}(t)\rangle = \sum_{n=-\infty}^{\infty} \begin{bmatrix} a_n \\ b_n \end{bmatrix} \exp[n(-i2\omega t - i2\phi)]. \quad (7)$$

Inserting Eq. (7) into Eq. (6) and equating coefficients with same the frequencies, one gets for all n ,

$$\dot{a}_n = i2n\omega a_n + ig_0(b_n + b_{n-1})/2, \quad (8a)$$

$$\dot{b}_n = i2n\omega b_n + ig_0(a_n + a_{n+1})/2. \quad (8b)$$

Here, the coupling between a_0 and b_0 is the conventional one present when the RWA is made. The couplings to the nearest neighbors, $a_{\pm 1}$ and $b_{\pm 1}$, are detuned by an amount 2ω and so on. To the lowest order in (g_0/ω) , we can ignore terms with $|n| > 1$, thus yielding a truncated set of six equations

$$\dot{a}_0 = ig_0(b_0 + b_{-1})/2, \quad (9a)$$

$$\dot{b}_0 = ig_0(a_0 + a_1)/2, \quad (9b)$$

$$\dot{a}_1 = i2\omega a_1 + ig_0(b_1 + b_0)/2, \quad (9c)$$

$$\dot{b}_1 = i2\omega b_1 + ig_0 a_1/2, \quad (9d)$$

$$\dot{a}_{-1} = -i2\omega a_{-1} + ig_0 b_{-1}/2, \quad (9e)$$

$$\dot{b}_{-1} = -i2\omega b_{-1} + ig_0(a_{-1} + a_0)/2. \quad (9f)$$

We consider g_0 to have a time dependence of the form $g_0(t) = g_{0M}[1 - \exp(-t/\tau_{sw})]$, where the switching time constant $\tau_{sw} \gg \omega^{-1}, g_{0M}^{-1}$. We can solve these equations by employing the method of adiabatic elimination, which is valid to first order in $\eta \equiv (g_0/4\omega)$. Note that η is also a function of time and can be expressed as $\eta(t) = \eta_0[1 - \exp(-t/\tau_{sw})]$,

where $\eta_0 \equiv (g_{0M}/4\omega)$. We consider first Eqs. (9e) and (9f). In order to simplify these two equations further, one needs to diagonalize the interaction between a_{-1} and b_{-1} . Define $\mu_- \equiv (a_{-1} - b_{-1})$ and $\mu_+ \equiv (a_{-1} + b_{-1})$, which now can be used to reexpress these two equations in a symmetric form as

$$\dot{\mu}_- = -i(2\omega + g_0/2)\mu_- - ig_0 a_0/2, \quad (10a)$$

$$\dot{\mu}_+ = -i(2\omega - g_0/2)\mu_+ + ig_0 a_0/2. \quad (10b)$$

Adiabatic following then yields (again, to lowest order in η) $\mu_- \approx -\eta a_0$ and $\mu_+ \approx \eta a_0$, which in turn yields $a_{-1} \approx 0$ and $b_{-1} \approx \eta a_0$. In the same manner, we can solve Eqs. (9c) and (9d), yielding $a_1 \approx -\eta b_0$ and $b_1 \approx 0$.

Note that the amplitudes of a_{-1} and b_1 are vanishing (each proportional to η^2) to lowest order in η and thereby justifying our truncation of the infinite set of relations in Eq. (9). It is easy to show now

$$\dot{a}_0 = ig_0 b_0/2 + i\Delta(t)a_0/2, \quad (11a)$$

$$\dot{b}_0 = ig_0 a_0/2 - i\Delta(t)b_0/2, \quad (11b)$$

where $\Delta(t) = g_0^2(t)/4\omega$ is essentially the Bloch-Siegert shift. Equation (11) can be thought of as a two-level system excited by a field detuned by Δ . For simplicity, we assume that this detuning is dynamically compensated for by adjusting the driving frequency ω . This assumption does not affect the essence of the results to follow, since the resulting correction to η is negligible. With the initial condition of all the population in $|0\rangle$ at $t=0$, the only nonvanishing (to lowest order in η) terms in the solution of Eq. (9) are

$$a_0(t) \approx \cos[g'_0(t)t/2], \quad b_0(t) \approx i \sin[g'_0(t)t/2],$$

$$a_1(t) \approx -i\eta \sin[g'_0(t)t/2], \quad b_{-1}(t) \approx \eta \cos[g'_0(t)t/2],$$

where

$$g'_0(t) = 1/t \int_0^t g_0(t') dt' = g_0[1 - (t/\tau_{sw})^{-1} \exp(-t/\tau_{sw})].$$

We have verified this solution via numerical integration of Eq. (6) as shown later. Inserting this solution into Eq. (6) and reversing the rotating-wave transformation, we get the following expressions for the components of Eq. (2):

$$C_0(t) = \cos[g'_0(t)t/2] - 2\eta \Sigma \sin[g'_0(t)t/2], \quad (12a)$$

$$C_1(t) = ie^{-i(\omega t + \phi)} \{ \sin[g'_0(t)t/2] + 2\eta \Sigma^* \cos[g'_0(t)t/2] \}, \quad (12b)$$

where we have defined $\Sigma \equiv (i/2)\exp[-i(2\omega t + 2\phi)]$. To lowest order in η , this solution is normalized at all times. Note that if one wants to carry this excitation on an ensemble of atoms using a $\pi/2$ pulse and measure the population of the state $|1\rangle$ after the excitation terminates [at $t=\tau$ when $g'(\tau)\tau/2 = \pi/2$], the result would be an output signal given by

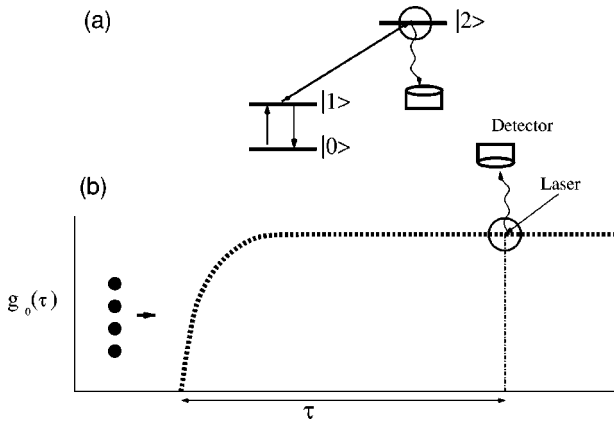


FIG. 1. Schematic illustration of an experimental arrangement for measuring the phase dependence of the population of the excited state $|1\rangle$: (a) The microwave field couples the ground state ($|0\rangle$) to the excited state ($|1\rangle$). A third level, $|2\rangle$, which can be coupled to $|1\rangle$ optically, is used to measure the population of $|1\rangle$ via fluorescence detection. (b) The microwave field is turned on adiabatically with a switching time constant τ_{sw} , and the fluorescence is monitored after a total interaction time of τ .

$$|C_1(g'_0(\tau), \phi)|^2 = \frac{1}{2}[1 + 2\eta \sin(2\phi_\tau)], \quad (13)$$

where we have defined the phase of the field at $t = \tau$ to be $\phi_\tau \equiv \omega\tau + \phi$. This signal contains information of both the amplitude and phase of the driving field.

This result can be appreciated best by considering an experimental arrangement of the type illustrated in Fig. 1. Consider, for example, a collection of ^{87}Rb atoms, caught in a dipole force trap, where the states $|0\rangle \equiv 5^2S_{1/2}:|F=1, m=1\rangle$ and $|1\rangle \equiv 5^2S_{1/2}:|F=2, m=2\rangle$ form the two-level system. These states differ in frequencies by 6.683 47 GHz. When illuminated by resonant right-circularly polarized light at a frequency of 3.844×10^{14} Hz, state $|1\rangle$ couples only to the state $|2\rangle \equiv 5^2P_{3/2}:|F=3, m=3\rangle$, which in turn can decay only to state $|1\rangle$. This cycling transition can thus be used to pump the system into state $|1\rangle$. When a right-circularly polarized microwave field at 6.683 47 GHz is applied, state $|1\rangle$ couples only to state $|0\rangle$, even when the RWA approximation breaks down. The strong-coupling regime (e.g., η_0 of the order of 0.1) can be reached, for example, by using a superconducting, high- Q (10^{10}) microwave cavity [12]. The theoretical model developed above is then a valid description of the coupling between $|0\rangle$ and $|1\rangle$.

The strong microwave field is turned on adiabatically with a switching time constant τ_{sw} , starting at $t=0$. After an interaction time of τ , chosen so that $g'_0(\tau)\tau = \pi/2$, the population of state $|1\rangle$ can be determined by coupling this state to the state $|2\rangle$ with a short (faster than $1/\omega$ and $1/g_{0M}$) laser pulse and monitoring the resulting fluorescence [13].

We have simulated this process explicitly for the following parameters: $\omega = 2\pi \times 6.683\,47 \times 10^9 \text{ sec}^{-1}$, $g_{0M} = 0.1$, and $\tau_{sw} = 0.1$. These numbers are easily achievable experimentally. The laser pulse width τ_{LP} is chosen to be 10^{-12} sec in order to satisfy the constraint that $\tau_L \ll 1/\omega$ and $\tau_L \ll 1/g_{0M}$.

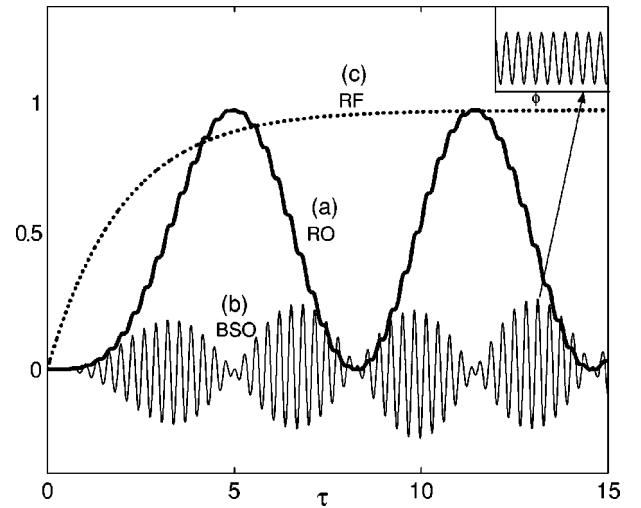


FIG. 2. Illustration of the Bloch-Siegert oscillation (BSO): (a) the population of state $|1\rangle$, as a function of the interaction time τ , showing the BSO superimposed on the conventional Rabi oscillation; (b) the BSO oscillation (amplified scale) by itself, produced by subtracting the Rabi oscillation from the plot in (a); and (c) the time dependence of the Rabi frequency. Inset: BSO as a function of the absolute phase of the field.

In order to optimize the signal, the laser Rabi frequency Ω_L is chosen to be such that $\Omega_L \tau_L = \pi$, so that all the populations of state $|1\rangle$ are excited to state $|2\rangle$ at the end of the pulse. For the cycling transition (1-2) and a pulse focused to an area of $25 \mu\text{m}^2$, the power needed for achieving this Rabi frequency is 1.2 W, which is achievable experimentally. After the laser pulse is turned off, the fluorescence is collected for a duration longer than the spontaneous-decay lifetime (32 nsec) of state $|2\rangle$. Under this condition, our simulation verifies that the detector signal is essentially proportional to the population of state $|1\rangle$, as given by Eq. (13), with the proportionality constant determined by the efficiency of the detection system. If 10^6 atoms are used (a number easily achievable in a dipole trap), the signal-to-noise ratio can be more than 100 for the parameters considered here, assuming a detector solid angle of 0.1π and a quantum efficiency of 0.8. In Fig. 2(a), we have shown the evolution of the excited-state population as a function of the interaction time τ using the analytical expression of Eq. (12). Under the RWA, this curve would represent the conventional Rabi oscillation. However, we notice here some additional oscillations, which are magnified and shown separately in Fig. 2(b), produced by subtracting the conventional Rabi oscillation ($\sin^2[g'_0(\tau)\tau/2]$) from Fig. 2(a). That is, Fig. 2(b) corresponds to what we call the Bloch-Siegert oscillation (BSO), given by $\eta \sin[g'_0(\tau)\tau] \sin(2\phi_\tau)$. The dashed curve (c) shows the time dependence of the Rabi frequency. These analytical results agree closely with the results obtained via direct numerical integration of Eq. (7). Consider next a situation where the interaction time τ is fixed so that we are at the peak of the BSO envelope. The experiment is now repeated many times, with a different value of ϕ each time. The corresponding population of $|1\rangle$ is given by $\eta \sin(2\phi_\tau)$ and is plotted as a function of ϕ in the inset of Fig. 2. This dependence of the

population of $|1\rangle$ on the initial phase ϕ (and, therefore, on the final phase ϕ_τ) makes it possible to measure these quantities.

Note, of course, that the speed of the detection system is limited fundamentally by the spontaneous decay rate γ^{-1} (~ 32 nsec in this case) of state $|2\rangle$. As such, it is impossible in this explicit scheme to monitor the phase of the microwave field on a time scale shorter than its period. If one were interested in monitoring the phase of a microwave field of a lower frequency (so that $\omega^{-1} \gg \gamma^{-1}$), it would be possible to track the phase on a time scale much shorter than its period. One possible set of atomic levels that can be used for this purpose is the Zeeman sublevels (e.g., those of the $5^2S_{1/2}:F=1$ hyperfine level of ^{87}Rb atoms), where the energy spacing between the sublevels can be tuned by a dc magnetic field to match the microwave field to be measured. However, the number of sublevels that get coupled is typically more than 2. A simple extension of our theoretical analysis shows that the signature of the phase of the microwave field still appears in the population of any of these levels and can be used to measure the phase. More generally, the phase signature is likely to appear in the population of the atomic levels, no matter how many levels are involved, as long as the Rabi frequency is strong enough for the RWA to break down.

A recent experiment by Martinis *et al.* [5] is an example where a qubit is driven very fast. In this experiment, a qubit is made using the two states of a current-biased Josephson junction, the resonance frequency is $\omega=6.9$ GHz, and the Rabi frequency is $g=80$ MHz. If this experiment is carried out without keeping track of the phase of the driving field, the degree of qubit excitation will fluctuate due to the BSO, leading to an error which is of the order of $g/\omega=0.01$ —i.e.,

nearly 1%. This error is much larger than the permissible error rate of 10^{-6} for an error-correcting quantum computer that would consist of 10^6 qubits [11]. In order to eliminate the BSO-induced error, one can design the driving system such that the phase is measured, e.g., by using an auxiliary cluster of bits located close to the qubit of interest, at the onset of the qubit excitation, and the measured value of the phase is used to determine the duration of the excitation pulse, in order to ensure the desired degree of excitation of the qubit [14,15]. Finally, we point out that by making use of distant entanglement, the BSO process may enable teleportation of the phase of a field that is encoded in the atomic state amplitude, for potential applications to remote frequency locking [16–19].

In conclusion, we have shown that when a two-level atomic system is driven by a strong periodic field, the Rabi oscillation is accompanied by another oscillation at twice the transition frequency, and this oscillation carries information about the absolute phase of the driving field. One can detect this phase by simply measuring only the population of the excited state. This leads to a phase-correlated fluctuation in the excitation of a qubit and violation of the rule that the degree of excitation depends only on the pulse area. We have shown how the resulting error may be significant and must be controlled for low-energy fast qubit operations.

We thank G. Cardoso for fruitful discussions. We wish to acknowledge support from DARPA Grant No. F30602-01-2-0546 under the QUIST program, ARO Grant No. DAAD19-001-0177 under the MURI program, and NRO Grant No. NRO-000-00-C-0158.

-
- [1] *The Physics of Quantum Information*, edited by D. Boumeester, A. Ekert, and A. Zeilinger (Springer, Berlin, 2000).
- [2] A. M. Steane, *Appl. Phys. B: Lasers Opt.* **64**, 623 (1997).
- [3] A. M. Steane *et al.*, e-print quant-ph/0003087.
- [4] D. Jonathan, M. B. Plenio, and P. L. Knight, *Phys. Rev. A* **62**, 042307 (2000).
- [5] J. M. Martinis *et al.*, *Phys. Rev. Lett.* **89**, 117901 (2002).
- [6] L. Allen and J. Eberly, *Optical Resonance and Two Level Atoms* (Wiley, New York, 1975).
- [7] F. Bloch and A. J. F. Siegert, *Phys. Rev.* **57**, 522 (1940).
- [8] J. H. Shirley, *Phys. Rev.* **138**, B979 (1965).
- [9] S. Stenholm, *J. Phys. B* **6**, 1650 (1973).
- [10] R. J. Abraham, J. Fisher, and P. Loftus, *Introduction to NMR Spectroscopy* (Wiley, New York, 1992).
- [11] J. Preskill, *Proc. R. Soc. London, Ser. A* **454**, 469 (1998).
- [12] S. Brattke, B. T. H. Varcoe, and H. Walther, *Phys. Rev. Lett.* **86**, 3534 (2001).
- [13] C. Monroe *et al.*, *Phys. Rev. Lett.* **75**, 4714 (1995).
- [14] P. Pradhan, G. C. Cardoso, J. Morzinski, and M. S. Shahriar, e-print quant-ph/0402122.
- [15] M. S. Shahriar and P. Pradhan in *Proceedings of the 6th International Conference on Quantum Communication, Measurement and Computing* (Rinton Press, Princeton, NJ, 2002).
- [16] R. Jozsa, D. S. Abrams, J. P. Dowling, and C. P. Williams, *Phys. Rev. Lett.* **85**, 2010 (2000).
- [17] S. Lloyd, M. S. Shahriar, J. H. Shapiro, and P. R. Hemmer, *Phys. Rev. Lett.* **87**, 167903 (2001).
- [18] G. S. Levy *et al.*, *Acta Astron.* **15**, 481 (1987).
- [19] M. S. Shahriar, e-print quant-ph/0209064.

In situ detection of the temporal and initial phase of the second harmonic of a microwave field via incoherent fluorescence

George C. Cardoso,¹ Prabhakar Pradhan,¹ Jacob Morzinski,² and M. S. Shahriar^{1,2}

¹*Department of Electrical and Computer Engineering, Northwestern University, Evanston, Illinois 60208, USA*

²*Research Laboratory of Electronics, Massachusetts Institute of Technology, Cambridge, Massachusetts 02139, USA*

(Received 26 October 2004; published 23 June 2005)

Measuring the amplitude and absolute (i.e., temporal and initial) phase of a monochromatic microwave field at a specific point of space and time has many potential applications, including precise qubit rotations and wavelength quantum teleportation. Here we show how such a measurement can indeed be made using resonant atomic probes via detection of incoherent fluorescence induced by a laser beam. This measurement is possible due to self-interference effects between the positive- and negative-frequency components of the field. In effect, the small cluster of atoms here act as a highly localized pickup coil, and the fluorescence channel acts as a transmission line.

DOI: 10.1103/PhysRevA.71.063408

PACS number(s): 32.80.Qk, 03.67.Hk, 03.67.Lx

Measurement of the amplitude and the absolute (i.e., temporal and initial) phase of a monochromatic wave is challenging because in the most general condition the spatial distribution of the field around a point is arbitrary. Therefore, one must know the impedance of the system between the point of interest and the detector, and ensure that there is no interference with the ambient field. It is recently shown in the literature that the absolute phase measurement can be used for accurate qubit rotations [1–3] and quantum wavelength teleportation [4–6].

Before we describe the physics behind this process, it is instructive to define precisely what we mean by the term “absolute phase.” Consider, for example, a microwave field such that the magnetic field at a position \mathbf{R} is given by $\mathbf{B}(t) = B_0 \cos(\omega t + \phi) \hat{x}$, where ω is the frequency of the field and ϕ is determined simply by our choice of the origin of time. The absolute phase is the sum of the temporal and initial phases—i.e., $\omega t + \phi$. In order to illustrate how this phase can be observed directly, consider a situation where a cluster of noninteracting atoms is at rest at the same location. For simplicity, we assume each atom to be an ideal two-level system where a ground state $|0\rangle$ is coupled to an excited state $|1\rangle$ by this field $\mathbf{B}(t)$, with the atom initially in state $|0\rangle$. The Hamiltonian for this interaction is

$$\hat{H} = \varepsilon(\sigma_0 - \sigma_z)/2 + g(t)\sigma_x, \quad (1)$$

where $g(t) = -g_0 \cos(\omega t + \phi)$, g_0 is the Rabi frequency, σ_i are the Pauli matrices, and the driving frequency $\omega = \varepsilon$ corresponds to resonant excitation. We consider g_0 to be of the form $g_0(t) = g_{0M}[1 - \exp(-t/\tau_{sw})]$ with a switching time τ_{sw} relatively slow compared to other time scales in the system—i.e., $\tau_{sw} \gg \omega^{-1}$ and g_{0M}^{-1} .

As we have shown before [2,3], without the rotating-wave approximation (RWA) and to the lowest order in $\eta \equiv (g_0/4\omega)$, the amplitudes of $|0\rangle$ and $|1\rangle$ at any time t are as follows:

$$C_0(t) = \cos[g'_0(t)t/2] - 2\eta\Sigma \sin[g'_0(t)t/2], \quad (2)$$

$$C_1(t) = ie^{-i(\omega t + \phi)} \{ \sin[g'_0(t)t/2] + 2\eta B \Sigma^* \cos[g'_0(t)t/2] \}, \quad (3)$$

where $\Sigma \equiv (i/2)\exp[-i(2\omega t + 2\phi)]$ and $g'_0(t) \equiv (1/t)\int_0^t g_0(t')dt' = g_0\{1 - (t/\tau_{sw})^{-1}[1 - \exp(-t/\tau_{sw})]\}$. If we produce this excitation using a $\pi/2$ pulse [i.e., $g'_0(\tau)\tau = \pi/2$] and measure the population of state $|1\rangle$ after the excitation terminates (at $t = \tau$), we get a signal

$$|C_1(g'_0(\tau), \phi)|^2 = 1/2 + \eta \sin[2(\omega\tau + \phi)]. \quad (4)$$

This signal contains information of both the amplitude and phase of the field $\mathbf{B}(t)$. The second term of Eq. (3) is related to the Bloch-Siegert shift [7,8], and we have called it the Bloch-Siegert oscillation (BSO) [2,3]. It is attributable to an interference between the so-called corotating and counterrotating parts of the oscillating field, with the atom acting as the nonlinear mixer. For $\eta = 0$, we have the conventional Rabi flopping that is obtained with the RWA. For a stronger coupling field, where the RWA is not valid, the second term of Eq. (3) becomes important [2,3], and the population will depend now both on the Rabi frequency and the phase of the driving field. In recent years, this effect has also been observed indirectly using ultrashort optical pulses [9–11] under the name of carrier-wave Rabi flopping. However, to the best of our knowledge, the experiment we report here represents the first direct, real-time observation of this effect.

From the oscillation observed, one can infer the value of $2(\omega t + \phi)$, which represents the absolute phase of the second harmonic. This is equivalent to determine the absolute phase of the fundamental field, $(\omega t + \phi)$, modulo π . In principle, a simple modification of the experiment can be used to eliminate the modulus π uncertainty. Specifically, if one applies a dc magnetic field parallel to the rf field, it leads to a new oscillation (in the population of either level) at the fundamental frequency, with exactly the same phase as that of the driving field. In the experiment described here, we have restricted ourselves to the case of determining the absolute phase of the second harmonic only.

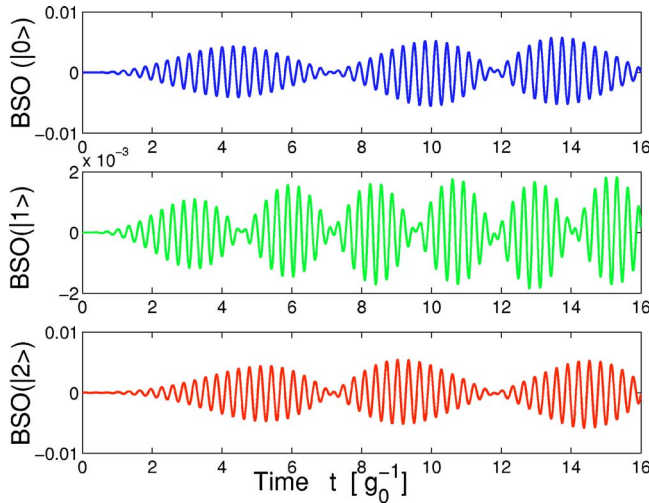


FIG. 1. BSO amplitude versus time t (in units of g_0^{-1}) plots for all the levels of a three-level system. The initial densities of the levels are $\rho_{00}(t=0)=0.5$, $\rho_{11}(t=0)=0.3$, and $\rho_{22}(t=0)=0.2$, the Rabi frequency $g_0=1$, and the resonant frequencies $\omega_{02}=\omega_{21}=10$.

While the above analytical model presented here is based on a two level system, practical examples of which are presented in Ref. [2], the effect is more generic, and is present even in three-level or multilevel systems. In particular, we employed a three-level system to observe this effect, due primarily to practical considerations. The specific system used consists of three equally spaced Zeeman sublevels of ^{87}Rb ($5^2S_{1/2}$: $F=1$: $m_F=-1, 0$, and 1 , denoted as states $|0\rangle$, $|1\rangle$, and $|2\rangle$, respectively), where the degeneracy can be lifted by applying an external bias field. We have performed numerical simulations to confirm the presence of the BSO signature in the population dynamics of such a system as described below.

Consider an equally spaced, ladder-type three-level system ($|0\rangle$, $|1\rangle$, and $|2\rangle$). The transition frequencies for $|0\rangle$ - $|1\rangle$ and $|1\rangle$ - $|2\rangle$ are of the same magnitude ε . We also consider that a direct transition between $|0\rangle$ and $|2\rangle$ is not allowed. Now, let the system be pumped by the same field at a frequency ω . Consider also that the Rabi frequency for the $|0\rangle$ - $|1\rangle$ transition is g_0 and that for $|1\rangle$ - $|2\rangle$ is also g_0 . Then, the Hamiltonian of the three-level system in a rotating frame can be written as

$$\hat{H}' = -g_0[1 + \exp(-i2\omega t - i2\phi)](|0\rangle\langle 1| + |1\rangle\langle 2|) + \text{c.c.}, \quad (5)$$

where $\omega=\varepsilon$. The amplitudes of the three levels are calculated numerically by solving the Schrödinger equation for the above Hamiltonian. The BSO amplitudes are then calculated by subtracting the population amplitude of each level *with* the RWA from the population amplitude *without* the RWA. The BSO oscillations for all the levels of such a system are shown in Fig. 1.

The experimental configuration, illustrated schematically in Fig. 2, uses a thermal, effusive atomic beam. The rf field is applied to the atoms by a coil, and the interaction time τ is set by the time of flight of the individual atoms in the rf field

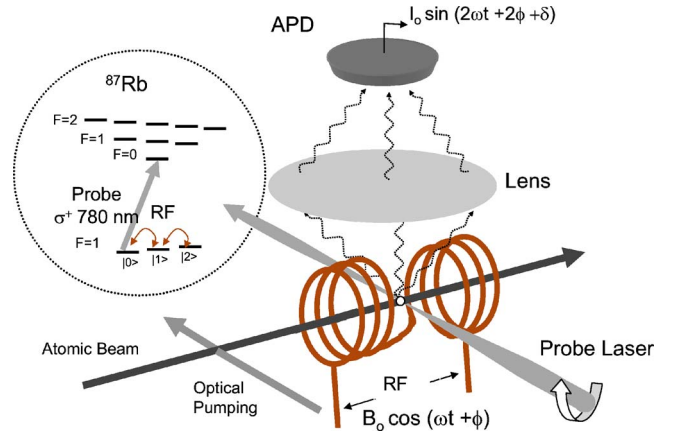


FIG. 2. Experimental setup. The 1-mm cross section rubidium atomic beam passes through the symmetry axis of the rf coil whose magnetic field is along the beam. The rf field of frequency ω is fed by a power amplifier connected to the resonant coil. A circularly polarized probe laser beam is focused down to $30\ \mu\text{m}$ in diameter through a gap in the middle of the rf coil and perpendicularly to the atomic beam. The atomic fluorescence is collected by the lens and detected by an avalanche photodiode (APD). The phase signature appears in the fluorescence signal encoded in an oscillation at a frequency 2ω due to the Bloch-Siegert oscillations. In the picture, δ is an additional phase delay due to the APD circuits and cabling. Inset: Diagram of the relevant sublevels of the D_2 line of ^{87}Rb . The numbers on the left represent the total angular momentum of the respective levels. The strong driving rf field couples to the ground-state Zeeman sublevels. The probe beam must be resonant with an appropriate optical transition for the observation of the phase-locked signal, as discussed in the main text.

before they are probed by a strongly focused and circularly polarized laser beam. The rf field couples the sublevels with $|\Delta m|=1$, as detailed in the inset of Fig. 2. Optical pumping is employed to reduce the populations of states $|1\rangle$ and $|2\rangle$ compared to that of state $|0\rangle$ prior to the interaction with the microwave field.

A given atom interacts with the rf field for a duration τ prior to excitation by the probe beam that couples state $|0\rangle$ to an excited sublevel in $5^2P_{3/2}$. The rf field was tuned to 0.5 MHz, with a power of about 10 W, corresponding to a Rabi frequency of about 4 MHz for the $|0\rangle \rightarrow |1\rangle$ as well as the $|1\rangle \rightarrow |2\rangle$ transition. The probe power was 0.5 mW focused to a spot of about $30\ \mu\text{m}$ diameter, giving a Rabi frequency of about $60\ \Gamma$, where $\Gamma(6.06\ \text{MHz})$ is the lifetime of the optical transition. The average atomic speed is 500 m/s, so that the effective pulse width of the probe, τ_{LP} , is about 60 ns, which satisfies the constraint that $\tau_{LP} \ll 1/\omega$. Note that the resolution of the phase measurement is essentially given by the ratio of $\min[\tau_{LP}, \Gamma^{-1}]$ and $1/\omega$, and can be increased further by making the probe zone shorter. The fluorescence observed under this condition is essentially proportional to the population of level $|0\rangle$, integrated over a duration of τ_{LP} , which corresponds to less than 0.3 Rabi period of the rf driving field [for $g_{0M}/(2\pi)=4\ \text{MHz}$]. Within a Rabi oscillation cycle, the BSO signal is maximum for $g_0(\tau)\tau/2 = (2n+1)\pi/2$, where $n=0, 1, 2, \dots$, so that there is at least one maximum of the BSO signal within the region of the probe.

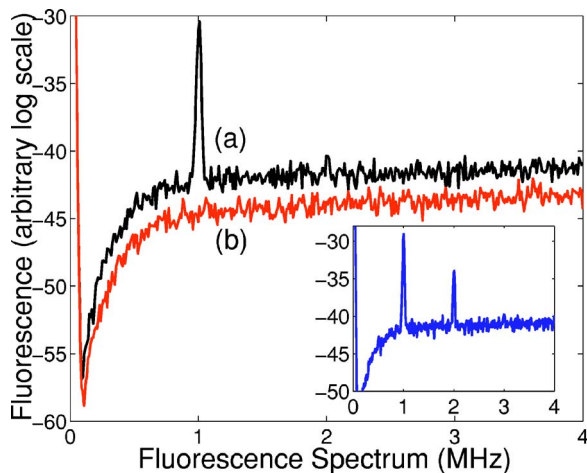


FIG. 3. Bloch-Siegert oscillation spectra. rf at 0.5 MHz and Rabi frequency around 4 MHz. (a) Probe beam resonant with the $5S_{1/2}$, $F=1 \leftrightarrow 5S_{3/2}$, $F'=0$ transition. The signal appears at 1 MHz with a linewidth less than 1 kHz (resolution limited by the spectrum analyzer). (b) Probe beam blocked. The dip structure around 100 kHz is an artifact due to the amplifier gain curve. Inset: Spectrum for same configuration and rf Rabi frequency around 10 MHz. Notice the 2-MHz harmonic which corresponds to the higher-order BSO at 4ω .

Note that atoms with different velocities have different interaction times with the rf field and produce a spread in the BSO signal amplitude within the probe region. However, *the phase of the BSO signal is the same for all the atoms*, since it corresponds to the value of $(\omega\tau + \phi)$ at the time and location of interaction. Thus, there is no washout of the BSO signal due to the velocity distribution in the atomic beam.

Figure 3 shows the spectrum of the observed BSO signal. In Fig. 3(a), we show that the BSO stays mainly at 2ω . When the probe beam is blocked, there is no signal [Fig. 3(b)]. When the rf intensity is increased a component of the BSO at 4ω begins to develop, as predicted. For the data in Fig. 4, the second harmonic of the driving field is used to trigger a 100-MHz digital oscilloscope and the fluorescence signal is averaged 256 times. When the probe beam is tuned to the $F=1 \leftrightarrow F'=0$ transition, the population at $m=-1$ state is probed. When the probe is tuned to $F=1 \leftrightarrow F'=1$, the combined populations of $m=-1$ and $m=0$ states are probed. That results in an effective detection of the complement of the population of $m=1$. On the other hand, when the probe beam is locked to the $F=1 \leftrightarrow F'=2$ transition, all three Zeeman sublevels of $F=1$ are simultaneously probed and the phase information is not clearly present, since the total population of level $F=1$ is a constant. The observed residual phase information is a result of different coupling efficiencies for each of the three ground Zeeman sublevels. We observed that the BSO signal amplitude varies as a function of an external magnetic field applied in the \hat{z} direction, with a peak corresponding to a Zeeman splitting matching the applied frequency of 0.5 MHz.

In Fig. 5, we show that the fluorescence signal is phase locked to the second harmonic of the driving field. First, we placed a delay line of $0.4 \mu\text{s}$ on the cable of the reference field used to trigger the oscilloscope and recorded the fluo-

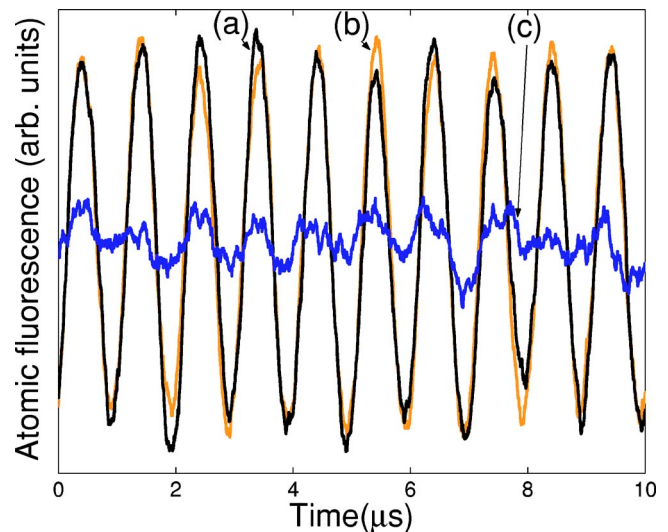


FIG. 4. Time dependence of the fluorescence signal at 2ω when the probe beam is resonant to different excited states. The lines (a), (b), and the noisy line (c) correspond to the probe locked to the transitions $F=1 \rightarrow F'=0$, $F=1 \rightarrow F'=1$, and $F=1 \rightarrow F'=2$, respectively, of the $5S_{1/2} \rightarrow 5P_{3/2}$ transition in ^{87}Rb .

rescence [Fig. 5(a)]. Then, we put the $0.4\text{-}\mu\text{s}$ delay line on the BSO signal cable and recorded the fluorescence [Fig. 5(b)]. The phase difference between the signals recorded in Figs. 5(a) and 5(b) is approximately $0.8 \mu\text{s}$, as expected for a phase locked fluorescence signal. The data presented were for the probe resonant with the transition $F=1 \leftrightarrow F'=1$, but the same results were observed for $F=1 \leftrightarrow F'=0$.

To summarize, we report the first direct observation of the absolute phase of the second harmonic of an oscillating elec-

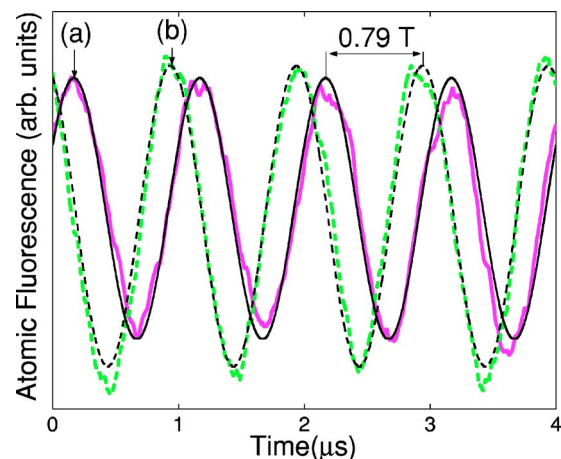


FIG. 5. Demonstration of phase-locked fluorescence. T is the period of the Bloch-Siegert oscillation. (a) Population vs time when a $0.4T$ delay line was inserted in the reference field cable. (b) Population vs time when the same $0.4T$ delay line was placed in the fluorescence signal cable. The figure shows that signal (b) is about $0.8T$ ahead of signal (a), confirming that the atomic fluorescence carries phase information which is locked to the absolute rf field phase. The solid and dashed sinusoidal smooth curves are fittings to the experimental data and were used for period and delay determination.

tromagnetic field using self-interference in an atomic resonance. This process is important in the precision of quantum bit rotations at a high speed. The knowledge of the absolute phase of a rf field at a particular point of space may also be useful for single-atom quantum optics experiments. For example, an extension of this concept may possibly be used to teleport the wavelength of an oscillator, given the presence of degenerate distant entanglement, even in the presence of unknown fluctuations in the intervening medium [4–6,12]. Finally, this localized absolute phase detector may prove use-

ful in mapping of radio-frequency fields in microcircuits. Although a particular alkali-metal atom was used in the present experiment, the mechanism is robust and could be observed in virtually any atomic or molecular species.

This work was supported by DARPA Grant No. F30602–01–2–0546 under the QUIST program, ARO Grant No. DAAD19–001–0177 under the MURI program, NRO Grant No. NRO-000–00–C-0158, and AFOSR Grants: No. F49620–02–1–0400 and No. FA9550–04–1–0189.

-
- [1] D. Jonathan, M. B. Plenio, and P. L. Knight, *Phys. Rev. A* **62**, 042307 (2000).
- [2] M. S. Shahriar, P. Pradhan, and J. Morzinski, *Phys. Rev. A* **69**, 032308 (2004).
- [3] P. Pradhan, G. C. Cardoso, and M. S. Shahriar, e-print quant-ph/0402112.
- [4] R. Jozsa, D. S. Abrams, J. P. Dowling, and C. P. Williams, *Phys. Rev. Lett.* **85**, 2010 (2000).
- [5] M. S. Shahriar, P. Pradhan, G. C. Cardoso, V. Gopal, and G. Pati, e-print quant-ph/0309085.
- [6] E. Burt, C. Ekstrom, and T. Swanson, e-print quant-ph/0007030.
- [7] L. Allen and J. Eberly, *Optical Resonance and Two-Level Atoms* (Wiley, New York, 1975).
- [8] F. Bloch and A. J. F. Siegert, *Phys. Rev.* **57**, 522 (1940).
- [9] G. G. Paulus *et al.*, *Nature (London)* **414**, 182 (2001).
- [10] O. D. Mücke, T. Tritschler, M. Wegener, U. Morgner, and F. X. Kärtner, *Phys. Rev. Lett.* **87**, 057401 (2001).
- [11] O. D. Mücke, T. Tritschler, M. Wegener, U. Morgner, and F. X. Kärtner, *Phys. Rev. Lett.* **89**, 127401 (2002).
- [12] S. Lloyd, M. S. Shahriar, J. H. Shapiro, and P. R. Hemmer, *Phys. Rev. Lett.* **87**, 167903 (2001).

C. Publications Supported Fully Or In Part By This Project

JOURNAL PAPERS

1. "Observation of Ultra-Low Light Level Nonlinear Optical Interactions in a Tapered Optical Nanofiber Embedded in a Hot Rubidium Vapor," S. Spillane, G.S. Pati, K. Salit, M. Hall, P. Kumar, R. Beausoleil, and M.S. Shahriar, **Phys. Rev. Lett.** (2008), Accepted/In-press
2. "Light-Shift Imbalance Induced Blockade of Collective Excitations Beyond the Lowest Order," M.S. Shahriar, P. Pradhan, G.S. Pati, and K. Salit, **Optics Communications**, 278 (2007), 94-98.
3. "Quantum Communication and Computing With Atomic Ensembles Using Light-Shift Imbalance Induced Blockade," M.S. Shahriar, G.S. Pati, and K. Salit, **Physical Review A** 75 (2): Art. No. 022323 FEB 2007.
4. "In-Situ Detection of The Temporal and Initial Phase of The Second Harmonic of a Microwave Field via Incoherent Fluorescence," G. Cardoso, P. Pradhan, J. Morzinski, and M.S. Shahriar, **Physical Review A** 71, 063408 (2005).
5. "Two-dimensional Arbitrary Pattern Nanolithography Using Atom Interferometry," A. Gangat, P. Pradhan, G. Pati, and M.S. Shahriar, **Physical Review A** 71, 043606 (2005).

CONFERENCE PAPERS

1. "Quantum Interference Spectroscopy in Vapors and Trapped Atoms with Nano-Fibers," K. Salit, M. Salit, S. Spillane, R. Beausoleil, P. Kumar, and M.S. Shahriar, presented at the SPIE Photonics West, San Jose, CA, (January 2008) (Invited).
2. "Low Light Level V-Type Electromagnetically Induced Transparency using Tapered Fiber Embedded in Rubidium Vapor," G.S. Pati, S. Spillane, R. Beausoleil, K. Salit, M. Hall, P. Kumar, and M.S. Shahriar, presented at the OSA Annual Meeting (Oct. 2007).
3. "Low Light Level Saturated Absorption in Tapered Fiber Embedded in Alkali Vapor," G.S. Pati, S. Spillane, R. Beausoleil, K. Salit, M. Hall, P. Kumar, and M.S. Shahriar, presented at the CLEO/QELS Meeting, Baltimore, MD (May 2007).
4. "Ultra-low Light Level Saturation Spectroscopy and EIT using a tapered fiber in a hot vapor cell" G.S. Pati, M. Hall, K. Salit, P. Kumar, S. Spillane, R. Beausoleil, and M.S. Shahriar, proceedings of the SPIE Photonics West Conference, San Jose, CA, (Jan 2007).

5. "Deterministic quantum storage, communication, and computing with atomic ensembles using light-shift imbalance induced blockade of collective excitations," M.S. Shahriar, presented at the SPIE conference on Photonic Devices and Algorithms for Computing, San Diego, CA (Aug., 2006) (invited).
6. "Making a Quantum Internet Using Schroedinger Cats," M.S. Shahriar, presented at the Third Feynman Festival, University of Maryland, College Park, MD (August, 2006) (invited).
7. "Quest for a Quantum Internet Using Schroedinger Cats," M.S. Shahriar, presented at the 31st International Nathiagali Summer College, Pakistan (June 2006) (invited).
8. "Deterministic Quantum Storage, Communication and Computing With Atomic Ensembles Using Light-Shift Imbalance Induced Blockade of Collective Excitations," M.S. Shahriar, P. Pradhan, G.S. Pati, V. Gopal, and K. Salit, presented at CLEO, Long Beach, California, (May 2006).
9. "Ensemble-based Quantum Memory, Quantum Communication, and Quantum Computing," Gour Pati, Kenneth Salit, Prem Kumar, and M.S. Shahriar, presented at the SPIE Photonics West Conference, San Jose, CA, January 2006 (invited).
10. "Light-Shift Imbalance Induced Dipole Blockade for Deterministic Quantum Information Processing using Atomic Ensembles", M.S. Shahriar, presented at the International Conference on Quantum Optics, Hong Kong, December, 2005 (invited).
11. "Slow-Light in Cold Atoms for Single Photon Detection," M.S. Shahriar, Midwest Workshop on Cold Atoms, Urbana, IL, November, 2005 (invited).
12. "Pseudo-random noise in high-speed operation of quantum bits," M.S. Shahriar, P. Pradhan, and J. Morzinski, presented at the Conference on Fluctuations and Noise in Photonics and Quantum Optics III, SPIE, Austin, Texas, 2005. (invited).
13. "Solid State Quantum Computing Via Spectral Hole Burning," M.S. Shahriar, presented at the International Workshop on Quantum Informatics, Dec 2004, Hong Kong (invited).
14. "Integrated Quantum Communication and Computing: The Quantum Internet," M.S. Shahriar, presented at the International Workshop on Quantum Informatics, Dec 2004, Hong Kong (invited).
15. "Effects of the Bloch-Siegert Oscillation on the Precision of Qubit Rotations: Direct Two-Level vs. Off-Resonant Raman Excitation," P. Pradhan, G. Cardoso,

J. Morzinski, and M.S. Shahriar, presented at the OSA Annual Meeting, Rochester, NY (2004).

16. "Single-Photon Raman Gain for Single-Photon Detection," G. Cardoso, G.S. Pati, V. Gopal, A. Heifetz, M.S. Shahriar, and P. Kumar, presented at the OSA Annual Meeting, Rochester, NY (2004)

D. Technology Transfer

There was no technology transfer resulting from this project.